Simulation of tokamak power exhaust in alternative divertor configurations with the SOLEDGE2D code

Rui Mao

Rui Mao. Simulation of tokamak power exhaust in alternative divertor configurations with the SOLEDGE2D code. Fluid mechanics [physics.class-ph]. Ecole Centrale Marseille, 2019. English. NNT : 2019ECDM0011 . tel-04095272

HAL Id: tel-04095272
https://theses.hal.science/tel-04095272v1
Submitted on 11 May 2023

ÉCOLE CENTRALE DE MARSEILLE

École Doctorale – SCIENCES DE L'INGENIEUR

Commissariat à l'Energie Atomique et aux Energies Alternatives – Centre de Cadarache
Institut de Recherche sur la Fusion par confinement magnétique

THÈSE DE DOCTORAT

pour obtenir le grade de

DOCTEUR de l'ÉCOLE CENTRALE de MARSEILLE

Discipline : Fusion Magnétique

TITRE DE LA THÈSE : Simulation de l'extraction de puissance dans un tokamak à configuration divertor alternative avec le code SOLEDG2D.

Par

MAO RUI

Directeur de thèse : SERRE Eric
Responsable CEA : CIRAOLO Guido

Soutenue le 06/12/2019 devant le jury composé par:

M. Roman Zagorski	Professeur	IPPLM	Rapporteur
M. Giuseppe Calabro	Professeur	Université la Tuscia	Rapporteur
Mme Pascale Hennequin	DR	CNRS	Examinateur
M. Eric Serre	DR	CNRS	Directeur de thèse
M. Guido Ciraolo	HDR	CEA	Responsable CEA
M. Nicolas Fedorczak	Docteur	CEA	Co-Responsable CEA

Résumé

L'extraction de puissance est l'une des questions cruciales pour l'élaboration d'un réacteur de fusion à confinement magnétique. Le confinement magnétique est responsable de l'impact extrêmement localisé du plasma sur les composants faisant face au plasma, nécessitant une forte dissipation de la puissance dans un volume de plasma dédié appelé divertor. La stratégie du réacteur expérimental ITER qui entrera en fonction à Cadarache dans les prochaines années repose sur une géométrie standard de divertor fermé conçue à partir d'expériences et de simulations plasma à plus petite échelle. En attendant les résultats des expériences sur ITER, les tendances expérimentales actuelles suggèrent toutefois que ce concept de divertor doit être amélioré pour tenir compte des contraintes d'extraction de puissance imposées par un réacteur plus important comme DEMO qui prendra la suite d'ITER. Ce projet de thèse avait pour objectif d'étudier les avantages potentiels des configurations de diverteurs autres que celle d'ITER, comme celle du tokamak WEST en opération au CEA Cadarache ou celle du tokamak chinois HL-2M en construction au laboratoire SWIP en Chine. Un intérêt particulier a été consacré aux configurations dites à « flocon de neige » prévues sur HL-2M et caractérisées par deux points X voisins dans le champ magnétique du divertor. Pour la premier fois le transport du plasma dans ces géométries magnétiques complexes a été simulé grâce à l'utilisation du code SOLEDGE2D-EIRENE développé par l'IRFM CEA et ses partenaires académiques, notamment les laboratoires M2P2 et PIIM d'Aix-Marseille Université. Dans une approche par étapes, les simulations SOLEDG2D ont d'abord été appliquées à la géométrie plus conventionnelle du divertor du tokamak WEST, dans le but d'une comparaison directe avec les résultats expérimentaux. Un ensemble de diagnostics synthétiques a été développé à partir de simulations SOLEDGE pour imiter un large éventail de diagnostics expérimentaux. Des rampes de densité pendant une décharge plasma ont été simulées, mettant en évidence le détachement du plasma des plaques du divertor en accord qualitatif avec des observations expérimentales. Ensuite, les géométries de flocon de neige de HL-2M ont été étudiées. Le détachement du plasma de la plaque du divertor « externe » est étudié dans ces configurations lors de rampes de densité de plasma, à puissance d'entrée constante et à coefficients de transport radial constants. Certaines caractéristiques typiques du détachement, telles que le seuil, la profondeur et la fenêtre en amont du détachement sont examinées. Dans les trois géométries, le début du détachement et l'évolution de la densité du plasma en amont sont caractérisés par le déplacement progressif d'un front de rayonnement de la cible externe au point X principal, comme observé dans les expériences. On constate que, quel que soit le détachement en termes de dissipation de particules, de quantité de mouvement ou de puissance, le seuil de détachement est principalement dominé par la structure géométrique de la plaque de divertor et ne dépend pas de la configuration magnétique du volume de plasma dans le divertor. En particulier, la longueur de connexion de la ligne magnétique dans le divertor n’affecte pas le seuil de détachement, contrairement aux attentes du modèle réduit souvent utilisé pour l’analyse du transport dans le plasma de bord et appelé « modèle à 2 points », mais en accord avec les résultats expérimentaux. Ces résultats de simulation constituent un premier pas vers l'objectif ambitieux de prédire l’impact d'une configuration magnétique « alternative » pour le divertor d’un tokamak de prochaine génération comme DEMO. Tout cela montre bien l’importance de traiter ce problème complexe avec une approche globale associant des tests expérimentaux sur les tokamaks actuels avec le développement de modèles théoriques réduits ainsi que l’analyse des résultats de simulations obtenues à partir d’outils numériques avancés.

Outline

Power and particle exhaust is one of the critical issue toward the elaboration of a magnetic confinement fusion reactor. Magnetic confinement is responsible for an extremely localized plasma bombardment on plasma facing components, requiring strong volume dissipation in a dedicated plasma volume called divertor. ITER exhaust strategy relies on a standard closed divertor geometry designed from smaller scale experiments and plasma simulations. Until conclusions from ITER results, current experimental trends however suggest that such divertor concept will not survive heat exhaust constrains imposed by a larger reactor like DEMO. This PhD project aimed at studying the potential benefit of divertor configurations alternative to the one of ITER, as targeted in the new Chinese tokamak HL2M. A particular interest was devoted to so-called snowflake configurations, consisting in two neighbor X-points on the divertor magnetic field. For the first time, these geometries were fully simulated with the SOLEDGE2D-EREINE code, consisting in a fluid solver for the plasma particle, momentum and energy conservation, coupled to a Monte Carlo solver for neutral dynamics. In a staged approach, SOLEDG2D simulations were first applied to the more conventional divertor geometry of the WEST tokamak, aiming for a direct comparison with experimental results. A set of synthetic diagnostics were built from SOLEDGE simulations to mimic a broad set of experimental diagnostics. Density ramps were simulated, featuring divertor detachment in qualitative agreement with experimental observations. Then, snowflake geometries of HL2M were addressed. First, magnetic geometries were constructed with a magnetic equilibrium solver, optimizing current distribution in poloidal field coils. Mesh were generated on these magnetic maps for the SOLEDGE plasma solver. To tackle the large number of mesh elements required by the snowflake geometry, a coarse-graining convergence technique was developed, providing a speed up of the convergence time of SOLEDGE simulations by a factor of about 10. Three configurations have been generated: standard single null (SN), snowflake plus (SF+), snowflake minus (SF-). Detachment of the outer target is studied in these configurations during plasma density ramps, at constant input power and constant radial transport coefficients. Some typical characteristics of detachment, like threshold, depth and upstream window of detachment are investigated. In the three geometries, detachment onset and evolution with upstream plasma density is characterized by the gradual displacement of a radiation front from the outer target to the main X-point, as observed in experiments. It is found that, whatever the detachment in terms of particle, momentum or power dissipation, the detachment threshold is dominated primarily by the geometrical structure of divertor plate and it does not exhibit dependence on the magnetic configuration of the diverted plasma volume. In particular, the parallel connection length in the divertor is not found to affect the detachment threshold, in contrast with simple expectations from the 2-point model, but in agreement with experimental findings. These simulation results are not enough to draw a clear conclusion on the benefit of alternative divertor configurations. Impurity seeding where not tested, nor the scalability to DEMO sized conditions. It rather evidences that simple ruling considerations may provide quite limited predictions for the problem of power and exhaust, and shows the necessity and difficulty of addressing that this complex simulation tools.

Chapter I: general introduction

1. Tokamak principle

Energy is the foundation for the survival and development of human society. Human food, clothing, housing and transportation are closely related to energy. With the development of society, human beings have put forward higher requirements for energy demand, and energy consumption will increase. Today's world energy consumption is dominated by fossil fuels such as coal, oil and natural gas, while the total amount of fossil fuels is limited, and the more it will be used, the more it will be exhausted. In order to solve energy problems, scientists have been exploring new energy sources. At present, the human energy structure has evolved from a singular structure of fossil fuels to a situation in which fossil fuels are dominant, renewable energy, nuclear fusion energy and other consumption structures complement each other. But the problem of energy shortages and the environment caused by traditional energy resources, have not been solved. Nuclear fusion energy can provide a new clean energy source with low raw material consumption and abundant resources. Comparing with clean energy such as solar energy, water energy, wind energy and geothermal energy, nuclear fusion energy is not limited by time and geography. More importantly, it can be considered as an inexhaustible source of energy and radioactive environmental pollution is not serious. The raw materials for the nuclear fusion reaction are the isotopes of hydrogen, deuterium and tritium. The seawater contains rich deuterium and the tritium can be produced by artificial methods from lithium. Finally, fusion reactors are intrinsically safe with respect to thermonuclear explosions. So the controlled nuclear fusion appears as a promising way to solve the energy problem. Therefore, the research of controlled nuclear fusion has received more and more attention from most countries in the world.

So far, humans have been studying controlled thermonuclear fusion for more than half a century. There are two main ways of controlled nuclear fusion, the magnetic confinement fusion and the inertial confinement fusion. Inertial confinement fusion takes the path of achieving combustion at extremely high density in a very short time, and is closely related to national defense. Here we mainly introduce magnetic confinement fusion, which is a low-density long-term combustion path. In the 1950s, a few nuclear powers such as the Soviet Union, the United States, and the United Kingdom began secret research on controlled nuclear fusion. At first, many proposals were made and various experimental devices were built for research, such as Stellarator, Mirror machine, Pinch (z-pinch/θ-pinch), Tokamak, Spheromak and so on. The main problems encountered in the research process are the macroscopic instability of the plasma, the poor confinement performance, and the plasma parameters are far from the requirements of the nuclear fusion reaction. With a series of major breakthroughs on Tokamak, controlled fusion is now concentrated on research based on tokamak devices. Tokamak is abbreviated by the four words "Toroidal", "kamera", "magnit" and "kotushka" in Russian. The concept is proposed by Soviet physicists Tamm and Sakharov. It is a spiral magnetic field formed by a polar magnetic field generated by a large current induction and a toroidal magnetic field generated by an external coil to restrain the high temperature plasma, as shown in figure 1.1.1.

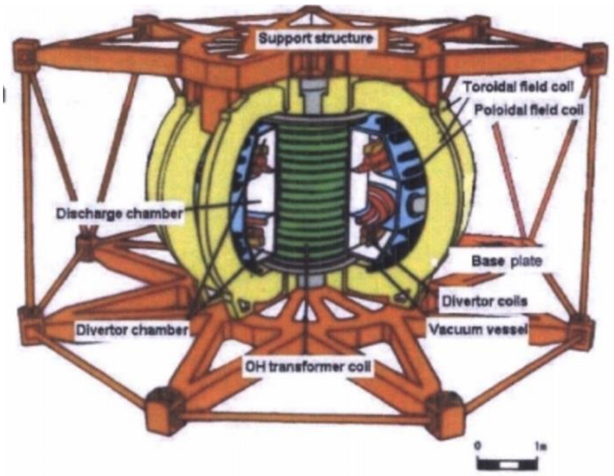

Figure 1 structure sketch of HL-2A Tokamak device in SWIP, China.

After more than 20 years of hard work, the plasma energy confinement time obtained by the experiment was still far below the theoretically expected one. Scientists began to recognize the complexity and difficulty of the research in nuclear fusion, recognizing that technology of controlled nuclear fusion will not be resolved in a short period of time and will require international exchanges and cooperation. In 1958, at the "Peaceful Use of Atomic Energy" conference in Geneva, countries published their own research on nuclear fusion. Since then, controlled fusion research has become the subject of international cooperation.

In 1985, with the approval of the US and Soviet leaders and the International Atomic Energy Agency (IAEA), a major international science and technology cooperation program, the International Thermonuclear Experimental Reactor (ITER[1]), was established with the goal of building a sustainable burning Tokamak fusion experimental reactor to verify the engineering feasibility of the fusion reactor. ITER program is one of the world's largest international science and technology cooperation programs for large scientific engineering. Seven countries (China, EU, India, Japan, South Korea, Russia and the United States) participated in the negotiation of the ITER plan. After nearly five years of arduous negotiations, on November 21, 2006 at the Elysee Palace in France, the seven countries signed the "Agreement on the privileges and immunities of the ITER International Fusion Energy Organization for the Joint Implementation of the ITER Project" and other relevant documents. At this point, the ITER plan negotiations have come to a successful conclusion. On October 24, 2007, the International Fusion Energy Organization was formally established in France, and the ITER program was officially launched. The ultimate goal of the ITER program is to study nuclear fusion energy and explore ways to fundamentally address the energy and environmental issues that contemporary mankind are facing.

The main nuclear reactions in the controlled nuclear fusion process are as follows:

$$\mathrm{D + D \rightarrow n + He^{3} + 3.27MeV}$$
$$\mathrm{D + D \rightarrow p + T + 4.03MeV}$$
$$\mathrm{D + He^{3} \rightarrow T + He^{4} + 18.35MeV}$$
$$\mathrm{D + T \rightarrow n + He^{4} + 17.59MeV}$$
$$\mathrm{T + T \rightarrow 2n + He^{4} + 11.33MeV}$$

The average energy released by each nucleus in the above five fusion reactions was 0.82 MeV; 1.01 MeV; 3.67 MeV; 3.51 MeV; 1.89 MeV. The reaction cross sections of these reactions are also different. The cross section of the D-T fusion reaction is the largest one, and the reaction cross section of the D-D fusion is relatively small. The fusion reactor based on the T-T reaction is much more difficult than the fusion reactor based on the D-T reaction. In terms of feasibility, the current priority for fusion energy applications is the D-T reaction fusion reactor.

The raw materials for the above mentioned five nuclear fusion reactions are the isotopes of hydrogen, namely the deuterium and tritium. Deuterium atoms are naturally occurring isotopes. There is a large amount of deuterium in seawater, while tritium is an isotope produced by artificial methods. Its half-life is only 12 years. It can be produced by the reaction of neutrons with lithium. The main nuclear reactions are as follows:

$$\mathrm{n} + \mathrm{Li}^6 \rightarrow \mathrm{T} + \mathrm{He}^4 + 4.79\mathrm{MeV}$$

$$\mathrm{n} + \mathrm{Li}^7 \rightarrow \mathrm{n} + \mathrm{T} + \mathrm{He}^4 - 2.47\mathrm{MeV}$$

We now introduce power balance estimations for nuclear fusion reactors. The zero-dimensional power balance of a fusion reactor can be expressed as:

$$S_\alpha + S_\mathrm{h} = S_\kappa$$

Where S_α represents the energy carried by the α particles generated in the fusion reaction, the α particles being constrained by the magnetic field as charged particles, so S_α remains in the plasma to provide a heat source. Assuming all the components are at the same temperature, the fuel is 50%-50% D-T mixture, both with a density of n/2. The pressure and temperature as basic variables, and the expression of S_α is as follows:

$$S_\alpha = \frac{n^2}{4} E_\alpha \langle \sigma v \rangle$$

Here, σ and v represent the collision cross section and collision frequency for fusion reaction. $\langle \sigma v \rangle$ is the rate coefficient for fusion reaction. E_α is energy carried by one α particle, $\mathrm{E}_\alpha = 3.5\mathrm{MeV}$. T and p represent the plasma temperature and pressure.

S_h is the external heating power injected into the plasma and S_κ represents the power flowing out of the plasma. Accurate calculation requires the temperature gradient distribution and thermal conductivity of the plasma edge, so we simplify this problem by defining a zero-dimensional energy confinement time:

$$S_\kappa = \frac{3nk_BT}{\tau_E}$$

Here, $3nk_BT$ represents the plasma energy, the energy confinement time τ_E represents the relaxation time of plasma energy due to thermal conduction down to e^{-1}. In practice, it is determined by regression analysis of large experimental database data for plasma discharges on different Tokamaks. For the immediate purpose, τ_E can be assumed to be a known quantity. The zero-dimensional power balance relationship of the fusion reactor with can be obtained:

$$\frac{n^2}{4} E_\alpha \langle \sigma v \rangle + \mathrm{S}_\mathrm{h} = \frac{3nk_BT}{\tau_E}$$

From the above power balance equation, two conditions for maintaining the steady state operation of the fusion reactor can be obtained. The first one is the ideal ignition condition that the plasma reaches steady state power balance without considering heat transfer loss and external heating, $S_\alpha = S_b$. In other words, the condition represents that the power of α particle generated by fusion reaction can satisfy the radiation loss due to bremsstrahlung. S_b represents the radiation loss due to bremsstrahlung per unit volume and can be expressed as a function of temperature and density:

$$\mathrm{S_b = C_B Z_{eff} n^2 T^{1/2}}$$

$\mathrm{C_B}$ is the bremsstrahlung coefficient, and $\mathrm{Z_{eff}}$ is the equivalent charge number. If one assumes that there is no impurity, Zeff=1 can be considered. Bringing in the expression of S_α and S_b, we get the plasma temperature requirement: $\mathrm{T_e} \geq 4.4\mathrm{keV}$. This temperature sets the lower temperature limit of the fusion reactor.

The second condition is a more realistic power balance state. Assume that a particle heating power is sufficient to balance bremsstrahlung and heat transfer power loss. After a simple algebraic calculation, we can get the famous Lawson criterion:

$$n\tau_E \geq \frac{12k_BT}{\langle\sigma v\rangle E_\alpha}$$

For the D-T reaction, using the typical physics parameters, the Lawson criterion can be approximated as [2]:

$$\mathrm{T_e} \geq 14\mathrm{keV}$$
$$n\tau_E \geq 1.5 \cdot 10^{20}\,\frac{s}{m^3}$$

The minimum of $n\tau_E$ occurs near T=26keV. However, this number has not yet been achieved in any reactor. External heating power is very important in the absence of ignition, because S_h can reduce the requirement of $p\tau_E$ as:

$$p\tau_E \geq \frac{S_\alpha}{S_\alpha + S_\mathrm{h}} \frac{12k_BT}{\langle\sigma v\rangle E_\alpha}$$

When $S_\mathrm{h} > 0$, the reactor becomes a power amplifier and its gain parameter $\mathrm{Q} = \frac{P_{out}-P_{in}}{P_{in}}$ is the key to measuring device performance.

At present, a few experiments on the tokamak devices have produced important amounts of fusion power. In 1997, the output power of JET reached 16MW, the output fusion energy reached 22MJ, and the gain factor Q=0.65 [3]. It is higher than the previous recording of the fusion power of 10.4 MW and the gain factor of 0.3, in TFTR D-T experimental [4]. Now that the ITER device is being built in Cadarache in the south of France, its goal is to build a Tokamak nuclear fusion reactor with self-sustaining combustion (ie, to achieve "ignition" conditions), to obtain a combustion plasma with a fusion performance factor Q>10. Verify the feasibility of fusion energy to explore the physical and engineering issues of future fusion demonstration reactors and commercial fusion reactors.

[1] ITER Physics Basis Editors, ITER Physics Expert Group Chairs and Co-Chairs and ITER Joint Central Team and Physics Integration Unit, Chapter 1: Overview and summary. Nucl. Fusion 39(12), 2137-2174(1999).
[2] J. Wesson, 'Tokamaks', Oxford Engineering Science Series No 48, Clarendon Press, Oxford, 2nd edition, 1997.
[3] A. Gibson and the JET Team, Deuterium-tritium plasma in the Joint European Torus (JET): Behavior and implications. Phys. Plasma 5(5), 1839-1847(1998)
[4] J. D. Strachan, et al, TFTR DT experiments, Plasma Phys. Control. Fusion 39(12B), B103-B114(1997).

2. Introduction of divertor configuration

The development of controllable nuclear fusion faces many technical problems. One of the most difficult problems is the power exhaust. In order to have high performances in the core region the plasma temperature can reach up to 10^8°C. In these conditions a strong plasma-wall interaction occurs at the wall of chamber. To avoid destroying the vessel wall and poisoning the plasma by impurities from wall, limiters and divertors are often used in tokamaks to solve this problem.

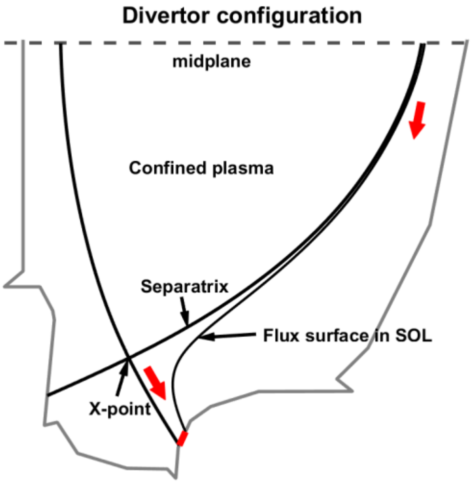

Figure 1.2.1 Cross section of the single null divertor configuration in the HL-2M tokamak (under construction in SWIP, China). The red arrow indicates the plasma flow going from the upstream midplane region, strongly connected with the confined core plasma, to the divertor target.

The divertor configuration is formed by superposing the magnetic field generated by the divertor coil with the spiral magnetic field in the vacuum chamber, and the separatrix or the last closed magnetic flux surface (LCFS), is completely determined by the magnetic field. As shown in figure 1.2.1, we define a number of distinct regions in the plasma. Here, we use normalized poloidal flux coordinates, $\psi_x = (\psi - \psi_m)/(\psi_{sep} - \psi_m)$, ψ is plasma poloidal magnetic flux, ψ_{sep} is ψ at plasma separatrix, ψ_m is ψ at plasma aixs. $\psi_x = 1$ at separatrix and $\psi_x = 0$ at plasma axis. First, the 'plasma core' region, $\psi_x < \psi_{prad}$, ψ_{prad} is the limit of intense impurity radiation, in present devices, ψ_{prad}~0.9. In the core region, the radiated power from low-Z impurities is negligible and the neutral particle density is low. The second region is the 'core periphery', $\psi_{prad} < \psi_x < 1$, there is a small number of neutrals and radiation power from low-Z impurities. The regions inside the LCFS, core and the core periphery region, constitute confined plasma or main plasma. Third, the 'scrape-off layer' (SOL) region, $\psi_x > 1$, which has a similar properties with the core periphery, but directly touch the divertor plate. The SOL region below the X-point has a high neutral density and low-Z impurity radiation. Finally, the 'private flux region', below the X-point, which is surrounded by the two divertor legs and the wall.

The divertor configuration shifts the region with strong plasma-wall interaction away from the main plasma, and the open magnetic lines in SOL region can transport the impurities generated on the first wall to the divertor, then pump out. The main advantage of the divertor configuration relative to limiter is that, the particle and heat flow are introduced into the diverter chamber away from the main plasma, so that the thermal energy is deposited on the specially designed divertor plate, so as to avoid impurity contamination of the main plasma. As the performance of the plasma can be obviously improved, the present tokamak devices use the divertor configuration.

The limiter configuration is relatively simple, it can concentrate the plasma-wall interaction region to the specially designed limiter surface, but the heat flow and high energy particles in SOL region will cause the erosion of the limiter material. The impurity particles from the limiter easily contaminate the core plasma.

The divertor physics study can be traced back to the initial stage of controlled nuclear fusion experiments, and Spitzer first proposed the concept of divertor in the report of the 1950s [1]. The original purpose of the divertor was primarily to control the impurities entering the main plasma, i.e., by isolating the region where the primary plasma-wall interaction takes place in a separate chamber, and consequently the impurity source is isolated from the main plasma. It is also desirable to transport impurities from the first wall to the divertor through the open magnetic lines in SOL region and remain there. Although the experimental data quality was not good in the early stages of fusion research, the evidence suggested that the divertor has a good shielding effect on impurities. In 1974, the earliest tokamak divertor experimental study was carried out on DIVA in Japan [2]. Subdivision studies were carried out on Tokamaks such as DITE [3] in the United Kingdom, T-12 [4] in the former Soviet Union, PDX14 [5] in the United States, and ASDEX [6] in Germany. These early experimental devices are now closed.

At present, the international advanced tokamak mainly uses divertor configuration, such as JET [7], DIIID [8], JT-60U [9], ASDEX-U [10], Alcator C-Mod [11], KSTAR [12] and China's EAST [13], HL-2A [14], WEST [15] and the International Thermonuclear Experimental Reactor (ITER) [16] under construction. The main parameters of these tokamak devices are shown in Table 1.2.1.

Device	Country	X-point	I_p(MA)	B_t(T)	P_{tot}(MW)	R (m)	a (m)	κ
JET	United Kingdom	1	7	4	42	3	1.25	1.8
DIIID	United States	2	3	2.2	22	1.66	0.5	1.6
JT-60U	Japan	1	3	4	40	3.4	0.9	1.8
ASDEX-U	Germany	1	1.6	3.9	31	1.65	0.5	1.6
Alcator C-Mod	United States	2	2	8.11	13.7	0.68	0.21	1.85
KSTAR	South Korea	2	2	3.5	26	1.8	0.5	2.0
EAST	China	2	1	3.5	7.5	1.85	0.45	2
HL-2A	China	2	0.48	2.8	10	1.64	0.4	1.6

ITER	France	1	17	5.3	110	6.2	2.0	1.85

table 1.2.1 The parameter of the international advanced tokamak

Divertor physics has evolved over the past few years and is now the main focus of research in tokamak. The four key issues facing this area are [17]:

1. Reduce the power flux on divertor target from main plasma.
2. A sufficiently high neutral gas pressure is generated near the pump to remove the fuel and helium.
3. Reduce plasma erosion on vacuum chamber walls, thereby reducing the generation of impurities.
4. Excrete impurities in the edge region of the plasma to prevent contamination of the main plasma

[1] Spitzer L 1951 US Atomic Energy Commission Report NYO-993 (PM-S-1)
[2] M. Nagami, et al, Divertor experiment for impurity control in DIVA. J. Nucl. Mater. 76-77, 521-527 (1978)
[3] P.e. Stott, et al, The Bndle diverotr- part I: Magnetic configuration. Nucl. Fusion 17(3), 481-496 (1977)
[4] Botnikov A. V., et al, Plasma Physics and Controlled Nuclear Fusion Research IAEA-CN-37/T-3-2 387 vol I, (1978)
[5] Meade D., et al, Plasma Physics and Controlled Nuclear Fusion Research IAEA-CN-38/X-1665 vol I (1980)
[6]Keilhacker M., et al, Plasma Physics and Controlled Nuclear Fusion Research IAEA-CN-38/O-1 vol II, (1980) [7] Jean Jacquinot, et al, Chapter 2: Mission and Highlights of the JET Jiont Undertaking: 1978-1999. Fusion Sci. Technol. 53(4), 866-890 (2008).
[8] J. L. Luxon, et al, Overview of the DIIID Fusion Science Program. Fusion Sci. Technol. 48(2), 807-827 (2005)
[9] A. Kitsunezaki, et al, JT-60 Program. Fusion Sci. Technol. 42(2,3), 179-184 (2002)
[10] Bernhard Streibl, et al, Chapter 2: Machine Design, Fueling, and Heating in ASDEX Upgrade. Fusion Sci. Technol. 44(3), 578-592 (2003)
[11] J. Irby, et al, Alcator C-Mod Design, Engineering, and Disruption Research. Fusion Sci. Technol. 51(3), 460-475 (2007)
[12] G. S. Lee, et al, Design and construction of the KSTAR tokamak. Nucl. Fusion 41(10), 1515-1523 (2001)
[13] Yuanxi Wan, HT-7 Team and HT-7U Team, Overview of steady state operation of HL-7 and present status of the HT-7U project. Nucl. Fusion 40(6), 1057-1068 (2000)
[14] Dequan Liu, et al, Construction of the HL-2A tokamak. Fusion Eng. Des. 66-68, 147-151 (2003)
[15] Bucalossi J. et al 2014 Fusion Eng. Des. 89 907
[16] M. Shimada, et al, Chapter 1: Overview and summary. Nucl. Fusion 47(6), S1-S17 (2007)
[17] C S Pitcher and P C Stangeby 1997 Plasma Phys. Control. Fusion 39 779

3. Alternative divertor configurations

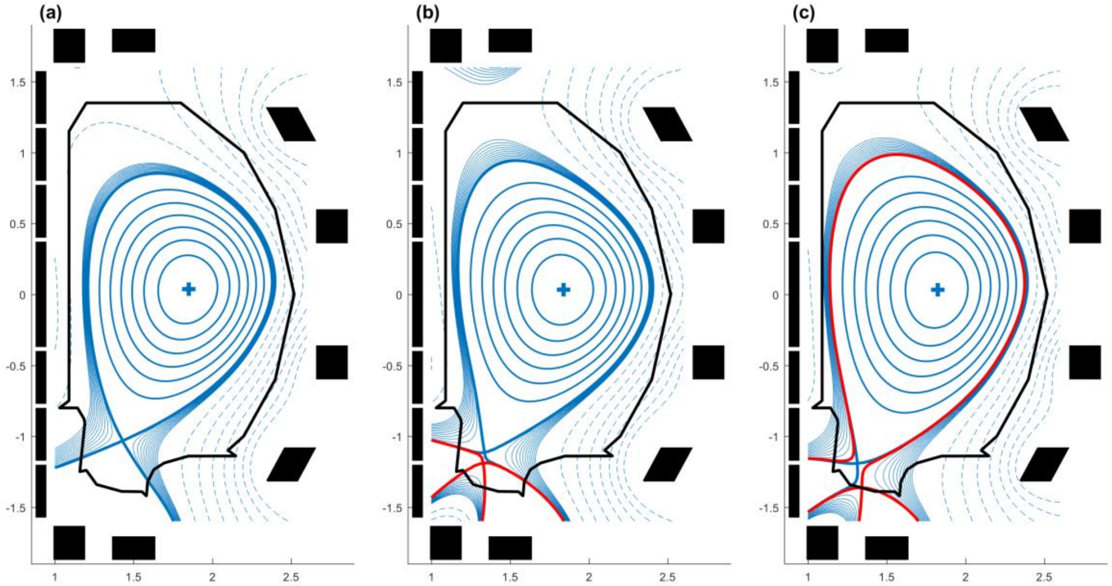

Figure 2. HL2M cross section with the 16 poloidal field coils (black). (a) single null, (b) snowflake plus, (c) snowflake minus configuration. The blue lines represent the plasma flux surface and the red lines represent the flux surface correspond to the second X-point.

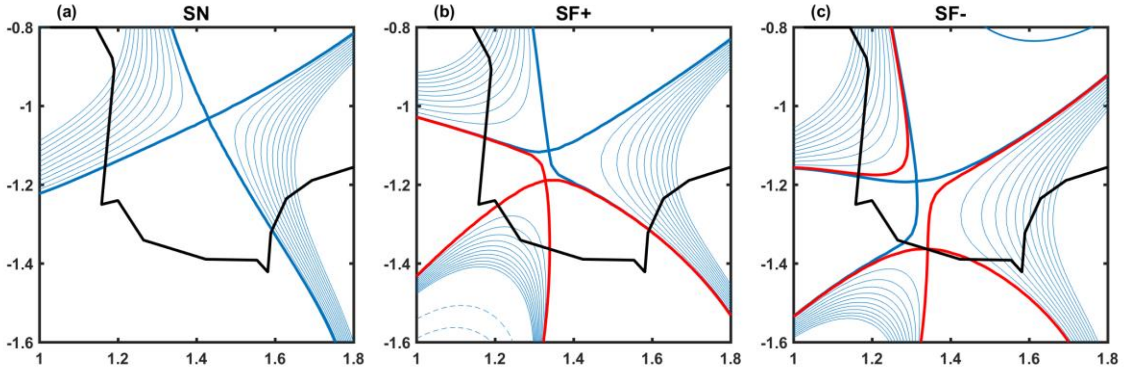

Figure 3. The plasma flux surface in divertor region for (a) single null, (b) snowflake plus, (c) snowflake minus configurations. The blue lines represent the plasma flux surface and the red lines represent the flux surface correspond to the second X-point.

For wide dispersal of heat and particle flow to divertor target, people explore alternative divertor configurations with multiple X points [18-20] in experiment and theory, including snowflake divertor (SF) [21], X divertor (XD) [22, 23], and Super X Divertor (SXD) [24]. The snowflake divertor configuration is the focus of this project. It is characterized by combining the first-order zeros of two standard divertors into a second-order zero [25, 26]. The poloidal magnetic surface in the precise second-order zero region has six separatrix branches that present the appearance of the snowflake. The precision snowflake divertor is topologically unstable [25]. In the experiment, two variants of the snowflake divertor, snowflake plus (SF+) and snowflake minus (SF-), are usually achieved at steady state. In the SF+ configuration, the second X point is located in the private flux region of the standard divertor X point. In the SF-, the second X point is located in the SOL region. As shown in figure 2,3, the common feature of the SF+ and SF- divertor is that by adding a second X point, the low poloidal field region around the first X point is wider, and the parallel length and magnetic flux expansion are greatly increased. It is expected that the plasma detachment can be more easily obtained (eg, lower impurity injection and upstream plasma density), as well as higher total power dissipation capability, and better control of the radiation front [27-29]. Preliminary experiments in TCV [30-32], DIIID [33-35] and NSTX [36] have shown that the heat flux to target for the SF- divertor filter is significantly reduced.

[18] Petrie T.W. 2013 Nucl. Fusion 53 113024
[19] Soukhanovskii V.A. et al 2013 J. Nucl. Mater. 438 S96–101
[20] Vijvers W.A.J. et al and The TCV Team 2014 Nucl. Fusion 54 023009
[21] Ryutov D.D. 2007 Phys. Plasmas 14 064502
[22] Takase H. 2001 J. Phys. Soc. Japan 70 609
[23] Kotschenreuther M., Valanju P.M., Mahajan S.M. and Wiley J.C. 2007 Phys. Plasmas 14 072502
[24] Eich T., The ASDEX Upgrade Team and The J. EFDA Contributors 2013 Nucl. Fusion 53 093031
[25] D. Ryutov, Phys. Plasmas 14 (2007) 064502.
[26] D. Ryutov et al., Plasma Phys. Control. Fus. 54 (2012) 124050.
[27] LaBombard B. et al 2015 Nucl. Fusion 55 053020 [30]
[28] Kotschenreuther M., Valanju P., Covele B. and Mahajan S. 2013 Phys. Plasmas 20 102507
[29] Lipschultz B., Parra F.I. and Hutchinson I.H. 2016 Nucl. Fusion 56 056007
[30] F. Piras et al., Phys. Rev. Lett. 105 (2010) 155003
[31] H. Reimerdes et al., Plasma Phys. Control. Fus. 55 (2013) 124027.
[32] W.A. Vijvers et al., Nucl. Fus. 54 (2014) 023009.
[33] V.A. Soukhanovskii et al., Nucl. Fus. 51 (2011) 012001.
[34] V.A. Soukhanovskii et al., Phys. Plasmas 19 (2012) 082504.
[35] V.A. Soukhanovskii et al., J. Nucl. Mater. 438 (2013) S96.
[36] D.N. Hill, Nucl. Fus. 53 (2013) 104001

4. Plasma wall interaction

The plasma-wall interaction is a very important research field in controlled fusion research [1, 2]. The interaction between plasma and material mainly includes two aspects: first, high-energy particles from the main plasma damage the wall material; second, various particles emitted from the wall enter the main plasma region and affect the confinement performance of plasma. The plasma-wall interaction has a great influence on the core plasma and involves the engineering problems of the first wall and the divertor. It is one of the key research topic of the current fusion reactor. On the one hand, we should study the interaction between plasma and materials to find materials that can withstand the huge heat flow in the fusion device and have low erosion rate; on the other hand, we should study the plasma behavior near the first wall material, especially in the divertor region. Plasma-wall interactions involve boundary plasma physics, chemistry, physical surface physics, chemistry, recycling, and changes in the internal composition of materials.

During the operation of the tokamak, the plasma material will be bombarded by energetic ions, electrons and neutral particles, causing the wall material atoms to enter the plasma as impurities, which will also shorten the service life of the wall material. The high-intensity particle, heat flows from the transient events such as plasma disrpution and edge localized modes (ELM) can also cause significant damage to the first wall. The damage mechanism of plasma-wall interaction in fusion device mainly has the following aspects [3,4].

1. Physical sputtering: Part energy of the incident particles is transmitted to the atoms in the wall by collision. If the energy of these atoms exceeds the surface binding energy, the atoms will escape from the surface of the material and enter the plasma. This process is called sputtering. W_0 represents the binding energy of the solid atom, the threshold of physical sputtering can be expressed as $\mathrm{E} = (m_1 + m_2)^2 \mathrm{W}_0 / m_1 m_2$, with the assumption of elastic collision, m_1, m_2 represent the mass of incidenti paritcle and atom in wall. The sputtering yield is related to the type, energy, incidence angle and charge state of the incident particles. It is also related to the structure, composition, temperature and surface morphology of the wall material. As the energy of the incident particles increases, the sputtering yield will increase rapidly. Since wall treatment does not reduce the occurrence of physical sputtering, physical sputtering is the dominant impurity generation mechanism in magnetic confinement fusion devices.

2. Chemical sputtering: mainly occurs in graphite and carbon-based composites, where incident particles and carbon combine to form volatile molecules. For example, H, O and C combine to form CH or CO. The sputtering rate is related to the energy of the incident particles, the particle flew density, and the composition, temperature, structure of the material.

3. Back scattering: After the incident particles or atoms, such as H, D, T, He, etc., entering the wall surface, a series of elastic and inelastic collisions with the atoms in the material happens, and finally these particles return to the edge plasma. This proceed called back scattering. Back scattered particles are mostly in the form of neutral particles. This process does not increase the impurity content of the plasma, but has a greater effect on the recycle of the working gas.

4. Desorption: In general, the solid surface has a layer of adsorbed gas from the surrounding environment, includes working gas and impurity gas. The adsorption methods include physical adsorption and chemical adsorption. For physical adsorption, the binding energy is small, generally 0.3eV; for chemical adsorption, the binding energy can reach up to 3eV. The low-energy gas is released when the temperature of the heated surface increases. This process is called thermal desorption. The atoms and molecules with high binding energy are released only when more energy is obtained from the incidence particles.

5. Radiation Enhanced Sublimation (RES): For graphite and some carbon-based composites, the sputtering yield increases rapidly at $T > 1200$ K, this process called radiation enhanced sublimation. The principle of RES is that after the material is bombarded by high-energy particles, interstitial atoms and holes are generated inside the material. When the temperature decreases, the interstitial atoms and holes will quickly recombine; when the temperature increases, the interstitial atoms move toward the surface of the material , and the evaporation rate is large due to the low binding energy betwwen the interstitial atoms and the surrounding atoms.

6. Unipolar arc: Since electrons in the plasma move faster than ions, a negative charge is accumulated on the surface, and a sheath with negative potential formed on the surface of the wall. If the sheath potential is large, an arc is generated between the wall and the plasma, causing a large amount of electron emission and evaporation and the disrupture of sheath. With a large amount of electron emission occurs in a small area, the local sheath potential will be weakened, resulting in a flow of electrons passing through the sheath, i.e., an unipolar arc. In addition, a unipolar arc is also generated when the plasma potential is raised. Unipolar arc is one of the main mechanisms for the production of metal impurities in plasma. This phenomenon mainly occurs in the initial stage of discharge. As time evolves, the arcing event will be less and less, and will not seriously affect the plasma.

7. Thermal evaporation: Evaporation occurs when the temperature of the first wall material exceeds the boiling point. Evaporation is also one of the main mechanisms for generating impurities in the plasma, and can be suppressed by the temperature control. Events such as unipolar arcs and disruptures can cause local heating of the wall material, causing a sharp change in the temperature of the material, causing cracking and chipping of the surface of the material. This phenomenon is called thermal shock.

The extent of plasma-wall interaction is dominated by the temperature, density, particle flow, and power flow of the plasma. These parameters determine the sputtering rate of the material and the location of the surface engraved and re-deposited in target. Impurities will both dilute the fusion fuel, cause large radiation loss, and edge radiation cooling will also cause plasma disruption. Low-binding energy impurities such as water and carbon oxides are easily released from the surface of the material, and other impurities can only be released from the surface material by thermal desorption, high-energy particle collision, baking and glow discharge.

In the early study of magnetic confinement fusion, the characteristics of the wall and edge plasma were less studied. The plasma obtained at that time was mixed with many impurities, and the effective Z even reached up to 5 or more. At the same time, due to the suction and deflation of the wall, the recycling at the boundary changes drastically, resulting in uncontrollable plasma density profiles and low plasma parameters. Since the 1970s [40, 41], the people has gradually paid attention to the study of plasma-wall interaction. Experiments have found that boundary recycling has a great influence on plasma quality [42, 43]. With the further research, a series of wall treatment technologies have been developed, such as various pre-discharge cleaning, baking, boronization, silicidation, and lithiation, et al. Wall treatment effectively controls the impurities and boundary recycling. Plasma confinement improvement is closely related to wall conditions, especially boundary particle recycling. How to maintain good wall conditions and low boundary recycling under long pulse conditions is a problem to be solved in the future.

[1] G. Federici, et al, Plasma-material interactions in current tokamaks and their implications for next step fusion reactor. Nucl. Fusion 41 (12), 1967-2137 (2001)
[2] V. Philipps, Plasma-wall interaction, a key issue on the way to a steady state burning fusion device. Phys. Scr. T123, 24-32 (2006)
[3] John Wesson, Tokamaks, Oxford: Clarendon Press, Third Edition (2004)
[4] Dirk Naujoks, Plasma-Material Interaction in Controlled Fusion. Berlin: Springer, (2006)

Chapter II: Plasma models for tokamak edge

1. From kinetic model to fluid equations

The edge plasma is the transition region from the main plasma to the wall and the divertor. The particles and power flow from the core plasma determine the operating mode of the edge plasma and the impurity yield of the wall. The impurities and neutral particles generated from the wall can also affect the confinement property of the core plasma. Therefore, studying the behavior of edge plasma is of great significance to the operation of tokamak. a briefly introduction of the edge plasma physical model is shown below.

Different levels of models can be used to describe the plasma. The most accurate model is the kinetics theory, which attempts to determine the distribution function of particles and can explain various physical phenomena. However, the solution of the model is more complicated, the results are more abstract, and the results are not physically intuitive. The description at the lower level is the macroscopic fluid model. The basic unknowns in this model are macroscopic physical quantities that are easily identifiable, such as density, temperature, and pressure. Compared with the kinetics theory, the unknowns of fluid model are only a function of space and time, ie Q=Q(r,t). For fusion research, fluid models provide a fairly accurate description of most important phenomena (macro balance and stability, transport, heating, and current drive). Although the physical properties of some important phenomena require a kinetic model, the fluid model is still an ideal fusion research framework. It should be notice that the kinetic model and the fluid model are not two separate descriptions. The fluid model can be strictly derived from the moments of the kinetic model. The moment processing always makes the number of unknowns of the system more than the number of equations. Therefore, the system must be closed by some form of mathematical expansion based on some physical considerations. That is, the number of equations is equal to the number of unknowns. In this chapter, we will first give the kinetic model equation, then use the formal mathematical moment processing to obtain the fluid model, and then simplify it according to the plasma characteristics of the SOL region to obtain a simple two-point model. Finally, the physical model of plasma off-target will be introduced. The plasma consists of ions and electrons, and the individual particles are subjected to Lorentz forces:

$$m\frac{\partial \vec{v}}{\partial t} = q\left(\vec{E} + \vec{v} \times \vec{B}\right) \quad (2.1.1)$$

In general, the particle number of tokamak plasma can up to 10^{20}, this would be the number of equations to be solved. It is impossible to solve Lorentz equation for every particle, especially these particles are also coupled to each other. So the probability density function $f(\vec{r},\vec{v},t)$ used for kinetic description. In this case we should solve the Boltzmann equation:

$$\frac{\partial f}{\partial \mathrm{t}} + \vec{v}\cdot\vec{\nabla}_r f + \vec{a}\cdot\vec{\nabla}_v f = \left(\frac{\partial f}{\partial \mathrm{t}}\right)_C \quad (2.1.2)$$

Here, $\left(\frac{\partial f}{\partial t}\right)_C$ represents the effect of collisions to probability density function. Substituting the Lorentz forces into Boltzmann equation (2.1.2), the Vlasov-Landau equation has been obtained:

$$\frac{\partial f}{\partial t} + \vec{v}\cdot\vec{\nabla}_r f + \frac{q}{m}\left(\vec{E} + \vec{v}\times\vec{B}\right)\cdot\vec{\nabla}_v f = \left(\frac{\partial f}{\partial t}\right)_c \quad (2.1.3)$$

Here, $\vec{E}$ and $\vec{B}$ are external field, because the interaction between partiles has been accounted in collisional term, $\left(\frac{\partial f}{\partial t}\right)_c$.

For now, it is still numerically very expensive to simulate a tokamak plasma with a fully kinetic, 2-D code including the interaction between wall and plasma. Then a further simplification has been done for Vlasov-Landau equation. By calculating the moments of terms in Vlasov-Landau equation, the fluid equations have been obtained, continuity equation, momentum conservation equation and energy equation, corresponding to the moments order 0, 1 and 2.

The moment of order k is defined as below:

$$M_k = \int_v f\vec{v}^k d\vec{v} \quad (2.1.4)$$

Here, $\vec{v}^k = \otimes_{i=1}^{k}\vec{v}$.

Multiplying by $\vec{v}^k$ and integrating Vlasov-Landau equation(2.1.3) over $\vec{v}$, one obtains:

$$\int_v \frac{\partial f}{\partial t}\vec{v}^k d\vec{v} + \int_v \left(\vec{v}\cdot\vec{\nabla}_x f\right)\vec{v}^k d\vec{v} + \int_v \left(\frac{\vec{F}}{m}\cdot\vec{\nabla}_v f\right)\vec{v}^k d\vec{v} = C_k \quad (2.1.5)$$

Here, $\vec{\mathrm{F}}$ represents Lorenze force, $\vec{F} = q\left(\vec{E} + \vec{v} \times \vec{B}\right)$. The collision contribution $C_k$is defines as:

$$C_k = \int_v \left(\frac{\partial f}{\partial t}\right)_c \vec{v}^k d\vec{v} \quad (2.1.6)$$

The detailed derivation of the fluid equations has been skipped in this thesis. The fluid equations and definition of the important quantities have been shown below. First, the continuity equation has obtained with moments of order 0:

$$\frac{\partial n}{\partial t} + \vec{\nabla} \cdot n\vec{u} = 0 \quad (2.1.7)$$

The collisions do not create or destroy particles, $C_1 = 0$. Here, n is density for a specie and $\vec{u}$ is fluid velocity

$$n = M_0 = \int f d\vec{v} \quad (2.1.8)$$

$$\vec{u} = \frac{M_1}{n} = \frac{1}{n}\int \vec{v} f d\vec{v} \quad (2.1.9)$$

Then the momentum conservation equation obtained by moments of order 1:

$$\frac{\partial n\vec{u}}{\partial t} + \vec{\nabla} \cdot \left(n\vec{u} \otimes \vec{u} + \frac{\Pi}{m}\right) - n\frac{\vec{F}}{m} = 0 \quad (2.1.10)$$

As Coulombian interaction is an elastic collision, particle momentum conserves, $C_1 = 0$. The pressure tensor Π is deined as:

$$\Pi = m\int (\vec{v} - \vec{u}) \otimes (\vec{v} - \vec{u}) f d\vec{v} \quad (2.1.11)$$

Π can be divided into two parts: $\Pi = p\,\mathbb{I} + \Xi$. The first term in right side is isotropic pressure p, given by $\mathrm{p} = \mathrm{Tr}(\Pi)/3$, with $\mathrm{Tr}(\Xi) = 0$.

At last, from the moment of order 2, the energy transport equation has been obtained:

$$\frac{\partial E_t}{\partial \mathrm{t}} + \vec{\nabla} \cdot (E_t\vec{u}) + \vec{\nabla} \cdot (\vec{u} \cdot \Pi) + \vec{\nabla} \cdot \vec{q} - n\vec{u} \cdot \vec{F} = C_2 \quad (2.1.12)$$

The first term is total energy E_t linked to the second moment, and can be divide into two parts:

$$\begin{aligned} E_t &= \int_v \frac{1}{2} m\vec{v} \cdot \vec{v} f(\vec{v}) d\vec{v} \\ &= \frac{1}{2} m Tr(M_2) \\ &= \frac{1}{2} nmu^2 + \frac{3}{2} p \quad (2.1.13) \end{aligned}$$

The first term is fluid kinetic energy $E_c = \frac{1}{2}nmu^2$, and the second part is internal energy U=3p/2. By multiplying velocity equation (2.1.10) by $m\vec{u}$, the kinetic energy equation is obtained:

$$\frac{\partial E_c}{\partial \mathrm{t}} + \nabla \cdot (E_c \vec{u}) + \vec{u} \cdot \vec{\nabla} \cdot \Pi - n\vec{u} \cdot \vec{F} = 0 \qquad (2.1.15)$$

Substracting Equation (2.1.15) from Equation (2.1.13), the internal energy equation has been obtained:

$$\frac{\partial U}{\partial \mathrm{t}} + \nabla \cdot (U\vec{u}) + \Pi: (\vec{\nabla} \otimes \vec{u}) + \nabla \cdot \vec{q} = C_2$$

The second and third term in left side of equation (2.1.12) is advection of energy and $\vec{q}$ is heat flux vector, deifned as:

$$\vec{q} = \frac{1}{2} m \int_v \|(\vec{v} - \vec{u})\|^2 (\vec{v} - \vec{u}) f d\vec{v} \qquad (2.1.14)$$

$\vec{q}$ is a third order moment, it will be expressed by a function of lower order moments to make the system close. Heat flux $\vec{q}$, collision contribution C_2 and tensor pressure Π can be expressed in different approches.

2.1.2 Strong collisionality assumption

In this thesis we focus on the edge plasma with high density and low temperature, called 'cold plasma', characterized by a high collisionality:

$$\lambda_c \ll L_{\parallel} \qquad (2.1.15)$$

Here, λ_c is the collisional mean-free path associated with the thermalization process due to Coulombian collisions between plasma particles, and $L_{\parallel}$ is the length of magnetic field line, characteristic length for the SOL region. For Coulombian interaction, λ_c can be evaluated as:

$$\lambda_c = \frac{1}{2n\sigma_0 ln\Lambda} \quad (2.1.16)$$

Where n is the plasma density, σ_0 is the cross section for large deflections, and Λ is the plasma parameter.

Go back to Vlasov-Landau equation (2.1.3), where $\left(\frac{\partial f}{\partial t}\right)_c$ represents the effect of collisions, and the work of Landau for the expression of this term can be found in paper [1]. In Tokamak core region, the plasma is 'hot', $\lambda_c \gg L_{\parallel}$. The collision term become secondary order, and Vlasov-Landau equation reduced to Vlasov equation:

$$\frac{\partial f}{\partial t} + \vec{v} \cdot \vec{\nabla}_r f + \frac{q}{m}\left(\vec{E} + \vec{v} \times \vec{B}\right) \cdot \vec{\nabla}_v f = 0 \quad (2.1.17)$$

For 'cold' edge plasma, the equation (2.1.3) is dominated by the collision term and can be reduced to:

$$\left(\frac{\partial f}{\partial t}\right)_c = 0 \quad (2.1.18)$$

Under the assumption of elastic collisions, the collision term $\left(\frac{\partial f}{\partial t}\right)_c$ can be expressed as Boltzman form:

$$\left(\frac{\partial f}{\partial t}\right)_{c2} = \iint (f' f_*' - f f_*) k d\vec{k} d\vec{v}_* = 0 \quad (2.1.19)$$

Then the well-known Maxwellian distribution is the distribution function for an equilibrium state of equation (2.1.19):

$$f_M = n\left(\frac{m}{2\pi k_B T}\right)^{3/2} exp\left(-\frac{m\|\vec{v} - \vec{u}\|^2}{2\pi k_B T}\right) \quad (2.1.20)$$

Here, the temperature T is defined by the internal energy, $\mathrm{U} = 3/2\, k_B n T$. With Maxwellian distribution, the pressure tensor, equation (2.1.11), can be defined as:

$$\Pi = m \int (\vec{v} - \vec{u}) \otimes (\vec{v} - \vec{u}) f d\vec{v} = k_B n T\, \mathbb{I} \quad (2.1.21)$$

with the definition of isotropic pressure, $\mathrm{p} = \mathrm{Tr}(\Pi)/3$, the perfect gas state law can be found:

$$\mathrm{p} = k_B n T \quad (2.1.22)$$

However, the heat flux is 0 with the Maxwellian distribution:

$$\vec{q} = \frac{1}{2} m \int_v \|(\vec{v} - \vec{u})\|^2 (\vec{v} - \vec{u}) f d\vec{v} = 0 \quad (2.1.23)$$

Since, the heat flux $\vec{q}$ and the collisional contributions C_i , equation (2.1.6), haven't been expressed yet. Maxwellian distribution isn't sufficient to describe the edge plasma in SOL region. Using a perturbative method to solve kinetic equation, the expression for these terms can be found, which only depends on the fluid variables n, $\vec{u}$ and T. This technique is firstly developed by Chapman and Enskog [2], and then improved by Spitzer-Härm [3]. The following is a briefly overview of this perturbative method.

In the analysis, the distribution function has been developed as:

$$f = \frac{1}{\varepsilon} f^{(0)} + f^{(1)} + \varepsilon f^{(2)} + \cdots \quad (2.1.24)$$

where ε is a small parameter. And the kinetic Vlasov-Landau equation (2.1.3) can be written as:

$$\xi(f) = J(ff_*) + \mathcal{D}f = 0 \quad (2.1.25)$$

Here, J is the collision operator and $\mathcal{D}$ is the advection operator

$$\mathcal{D}f = \frac{\partial f}{\partial t} + \vec{v} \cdot \vec{\nabla} f + \vec{a} \cdot \vec{\nabla}_v f$$
$$J(ff_*) = \iint (f' f_*' - ff_*) k d\vec{k} d\vec{v}_*$$

Substituting equation (2.1.24) into collision term (2.1.25), an infinite series of equations have been obtained:

$$\xi^{(0)}\left(f^{(0)}\right) = 0 \quad (2.1.26)$$
$$\xi^{(1)}\left(f^{(0)}, f^{(1)}\right) = 0 \quad (2.1.27)$$
$$\xi^{(2)}\left(f^{(0)}, f^{(1)}, f^{(2)}\right) = 0 \quad (2.1.28)$$

The detailed derivation presented in refer [4]. The solution of the first equation (2.1.26) of order-0 is Maxwellian distribution. A net heat flux can be obtained from the equation (2.1.17) of order-1:

$$\vec{q}_{SH_e} = -3.16 \frac{nT_e \tau_e}{m_e} \vec{\nabla} T_e = -3.16 \frac{3.5 \cdot 10^4}{Z(ln\,\Lambda/10)} \frac{T_e^{5/2}}{m_e} \vec{\nabla} T_e \quad (2.1.29)$$
$$\vec{q}_{SH_i} = -3.9 \frac{nT_i \tau_i}{m_i} \vec{\nabla} T_i = -3.9 \frac{1.5 \cdot 10^6}{Z^3(ln\,\Lambda/10)} \frac{T_i^{5/2}}{m_p} \vec{\nabla} T_i \quad (2.1.30)$$

Where τ represents the mean collisional time, m_p represents the proton mass, Z represents the atomic number of the ions and lnΛ is the Coulomb logarithm. It should be noticed that, the dependence of $T^{5/2}$ make the conductive heat flux very high for elevated temperature. Under the assumption of $T_e = T_i$, conductive heat flux though electron occupies the dominant position, $\vec{q}_{SH_e}/\vec{q}_{SH_i} \approx m_i/m_e$. Since this work doesn't consider effect of magnetic field, the equations (2.1.29-2.1.30) can't be used in perpendicular heat flux. This perturbative method can also be used to evaluate the pressure tensor.

[1] L. Landau. Die kinetische Gleichung für den Fall Coulombscher Wechselwirkung. Phys. Z. Sowjet., 10, 1936. Translation: The transport equation in the case of Coulomb interactions, in D. ter Haar, ed., Collected papers of L.D. Landau, pp. 163-170. Pergamon Press, Oxford, 1981. 21
[2]S. Chapman and T. G. Cowling, The Mathematical Theory of Non-Uniform Gases, Cambridge University Press 1939.

[3] L. Spitzer and R. Härm, Transport phenomena in a completely ionized gas, Phys. Rev. , 89, March 1953, 977.
[4] S. Chapman and T.G. Cowling. The Mathematical Theory of Non-uniform Gases. Cambridge University Press, 1939. 11, 26, 27, 29, 30, 31, 32, 33, 34

2.1.3 Plasma-Wall interaction

When the plasma interacts with the solid, a recombination process occurs. Most of the electron ions recombined on the wall are reinjected into the plasma in the form of neutral particles. This balance of particle flow is referred to as plasma recycling. The quasi-neutral principle is no longer valid, because the electron mobility is higher than ion, so the potential of wall is negative. The ions are attracted by the negative potential, and a positive charge is accumulated near the surface to form a charge shield. This very thin layer of net charge formed on the solid surface is called the sheath. The sheath is also a kind of Debye shielding, the general thickness is Debye length. Because the Debye length is much smaller than the collision mean free path, the sheath can be considered as collision free.

Back to the momentum equation (2.1.10), assuming that the electron mass is negligible, the electron momentum equation along the magnetic field line can be written as:

$$\nabla_{\parallel} p_e = -n_e e E_{\parallel} \quad (2.1.31)$$

Here, the subscript parallel symbol indicates the physical quantity along the magnetic line. According to the Maxwellian distribution (2.1.22), the momentum equation can be expressed in terms of temperature density and potential:

$$k_B \nabla_{\parallel} n_e T_e = n_e e \nabla_{\parallel} \phi \quad (2.1.32)$$

Solving the above formula can get the so called Boltzmann distribution of electrons.
Here, ϕ_{se} n_{se} represent the potential and density of the sheath inlet:

$$n_e = n_{es} \exp\left(\frac{e(\phi - \phi_{es})}{k_B T_e}\right) \quad (2.1.33)$$

Assume that the ion temperature is very low, $T_i \rightarrow 0$. The random motion speed of ion is zero, $v_i = u_i$. The relationship between ion velocity and potential in the sheath is:

$$\frac{1}{2} m_i v^2 = -e\phi$$

Continue to assume that the ion current is constant under steady state conditions, $nv = const$, and the ion density can be obtained by combining the Botlmann distribution (2.1.33):

$$n_i = n_{se}\frac{v_{se}}{v} = n_{se}\sqrt{\frac{\phi_{se}}{\phi}} \quad (2.1.34)$$

Substituting equation (2.1.33-34) into Poisson equation,$\nabla^2\phi = \frac{q}{\varepsilon_0}(n_e - n_i)$, the relationship between potential and electron density have been obtained:

$$\frac{d^2\phi}{dx^2} = -\frac{en_{se}}{\varepsilon_0}\left[\sqrt{\frac{\phi_{se}}{\phi}} - \exp\left(\frac{e(\phi-\phi_{es})}{k_B T_e}\right)\right] \quad (2.1.35)$$

Replace the potential with Δ, $\varDelta = \phi_{es} - \phi < 0$:

$$\sqrt{\frac{\phi_{se}}{\phi}} \approx 1 + \frac{1}{2}\frac{\varDelta}{\phi_{es}} = 1 - \frac{1}{2}\frac{\varDelta}{|\phi_{es}|}$$

$$\exp\left(\frac{e(\phi-\phi_{es})}{k_B T_e}\right) = 1 - \frac{e\varDelta}{k_B T_e}$$

Transform the equation (2.1.35) into a differential equation forΔ:

$$\frac{d^2\varDelta}{dx^2} \approx \frac{en_{se}\varDelta}{\varepsilon_0}\left(\frac{e}{k_B T_e} - \frac{1}{2|\phi_{es}|}\right) \quad (2.1.36)$$

If this differential equation has a non-oscillation solution, the following conditions must be met:

$$\frac{e}{k_B T_e} - \frac{1}{2|\phi_{es}|} > 0 \quad (2.1.37)$$

also called the Bohm criterion:

$$v_{se} \geq c_s \quad (2.1.38)$$
$$c_s = \sqrt{\frac{k_B T_e}{m_i}}$$

The above inference is derived by ignoring the ion temperature. If we consider the ion temperature, the expression of sound speed is given by:

$$c_s = \sqrt{\frac{k_B(T_e + \gamma T_i)}{m_i}} \quad (2.1.39)$$

$\gamma = 1$ if the plasma is isothermal, γ=5/3 if the plasma is adiabatic and isotropic. The Ion flux to target can be expressed by:

$$\Gamma_{se} = nv_{se} \geq nc_s \approx n\sqrt{\frac{k_B(ZT_e + \gamma T_i)}{m_i}}$$

Since the sheath region does not collide, the heat flux is in the form of convection:

$$q_e = \gamma_e k_B T_e \Gamma_{se} \quad (2.1.40)$$
$$q_i = \gamma_i k_B T_i \Gamma_{se} \quad (2.1.41)$$

Here, $\gamma_e \gamma_i$ are sheath transmission coeficients and should be calculated using kinetic approach [5]:

$$\gamma_i = 2.5\frac{T_i}{T_e} - \sim 0.5$$
$$\gamma_e = \frac{2}{1-\delta_e} - 0.5\ln\left[\left(2\pi\frac{m_e}{m_i}\right)\left(1+\frac{T_i}{T_e}\right)(1-\delta_e)^2\right] + \sim 0.5$$

Usually people use simple forms:

$$\gamma_i = 2.5$$
$$\gamma_e = 4.5$$

[5] P. C. Stangeby, The Plasma Boundary of Magnetic Fusion Devices, Bristol and Philadelphia, Institute of Physics Publishing 2000

2. Simple two point model

Since there are many different mechanisms in edge plasma model and the geometry of flux surface and realistic wall is complex, complex advanced tools for the edge plasma modeling have been developed to understand the plasma behavior in SOL region. Most of them are 2-D or 3-D codes, dividing the computational region into many fine grids, solving a set of fluid equations, based on some simplifications on numerical or physics. In this thesis, SolEdge2D code has been used to provide solutions for particle and energy transport in the edge plasma within complex and realistic 2D geometries and will be introduced in section 3. However, when using these codes people needs always more simplified models in order to analyze the outputs of the codes, in order to avoid lack of clear physical significance of the plasma transport in SOL region. The two-point model is a 1-D simplified SOL plasma transport model, it can used to predict the results of the edge plasma problems and judge the reliability of the outputs from the simulation code. In this section, the basic two-point model will be described and the

The two-point model focuses on the plasma parallel transport in SOL region. As shown in figure 2.2.1, a thin magnetic tube has been chosen and be straighten and the two-point model relate plasma parameters at two points. The first point is upstream point: the model assumes that the particle and heat flux flew from core plasma to SOL region through this point. Then the target point where the heat and particle flux strike the divertor target. The subscripts A_u and A_t correspond to the value taken by the quantity A at respectively upstream positions (midplane) and target positions (divertor surface). In two-point model the parallel coordinate has been used.

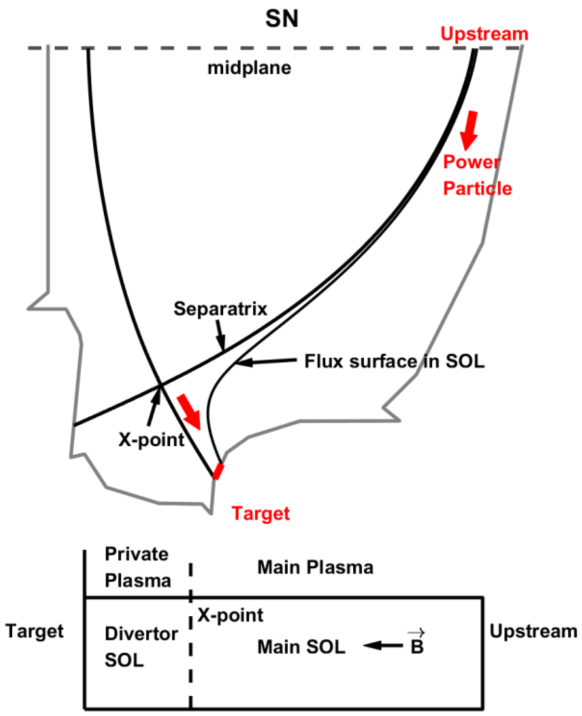

Figure 2.2.1 Schematic geometries of parallel heat/particle flux transport tube between separatrix and a closely flux surfaces in the SOL, from the upstream (outer midplane) to the outer target. Red arrows indicate the heat/particles flux.

Using some simplifications of thermal transport and particle flow process, the two-point model can be derived from fluid model. At first, the two-point model only has two species:

electron and Ion. We assume that the temperature of electron and ion is same, $\mathrm{T} = T_e = T_i$. It should be noticed that the temperature of them is obviously different because of the low collisonality and the date from experiment can also support it. In two-point model, the cross field transport has not been taken into account and the sink of particles, momentum and energy is zero in calculation region.

In steady state assumption, the parallel component of momentum conservation equation from fluid model can be expressed as:

$$\vec{\nabla} \cdot \left(n\vec{u} \otimes \vec{u} + \frac{\Pi}{m} \right) \cdot \vec{b} + n\frac{q\left(\vec{E} + \vec{v} \times \vec{B}\right)}{m} \cdot \vec{b} = 0$$

Here, the $\cdot \vec{b}$ is the unit vector of magnetic direction. It's clearly that the term of $\vec{v} \times \vec{B}$ is vanished because of the $\left(\vec{v} \times \vec{B}\right) \cdot \vec{b} = 0$. For terms of $\vec{E}$, using the principle quasi-neutrality $n_e \approx n_i$, the conributions from electron and ion can cancel each other out. Ignore the perpendicular component of transport and velocity, the momentum conservation equation for two-point model can be expressed as:

$$\nabla_{\parallel}\left(2nT(1 + M^2)\right) = 0$$

Here, M is the Mach number, $\mathrm{M} = u/c_s$, $c_s = \sqrt{(T_i + T_e)/m_i}$. Because of the Bohm boundary condition, equation (2.1.38), at the sheath entrance $\mathrm{M} \geq 1$. Since the length of sheath is very small compared to the parallel length $L_{\parallel}$, we can set that $M_t = 1$ at target point. We assume that the upstream point is stagnation point, $M_u = 0$. The pressure conservation equaiton of two-point model has been obtained:

$n_u T_u = 2n_t T_t$ (2.2.1)

Consider the energy conservation equation (2.1.12), using the same kind of assumption,

$$\left(\vec{\nabla} \cdot (E_t\vec{u}) + \vec{\nabla} \cdot (\vec{u} \cdot \Pi) + \vec{\nabla} \cdot \vec{q}\right) \cdot \vec{b} = 0$$

Neglecting the stress tensor, we obtain:

$$q_{\parallel} + \left(\frac{5}{2}p + \frac{1}{2}mnu^2\right)u = constant$$

Here, two-point model assume that the conduction heat flux is the dominant transport mechanism in calculation region, except the sheath neat the target. Then the parallel heat flux can be expressed as:

$$q_{\parallel} = -\kappa_0 \frac{2}{7} \nabla_{\parallel} T_e^{7/2} \quad (2.2.2)$$

Where Spitzer conductivity $\kappa_0 \approx 2000$. The parallel ion conduct component has been neglected, very small compared to the electron conduction term. This expression is supposed to hold along the main fraction of SOL field lines and assume the $q_{\parallel}$ is constant. Intergrating the gradient along the length of the field lines $L_{\parallel}$, between upstream and target point:

$$T_u^{7/2} = T_t^{7/2} + \frac{7 q_{\parallel} L_{\parallel}}{2\kappa_0} \quad (2.2.3)$$

Here, $L_{\parallel}$ represent the parallel length from uptream to target.

The second expression of heat flux is sheath transmission. From the appropriate description of the kinetic distribution functions of electrons and ions in the potential gradient taking place in that region, the fluid heat load flowing through the sheath separating the quasi-neutral plasma and the divertor surface expressed as:

$$q_{\mathrm{t}} = \gamma c_s n_t T_t = C n_t T_t^{3/2} \qquad (2.2.4)$$

$$C = \frac{\gamma \sqrt{Z + a}}{\sqrt{m_i}}$$

where $\gamma \approx 5 + 2.5\alpha$ is called the sheath transmission coefficient. We do the approximation that electron and ions are thermalized, i.e. $T_e = \alpha T_i$ with α constant along field lines. It takes into account both electron and ion heat load, including sheath acceleration of ions and repulsion of a fraction of the electrons. It depends on the ion to electron temperature ratio, but to limit the number of parameters. Here it assumes that $T_e = T_i$ and Z=1, we therefore have ≈ 7.5 $\beta = \gamma\sqrt{2/m_i}$.

In simple two-point model, the volumetric power losses hasn't been consiered:

$$q_{\mathrm{t}} = q_{\parallel} \quad (2.2.5)$$

These three equations, equations (2.2.1,2.2.3, 2.2.4) make up the simple two-point model. It should be noticed that the particle conservation has not been considered, because the all particles has been imposed to inject the SOL region from upstream point and the particles don't have a parallel velocity at upstream point.

The upstream density n_u and power $q_\parallel$ are the input parameters, the upstream temperature T_u is considered as output, whereas the target variables are only intermediates. Considering the power balance at upstream, the total power transported from the core plasma into the scrape off layer P_{sep}, is supposed to flow along the field lines in a layer of radial width, exponential power scrape-off width λ_q. To get rid of geometrical effects due to magnetic flux expansion, field line mapping of the heat load pattern from the divertor to the midplane is performed. The $q_\parallel$ can be expressed as:

$$\frac{1}{2}P_{sep} = 2\pi R\lambda_q q_\parallel \frac{B_\theta}{B_\phi} \qquad (2.2.6)$$

Here, R represent the radius of upstream point, B_θ and B_ϕ denote poloidal and toroidal components of the magnetic field. Since the density at uptream point n_u can be related to the mean plasma density and the $q_\parallel$ can be expressed with the inject power. It suggests that the two-point model can be used to control the performance of dischage, because these input quantities $q_\parallel$ and n_u are operating parameters for a tokamak, the two-point model can be used to predict the target parameters.

According to the difference between temperature and pressure on upstream and target point, it is possible to distinguish three different regimes of SOL plasma: sheath-limited, high-recycling and detached regime.

Defining a reference temperature $T_Q = \left(\frac{7q_\parallel L}{2\kappa_0}\right)^{2/7}$, the equation (2.2.3) can be expressed as:

$$\left(\frac{T_u}{T_t}\right)^{7/2} = 1 + \left(\frac{T_Q}{T_t}\right)^{7/2} \qquad (2.2.7)$$

The sheath limit regime is also referred to as a low-recycling state. When the plasma density in target point is much higher than T_Q, $T_t \gg T_Q$. the temperature difference between the upstream and target is small, that is:

$$T_u \approx T_t = \left(\frac{q_{\parallel}}{Cn_t}\right)^{2/3} = \left(\frac{2q_{\parallel}}{\gamma n_u}\sqrt{\frac{m_i}{2}}\right)^{2/3} \quad (2.2.8)$$

From the criterion of sheath limit regime, $T_t \gg T_Q$, the uptream density for high-recycling regime can be expressed as:

$$n_u \ll 2\frac{{q_{\parallel}}^{4/7}}{C}\left(\frac{7L}{2\kappa_0}\right)^{-3/7} \quad (2.2.9)$$

When the plasma density is low, there is no energy loss during the transport along the magnetic field lines. Due to the presence of the sheath, the electron flux reaching the divertor target plate is reduced, and the sheath becomes a domain that limits the size of the conduction heat flux, so it is called a sheath limited. The momentum loss caused by charge exchange in the SOL region is small, and the plasma pressure remains conserved along the magnetic field lines, substituting equation (2.2.8) into equation (2.2.1), obtained:

$$n_t = n_u/2 \quad (2.2.10)$$

It is clearly that the plasma density at the target increases linearly with the increase in the density of the main plasma, so the sheath limit regime is also called a linear state. In the sheath limited regime, the plasma temperature is high near the target plate, the heat flow is large, and thus impurities are sputtered much. The future reactor will not adopt this operating state. In the case of medium plasma density and heating power, the plasma temperature in the SOL region is relatively low, and the limited plasma conductivity causes a large temperature gradient between the upstream and the target plate, but the pressure in the SOL region along the magnetic field line remains conserved. This state is called a thermal conduction limited or a high-recycling regime. In this case, we still assume that the divertor plasma temperature is high enough, the friction process is negligible, and the energy loss is small. Then we derive the target parameter expression.

Based on $T_u \gg T_t$, the conduction expression of heat flux, equation (2.2.7), is simplified:

$$T_u = T_Q = \left(\frac{7q_{\parallel}L}{2\kappa_0}\right)^{2/7} \quad (2.2.11)$$

Then combined the pressure conservation equation (2.2.1) and sheath transmission heat flux equation (2.2.4), we get:

$$n_t = \frac{n_u^3 T_u^3 C^2}{8q_\parallel^2} \propto \frac{n_u^3 L_\parallel^{6/7}}{q_\parallel^{8/7}} \qquad (2.2.12)$$

$$T_t = \frac{4q_\parallel^2}{n_u^2 T_u^2 C^2} \propto \frac{q_\parallel^{10/7}}{n_u^2 L_\parallel^{4/7}} \qquad (2.2.13)$$

$$\Gamma_i \propto n_t\sqrt{T_t} \propto \frac{L_\parallel^{4/7}}{q_\parallel^{3/7}} n_u^2 \qquad (2.2.14)$$

$$with\ C = \frac{\gamma\sqrt{2}}{\sqrt{m_i}}$$

It shows that in high-recycling regime, the temperature and density at the target point are determined by the upstream density n_u and heat flux $q_\parallel$. From equation (2.2.12), the plasma density at the target plate n_t is proportional to the cube of the upstream density n_u. When the n_u increases, the plasma density near the divertor increases rapidly, which reflects that there is strong particle recycling near the divertor target. Equation (2.2.13) shows that the plasma temperature at the target T_t is inversely proportional to the square of the n_u, ie $T_t \propto n_u^{-2}$, which can be reduced by increasing the upstream plasma density. The equation (2.2.14) shows that with the increasing upstream density, the particle flux rises rapidly, and since the total power is constant, it can effectively reduce the energy carried by each particle and then reduces the sputtering of the target.

In high-recycling regime, the temperature near the target plate is lower and the particle flux is higher, which can effectively reduce the impurity yield, enhance the shielding effect of the divertor, and help to pump impurities and ash generated in the fusion reactor. With the plasma ramp, the edge plasma transitioned from a sheath-limited to high-recycling regime, until the plasma detached.

Based on the criterion of reaching high-recycling regime, $T_u \gg T_t$, the uptream density for high-recycling regime can be expressed as:

$$n_u \gg 2\frac{q_\parallel{}^{4/7}}{C}\left(\frac{7L}{2\kappa_0}\right)^{-3/7} \qquad (2.2.15)$$

From this equation, we can see that increasing upstream density can reach high-recycling regime, and a higher inject power will elevate the threshold.

When the plasma density is high or the radiation loss is large, the plasma temperature of the divertor is sufficiently low (<5 eV), the ionization process is small, and the friction effect of charge exchange and elastic collision between ion and neutral particles is obviously. Due to the momentum loss, the plasma pressure in the recycling area is no longer conserved, and this state is called the detached regime. The plasma density and temperature on the target plate decrease as the upstream density ramp. There are five ways to achieve plasma detachment [5]:

1. Increase plasma impurity content by boundary impurity inject.
2. Inject higher emissivity impurities, ie increase the radiant power:
3. Increase the density of the upstream plasma
4. Increase the connection length of the SOL area. From 2-point model, equation (2.2.13), the upstream density for detachment onset, Tet $\sim$ 5 eV, is expected to scale as $\propto L_{\parallel}^{-4/7}$. We would expect a reduction in threshold density for detachment with in increasing $L_{\parallel}$, through the terms of $L_{\parallel}^{-4/7}$.
5. By increasing the core plasma radiation, reduce the input power of SOL region.

Nowadays, people use one-dimensional model to analyze the plasma detachment [6,7], and has a deep understanding of this process. Plasma detachemnt is the condition that the temperature of the target plate is sufficiently low, the volume recombination and the friction of the ion-neutral atom collision on the plasma flow reduce the heat flow and the particle flow at the target plate, thereby the plasma 'detached' from the target plate. The plasma detachment can effectively reduce the heat flux to the surface of the target plate, reduce the damage to the target material, and provide an excellent operation mode for the nuclear fusion reactor.

The two-point model can't be used in detached regime, because there is no source term in the mass conservation equation which can take into account the ionization of the neutrals. Moreover, the sink terms in momentum and energy conservation are also necessary for detachment plasma modeling.

[5] C. S. Pitcher and P. C. Stangeby, Experimental divertor physics. Plasma Phys. Control. Fusion 39(6), 779-930 (1997)

[6] Rajiv Goswami et al,. One-dimensional model of detached plasma in the scrape-off layer of a divertor tokamak. Plasma Phys. 8(3), 857-870 (2001).

[7] V. Kotov and D. Reiter, Two-point analysis of the numerical modelling of detached divertor plasma. Plasma Phys. Control. Fusion 51(11), 115002 (2009)

3. Modified two point model

Considering the effect of neutral particles, keeping the two-point model as simple before, three corrective factors have been introduced to take into account the different physical phenomenons between neutal particles and plasma [6]: $f_{power}, f_{mom}, f_{cond}$. It should be noticed that the modification is focus on the high-recycling regime.

Two main processes causes volumetric power losses near the target: impurity radiation, q_{rad}^{SOL}, and charge exchange with the neutral particles, q_{cx}^{SOL}. In general, q_{cx}^{SOL} is smaller than q_{rad}^{SOL}. The power loss factor f_{power} defined to express the effect of these two prosesses:

$$f_{power}q_{\parallel} = q_{rad}^{SOL} + q_{cx}^{SOL} \quad (2.3.1)$$

The sheath transmission heat flux, equations (2.2.4-5), expressed as:

$$\left(1 - f_{power}\right)q_{\parallel} = q_{\mathrm{t}} = \gamma c_s n_t T_t \quad (2.3.2)$$

It is clearly that f_{power} can obvously reduce the temperature and heat flux on target and the larger is better.

The frictional collisions with neutrals, viscous forces and volume recombination will cause momentum loss in palsma flow. To express this process, the f_{mom} is defined as:

$$f_{mom}P_u = P_t$$

Here, P_u and P_t represent the pressure on uptream and target point. Then the pressure balance equation (2.2.1) can be expressed as:

$$f_{mom}n_u T_u = 2n_t T_t \quad (2.3.3)$$

In simple two-point model, it assumes that the heat flux in SOL is dominated by conductive component. Considering the effect of convective term, the conductive factor f_{cond} is defined by the relationship:

$$f_{cond}q_{\parallel} = q_{\parallel,\,cond}$$

The conduction heat flux along the magnetic line, equation (2.2.3), can be expressed as:

$$T_u^{7/2} = T_t^{7/2} + \frac{7f_{cond}q_{\parallel}L_{\parallel}}{2\kappa_0} \quad (2.3.4)$$

Here, the f_{power} hasn't been used because the power loss is assumed just occurs near the target.

Then combining the three modified two-point model equations (2.3.2-4), the modified expression with three correction factors obtained:

$$T_u = \left(\frac{7 f_{cond} q_{\parallel} L}{2\kappa_0}\right)^{\frac{2}{7}} \quad (2.3.5)$$

Here, T_u is also greater than T_t, and modefied by f_{cond}, $T_u \propto f_{cond}^{2/7}$.

Taking into account the effect of the total flux expansion $f_R = B_u/B_t \approx R_t/R_u$, the modified 2-point model [29] is given by:

$$n_t \propto \frac{n_u^3 L_{\parallel}^{6/7}}{q_{\parallel}^{8/7}} f_R^2 \left(\frac{ln f_R}{f_R - 1}\right)^{6/7}$$

$$T_t \propto \frac{q_{\parallel}^{10/7}}{n_u^2 L_{\parallel}^{4/7}} \frac{1}{f_R^2} \left(\frac{ln f_R}{f_R - 1}\right)^{-4/7}$$

This model shows that increasing f_R can shift the detachment onset towards lower upstream density and enhance the detachment control performance [18].

[6] Stangeby P C 2000 The Plasma Boundary of Magnetic Fusion Devices (Bristol: IOP Publishing)

4. Detachment

Due to the tremendous challenge of heat and particle exhaust in future tokamak fusion reactors, detachment is being extensively studied in a number of tokamaks, such as JET [5], TCV [6, 7], ASDEX Upgrade [8], DIII-D [9], JT-60U [10], C-Mod [11] and many others. Although detachment has an advantage in terms of heat flux and erosion issues on target, pushing detachment too far can lead to degradation of the pedestal pressure in H-mode and lower the overall confinement [12]. Moreover, the control of the detachment front, obtained for short time discharges in current tokamaks, remains a challenge for long pulses relevant for reactor operation.

[5] Loarte A, Monk R D and Martin-Solis J R 1998 Nucl. Fusion 38 331
[6] C. Theiler, et al 2017 Nucl. Fusion 57 072008
[7] H. Reimerdes, et al 2017 Nucl. Fusion 57 126007
[8] Kallenbach A, Dux R, Mertens V and Gruber O 1995 Nucl. Fusion 35 1231
[9] Petrie T W, Buchenauer D, Hill D N and Klepper C 1992 J. Nucl. Mater. 196–198 848
[10] Hosogane N, Asakura N, Kubo H and Itami K 1992 J. Nucl. Mater. 196–198 750

[11] Lipschultz B, Goetz J and LaBombard B 1995 J. Nucl. Mater. 220–222 50
[12] Kallenbach A et al 2015 Nucl. Fusion 55 053026

5. Alternative divertor configurations

Considering the power balance at upstream, the total power transported from the core plasma into the scrape off layer P_{sep}, is supposed to flow along the field lines in a layer of radial width, exponential power scrape-off width λ_q. To get rid of geometrical effects due to magnetic flux expansion, field line mapping of the heat load pattern from the divertor to the midplane is performed. The power flowing down the divertor can be expressed as:

$$\frac{1}{2}P_{sep} = 2\pi R\lambda_q q_{\parallel}\frac{B_\theta}{B_\phi} \qquad (9)$$

Take account in geometrical effects due to magnetic flux expansion f_x^* and the geometry of divertor target, the heat flux deposited of divertor can be expressed as:

$$q_t = \frac{R_u}{R_t}\frac{sin\beta}{f_x^*}q_{\parallel} \qquad (10)$$

β is the divertor target inclination with respect to flux surfaces and f_x^* is the volumetric flux expansion, defined as $f_x^* = \frac{\Delta r_t}{\Delta r_u} = \frac{B_{\theta,u}R_u}{B_{\theta,t}R_t} = \frac{B_{\theta,u}B_{\phi,t}}{B_{\theta,t}B_{\phi,u}}$. Here, θ and φ denote poloidal and toroidal components of the magnetic field. In the right side, α represents the total incidence angle between the magnetic field and divertor plate.

Using the definition of f_x^*, equation (10), the effect of the divertor tilt β and flux expansion f_x^* can be combined to:

$$\frac{sin\beta}{f_x} = tan\alpha\frac{B_{\phi,u}}{B_{\theta,u}}\sqrt{\frac{\left(B_{\phi,t}\right)^2+\left(cos\beta\cdot B_{\theta,t}\right)^2}{\left(B_{\phi,t}\right)^2}} \approx tan\alpha\frac{B_{\phi,u}}{B_{\theta,u}} \qquad (11)$$

The equation (11) shows that both flux expansion and divertor tilt reduce the total incidence angle between the magnetic field and divertor plate, α. However, in reactor relevant conditions with actively cooled divertors composed of castelleted plasma facing units, there is an engineering limit on how small can be the incidence angle [25]. [FN22] This necessarily means the limit of possible reduction of heat flux by wall tilt and flux expansion. With the ITER monobloc technology, a minimum indice angle of 1.5 degree is envisaged.

If we conbine the equation (5,9,11), the peak value of heat flux on the divertor can be expressed as:

$$q_t \approx tan\alpha \frac{B_{\phi,u}}{B_{\theta,u}} \frac{P_{sep}}{4\pi R_t \lambda_q} \qquad (12$$

From the equation (12), there are two ways to reduce the resulting heat flux perpendicular to the divertor plate. One possible is reduce the α by tilting the divertor plate or to increase the volume flux expansion f_x^*. And the second way is to bring the outer strikepoint to a larger major radius to increase the R_t. It should be noticed that, in reactor relevant conditions with actively cooled divertors composed of castelleted plasma facing units, there is an engineering limit on how small can be the incidence angle [25]. [FN22] This necessarily means the limit of possible reduction of heat flux by wall tilt and flux expansion. With the ITER monobloc technology, a minimum indice angle of 1.5 degree is envisaged.

As an illustration, the power exhaust in ITER with the total power to outer target $P_{sep} \cong 50MW$, power flux e-folding length $\lambda_q \approx 1mm$, $R_t \approx 6m$, $B_{\phi,u}/B_{\theta,u} \approx 3$, $\alpha \approx 3°$, we obtain from equation (12) the value of q_t, approximately 100MW, far more than engineering limits.

One possible approach to solve this problem is detachment plasma, increase the radiation in diverter volume, thus distribution of P_{sep} over the area outside the strike point. From the 2-point model equation (7), increase of parallel connection length could be beneficial to reduce the temperature on target and ease detachment access. This can be provided by lower the poloidal magnetic field in the divertor, in other world increasing the volume flux expansion. It has also been proposed that poloidal flux expansion [26] and flux flaring near the target [17] shall improve detachment stability. In this paper, we mainly discussed outer divertor, because the inner divertor area more easily enters detachment [27].

[17] Kotschenreuther M., Valanju P., Covele B. and Mahajan S. 2013 Phys. Plasmas 20 102507
[24] Petrie T.W. 2013 Nucl. Fusion 53 113024
[25] RA Pitts, S Carpentier, F Escourbiac, et al Journal of Nuclear Materials 415(1), S957-S964
[26] Lipschultz B., Parra F.I. and Hutchinson I.H. 2016 Nucl. Fusion 56 056007
[27] Loarte A. et al 1998 Nucl. Fusion 38 331–71

Chapter III: Simulation model

1. SOLEDGE-2D fluid model

The transport code SolEdge2D-EIRENE has been developed in the perspective of simulating the entire volume of edge plasma interacting with the wall in tokamaks. It is based on a standard explicit domain decomposition technique, allowing one to treat various magnetic configurations, from limiter plasma to complex double null divertor scrape-off layers, or even snowflake configurations. The computational grid has been divided first into several subdomains that are topologically different (core, SOL, Private Flux Region - PFR, and so on). Then each subdomain is further divided into several zones solved in parallel to reduce the computation wall clock time, each zone having a similar number of grid points. The specificity of the plasma solver SolEdge2D is to use an immersed boundary condition technique, termed here 'penalization', in order to enable simulations of the plasma up to the first wall in a flexible manner [1, 2]. As an illustration, the meshes of SN, SF+ and SF- configurations for the HL-2M device are plotted in figure 3, and are also used for simulations analysed later. As shown in figure 3, the SolEdge2D code relies on flux surfaces aligned meshes and these meshes are not intrinsically suitable to describe the first wall geometry, which is not aligned on the flux surfaces. Thanks to the penalization technique, we are able to overcome this issue and extend the mesh grid up to the wall, verifying Bohm boundary conditions at the plasma-wall interface. Because of the parallelization over zones, splitting the domain into a large number of zones can accelerate the speed of convergence. In its present version, the plasma module SolEdge2D simulates plasmas made of two species: singly charged ions and electrons. For each species, one solves equations for density n, parallel velocity u and temperature T. Here, the temperature unit is eV. The quasi-neutrality and ambipolarity assumptions gives $n = n_i = n_e/Z$ and $u = u_e = u_i$. Using a finite volume numerical scheme, the code solves the transport equations of mass, parallel momentum and energy, which is simplified from the 4 fluid equations as shown in chapter 2.1.

[1] L. Isoardi et al Journal of Computational Physics, Volume 229, 2010, pp. 2220-2235

[2] B. Bensiali, G. Chiavassa, J. Liandrat, Applied Numerical Mathematics, Volume 96, 2015, pp. 134-152

3.1.1 Continuity equation

From the continuity equation of fluid model, equation (2.1.7), considering the source term, the mass transport equation obtained:

$$\frac{\partial n}{\partial t} + \vec{\nabla} \cdot \left(n u_{\parallel} \vec{b} + n \vec{u}_{\perp} \right) = S^{n} \text{ (3.1.1)}$$

Where $\vec{\mathrm{b}} = \vec{\mathrm{B}}/\mathrm{B}$ indicates the unit vector in the direction parallel to the magnetic field. S^{n} is volume source of particles, includes ionization and recombination of neutral. The velocity $\vec{u}$ is decomposed to parallel component $u_{\parallel}\vec{b}$ which is determined by the parallel momentum balance, and the perpendicular part $\vec{u}_{\perp}$ is calculated by:

$$\Gamma_{\perp} = n\vec{u}_{\perp} = D\vec{\nabla}_{\perp} n \quad \text{(3.1.2)}$$

Where $\Gamma_{\perp}$ represents the particle flux of turbulent transport, D is diffusion coeficient which is obtained from the experimental radial density profile data and as a input parameter for SolEdge2D. In general, $\mathrm{D} = 0.3 \sim 3\ m^{2}/s$ for L-mode and less than 0.3 for H-mode.

3.1.2 Momentum equation

Adding the source term, the momentum equation for SolEdge2D is written as:

$$\frac{\partial n m_{e} \vec{u}}{\partial t} + \vec{\nabla} \cdot (n m_{e} \vec{u} \otimes \vec{u} + \Pi) + nZe\left(\vec{E} + \vec{v} \times \vec{B}\right) = S^{\Gamma e} \text{ (3.1.3)}$$
$$\frac{\partial n m_{i} \vec{u}}{\partial t} + \vec{\nabla} \cdot (n m_{i} \vec{u} \otimes \vec{u} + \Pi) - nZe\left(\vec{E} + \vec{v} \times \vec{B}\right) = S^{\Gamma i} \text{ (3.1.4)}$$

In SolEdge2D, the pressure tensor is simplified to its spherical part: $\Pi = p\,\mathbb{I}$. The parallel part of ion momentum equation, equation (3.1.4), can be expressed as:

$$\frac{\partial n m_{i} u_{\parallel}}{\partial t} + \vec{\nabla} \cdot \left(n m_{i} u_{\parallel} u_{\parallel} \vec{b} \right) = -\nabla_{\parallel} p_{i} + \mathrm{Zen} E_{\parallel} + S^{\Gamma i} \quad \text{(3.1.5)}$$

$$S^{\Gamma i} = \mathrm{R_{ei}} + \vec{\nabla} \cdot \left(\nu_{\parallel} \nabla_{\parallel} u_{\parallel} \vec{b} + m_{i} n \nu \vec{\nabla}_{\perp} u_{\parallel} \right) + S^{\Gamma in}$$

Here, the second term in the left, $\vec{\nabla} \cdot \left(n m_{i} u_{\parallel} u_{\parallel} \vec{b} \right)$, is parallel momentum advection. $-\nabla_{\parallel} p_{i}$ is the parallel pressure force and satisfy the perfect gas state law $p_{i} = k_{B} n T_{i}$. $\mathrm{Zen}E_{\parallel}$ is the Lorrentz force along the magnetic line. Source term $S^{\Gamma i}$ can be decomposed to 4 parts: $\mathrm{R_{ei}}$ represents the parallel force due to ion-electron collisions with the form:

$$\mathrm{R_{ei}} = -\mathrm{R_{ie}} = 0.71 Zen \nabla_{\parallel} T_{e} \quad \text{(3.1.6)}$$

$\vec{\nabla} \cdot \nu_{\parallel} \nabla_{\parallel} u_{\parallel} \vec{b}$ is parallel viscous term that is due to collisions and is reminiscent from pressure anisotropy $p_{\perp} \neq p_{\parallel}$. The Spitzer and Harm derived the expression of $\nu_{\parallel}$ [3]. Then the turbulent viscous term $\vec{\nabla} \cdot m_{i} n \nu \vec{\nabla}_{\perp} u_{\parallel}$ represents the turbulent perpendicular transport of momentum not associated with particle transport. At last, $S^{\Gamma in}$ represents the volume source of momentum due to interaction with neutrals (ionisation, recombination, charge-exchange, other momentum losses due to non-resonant collisions...). The diffusion coefficient ν should be set from comparison with experimental radial profiles of ion momentum or can easily use the value of D.

For electron, electron mass is neglected. The parallel part of electron momentum equation, equation (3.1.3), simplifies into:

$$\mathrm{ZenE}_\parallel + \nabla_\parallel p_e = \mathrm{R}_{\mathrm{ie}} \quad (3.1.7)$$

Here, $p_e = enT_e$. From this equation, the parallel electric field can be obtained:

$$\mathrm{E}_\parallel = -\frac{\nabla_\parallel p_e}{\mathrm{Zen}} - 0.71\nabla_\parallel T_e \ (3.1.8)$$

3.1.3 Energy equation

The ion and electron temperature are given by the energy transport equations. For ion, the total energy of ion can be expressed as:

$$E_{t,i} = \frac{1}{2}nmu_\parallel^2 + \frac{3}{2}enT_i \quad (3.1.9)$$

Then the energy transport equation (2.1.12) can be simplified to:

$$\frac{\partial}{\partial \mathrm{t}}E_{t,i} + \vec{\nabla}\cdot\left(E_{t,i}\vec{u} + p_i u_\parallel \vec{b}\right) = Zenu_\parallel E_\parallel + S^{E_i} \quad (3.1.10)$$

$$S^{E_i} = R_{ei}u_\parallel + \vec{\nabla}\cdot\left(\kappa_i\ \nabla_\parallel T_i \vec{b} + n\chi_i \vec{\nabla}_\perp T_i\right) + \vec{\nabla}\cdot\left(\nu_\parallel u_\parallel \nabla_\parallel u_\parallel \vec{b} + m_i n\nu u_\parallel \vec{\nabla}_\perp u_\parallel\right) + Q_{ei} + S^{E_{i,n}}$$

Where $\vec{\nabla}\cdot\left(E_{t,i}\vec{u} + p_i u_\parallel \vec{b}\right)$ represents the advection of total energy, and the parallel advective heat flux is expressed as:

$$q_{\parallel,adv,i} = \frac{5}{2}enT_i u_\parallel + \frac{1}{2}m_i n u_\parallel^3 \quad (3.1.11)$$

Back to the equation (3.1.10), on the right side, $Zenu_\parallel E_\parallel$ represents the work of electric field. S^{E_i} donates the source term and decomposed to 5 parts. $R_{ei}u_\parallel$ is the work of ion-electron collision force. $\kappa_i\ \nabla_\parallel T_i \vec{b}$ is conductive heat flux, heat conductivity $\kappa_i\ = \kappa_0\ T_i^{5/2}$. The $n\chi_i\vec{\nabla}_\perp T_i$ is turbulent perpendicular heat flux that is described by a Fourier law, the diffusivity χ_i being set empirically from radial temperature profiles. It takes values similar to D. $\nu_\parallel u_\parallel \nabla_\parallel u_\parallel \vec{b}$ is energy flux due to parallel viscosity. $m_i n\nu u_\parallel \vec{\nabla}_\perp u_\parallel$ represents cross-flield energy flux due to perpendicular turbulent viscosity. Q_{ei} is internal energy exchange term due to collisions between ions and electrons.

$$Q_{ei} = -Q_{ie} = -\frac{3}{2}\frac{T_i - T_e}{\tau_{ei}}$$

$S^{E_{i,n}}$ represents the volume energy source term due to interactions with neutrals.

Also neglecting the mass of electron, the total energy of electron expressed as:

$$E_{t,e} = \frac{3}{2} enT_e \quad (3.1.12)$$

The electron energy transport equation is following:

$$\frac{\partial}{\partial \mathrm{t}} E_{t,e} + \vec{\nabla} \cdot \left(E_{t,e} \vec{u} + p_e u_{\parallel} \vec{b} \right) = -Zenu_{\parallel} E_{\parallel} + S^{E_e} \quad (3.1.13)$$

$$S^{E_e} = R_{ie} u_{\parallel} + \vec{\nabla} \cdot \left(\kappa_i \ \nabla_{\parallel} T_i \vec{b} + n\chi_i \vec{\nabla}_{\perp} T_i \right) + Q_{ei} + S^{E_{e,n}}$$

Here, the volume energy source term $S^{E_{e,n}}$ represents the interaction of electrons with neutrals contains in particular radiation losses.

3.1.4 Boundary condition

Based on the Bohm boundary condition, at the entrance of the plasma magnetic presheath, the parallel velocity of the plasma reaches minimum sound speed:

$$u_{\parallel} \geq c_s = \sqrt{\frac{k_B (T_e + \gamma T_i)}{m_i}} \quad (3.1.14)$$

In SOLEDGE2D-EIRENE, a penalization technique using immersed boundary condition is used. The boundary condition of the energy flux at the sheath entrance:

$$q_{\parallel,\mathrm{sh},i} = \gamma_i enT_i u_{\parallel} + \frac{1}{2} m_i n u_{\parallel}^3 \quad (3.1.15)$$

$$q_{\parallel,\mathrm{sh},e} = \gamma_e enT_e u_{\parallel} \quad (3.1.16)$$

The sheath transmission coefficients γ_i and γ_e describes the effect of the sheath fliter. For ion $\gamma_i = 5/2$. For electrons, In SolEdge2D, the expresstion of γ_e is:

$$\gamma_e = \frac{2}{1-\delta_e} - 0.5\log\left(2\pi \frac{m_e}{m_i} \left[1 + \frac{T_i}{T_e} \right] \left[\frac{1}{1-\delta_e} \right]^2 \right) \quad (3.1.17)$$

Here, δ_e is the secondary electron emission rate.

[3] L. Spitzer and R. Harm. Transport phenomena in a completely ionized gas. Phys. Rev., 1953.

2. Coupling width EIRENE code

Based on a Monte-Carlo algorithm, the EIRENE code is an effective tool to simulate complex randomized process and provide detailed description of the distribution of the main quantities linked to the neutral atoms. Using the Monte-Carlo methods, it permits the kinetic description of plasma systerm with complex geometry configurations and can give access to fluid moments taking the whole kinetic effects into account. EIRENE has been coupled with many simulation codes, B2 [1, 2, 3], Edge2D [4, 5, 6, 7], OEDGE [8, 9] or EMC3 [10].

For SolEdge2D-EIRENE coupling, SolEdge2D provide plasma parameters (n, u, Te, Ti) as input to EIRENE and the ion distribution is assumed described by a shifted Maxwellian distribution with these parameters. The most neutral particles come from the wall recycling. In practice, based on the plasma flux and parameters on the wall from SolEdge2D, a truncated shifted Maxwellian distribution of ions impacting the wall and Monte-Carlo TRIM code [11] calculates the solid-particle interaction. The ion impinging the wall will be reflected to plasma or desorbed. The desorbed atoms and molecules are emitted with a temperature close to the wall temperature. The physical and chemical sputtering processes are considered. It also allows neutral particles injected from outside through the gas puff.

Then, in vacuum chamber, EIRENE calculates the neutral density n_n, neutral pressure p_n, particle source S^n in continuity equation (3.1.1), ion momentum source $S^{\Gamma i,n}$ in equation (3.1.5), energy source $S^{E_{i,n}}$, $S^{E_{e,n}}$ in equation (3.1.10,3.1.13). n_n and p_n are not used fo SolEdge2D, but help to analyzed distribution of the neutral particles. To calculate the source terms, both the electron impact processes and the heavy particles collisions are considered. The electronic collisions include ionization, dissociation and recombination. The heavy particle ones include elastic collisions and charge-exchange collisions, the latter being an elastic collision between a slow and a fast particle that exchange their charges.

In practice, EIRENE uses arbitrary triangle grids, independently of the flux surface and SolEdge2D based on flux surfaces aligned meshes. For coupling SolEdge2D with EIRENE, each SolEdge2D cell is divide into two triangles to generate the EIRENE grid, as shown in figure 3.2.1. In simulation process, through dedicated interface routines, EIRENE take the plasma parameter and flux calculate by SolEdge2D as input argument, and particle, momentum and energy sources computed by EIRENE back into SolEdge2D.

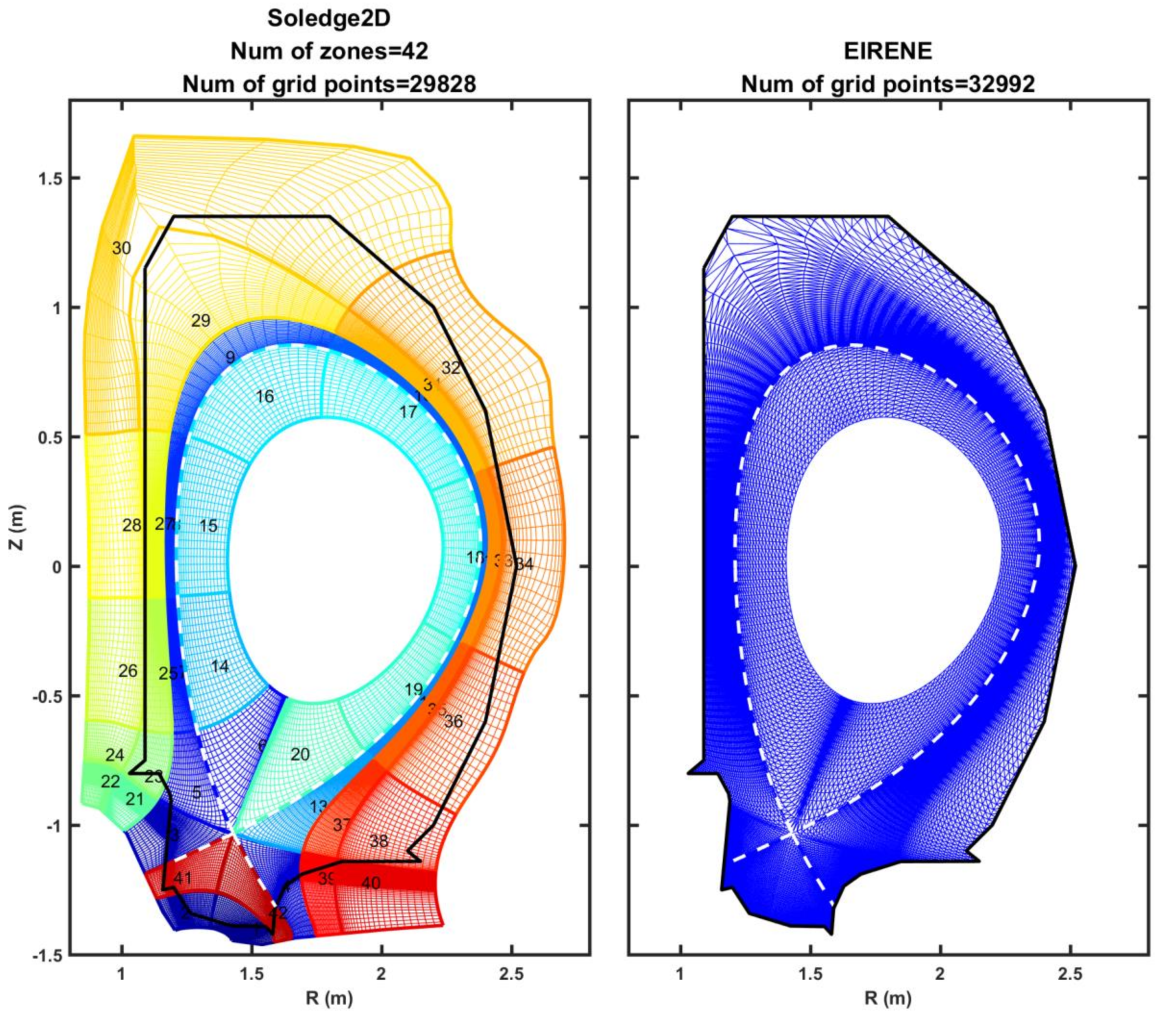
Soledge2D
Num of zones=42
Num of grid points=29828

EIRENE
Num of grid points=32992

Figure 3.2.1 SolEdge2D and EIRENE mesh of a single null configuration for HL2M.

[1] D. Reiter, M. Baelmans, and P. Börner. The EIRENE and B2-EIRENE codes. Fusion Sci. Technol., 47:172-186, 2005. 113

[2] A.V. Chankin et al. Solps modelling of asdex upgrade h-mode plasma. Plasma Phys. Control. Fusion, 48:839, 2006. 113

[3] R. Schneider, X. Bonnin, K. Borrass, D.P. Coster, H. Kastelewicz, D. Reiter, and B.J. Rozhansky, V.A. Braams. Plasma edge physics with b2-eirene. Contrib. Plasma Phys., 46:3-191, 2006. 113

[4] W. Fundamenski et al. Progress in edge plasma transport modeling on jet. Contrib. Plasma Phys., 48:190-195, 2008. 113

[5] D. Moulton, W. Fundamenski, S. Wiesen, G. Corrigan, P. Belo, G. Maddison, C. Giroud, and JET-EFDA Contributors. Edge2d-eirene modelling of the inter-elm phase of h-mode plasmas on jet. J. Nucl. Mat., 415:S509-S512, 2011. 113

[6] D. Moulton, W. Fundamenski, S. Wiesen, G. Corrigan, P. Belo, G. Maddison, C. Giroud, and JET-EFDA Contributors. Progress in Edge2d-Eirene modelling of nitrogen seeded jet plasmas. JET EFDA CP, 2010. (preprint). 113

[7] C. Guillemaut et al. Edge2d-eirene modelling of divertor detachment in jet high triangularity l-mode plasmas in carbon and be/w environment. JET EFDA CP,

2012. (preprint). 113
[8] P.C. Stangeby et al. Interpretive modeling of simple-as-possible-plasma discharges on diii-d using the oedge code. J. Nucl. Mat., 313-316:883-887, 2003. 113
[9] J.D. Elder et al. Oedge modeling of 13c deposition in the inner divertor of diii-d. J. Nucl. Mat., 337-339:79-83, 2005. 113
[10] D. Harting, S. Wiesen, H. Frerichs, D. Reiter, P. Börner, and Y. Feng. Validating the 3d edge code emc3-eirene against 2d simulations with edge2d-eirene for jet single null configurations. J. Nucl. Mat., 415:S540-S544, 2011. 113
[11] J. Ziegler. Trim and srim website (links to code manuals). http://www.srim.org/, 2012. 115

3. Soledge2D geometry

The SOLEDGE grid is based on a structured quadrangle grid aligned with magnetic flux surfaces. These meshes are not intrinsically suitable to describe the first wall geometry, which is not aligned on the flux surfaces. A solution to deal with this issue consists in using mesh reshaping near the wall, such as (partially, for the time being) implemented in different versions of SOLPS transport code [1,2]. SolEdge2D relies on another approach, the so-called 'penalization technique' [3, 4, 5], to deal with this issue without resorting to mesh reshaping near the wall. This approach does not require the grid to be aligned with the wall. More precisely, the grid is kept as orthogonal as possible, and is extended beyond the first wall into the solid. Mask functions then determine whether mesh cells belong to the plasma or to the wall. So called penalization terms are added to the Rhs of continuity equation (3.1.1), momentum equation (3.1.5), energy equation (3.1.10,3.1.13) in such a way that the desired boundary conditions are enforced at the plasma–wall interface. These penalization terms are only activated in the solid, so that no artificial sources exist in the plasma domain. This method has the advantage of being very flexible since the geometry of the wall is decoupled from the grid: changing wall geometry only requires adjusting the penalization mask, without re-gridding.

[1] Baelmans M. et al 2011 Nucl. Fusion 51 083023
[2] Klingshirn H. et al 2013 J. Nucl. Mater. 438 S856
[3] Bufferand H. et al 2013 J. Nucl. Mater. 438 S445
[4] Isoardi L. et al 2010 J. Comput. Phys. 229 2220
[5] Paredes A. et al 2014 J. Comput. Phys. 274 283

3.3.1 SolEdge2D mesh

SOLEDGE plasma equations are solved in 2D, assuming a toroidal symmetry. The simulation domain can be represented by a poloidal cross-section of the plasma. It is described by a set of two coordinates, either (R;Z) where R is the major radius and Z the vertical coordinate, or (θ; ψ) where ψ is a label of the magnetic flux surfaces (it is thus a radial coordinate) and θ is a poloidal coordinate, as shown in figure 3.3.1.

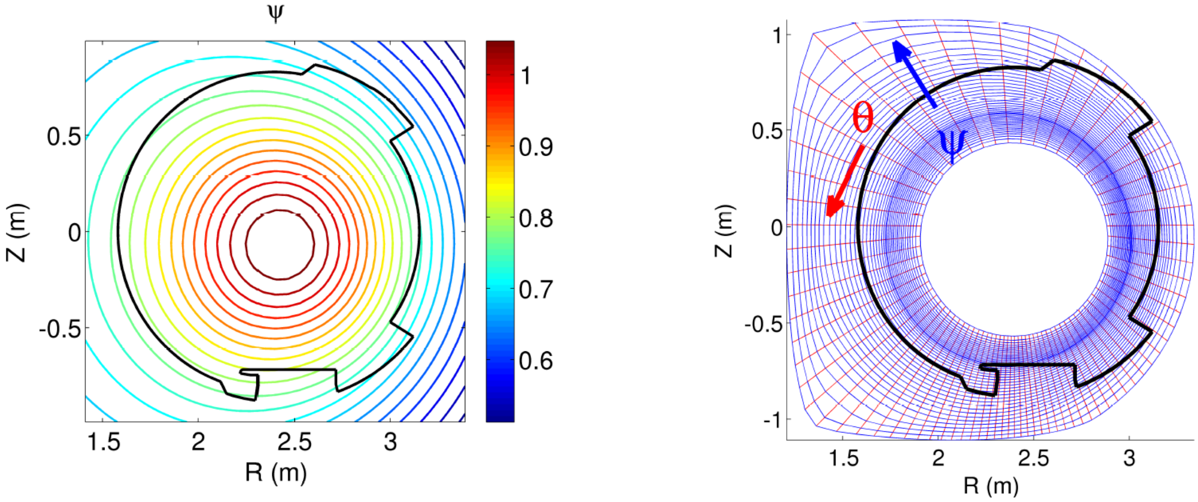

Figure 3.3.1: SolEdge2D (θ; ψ) coordinate system for a simple limiter configuration.

It SolEdge2D, the calculation domain is subdivide in a several subdomains, as shown in figure (3.3.2). Each subdomain is treated separately using parallelized process and transmit its informations to others. The boundary of the subdomain is surrounded by a set of ghost cells: these cells are filled with the fields of the neighboring subdomain, simulating the vicinity of the two zones even if they are not directly linked. While the subdomain has a wall, the ghost cells values are calculated in order to give the desired boundary conditions.

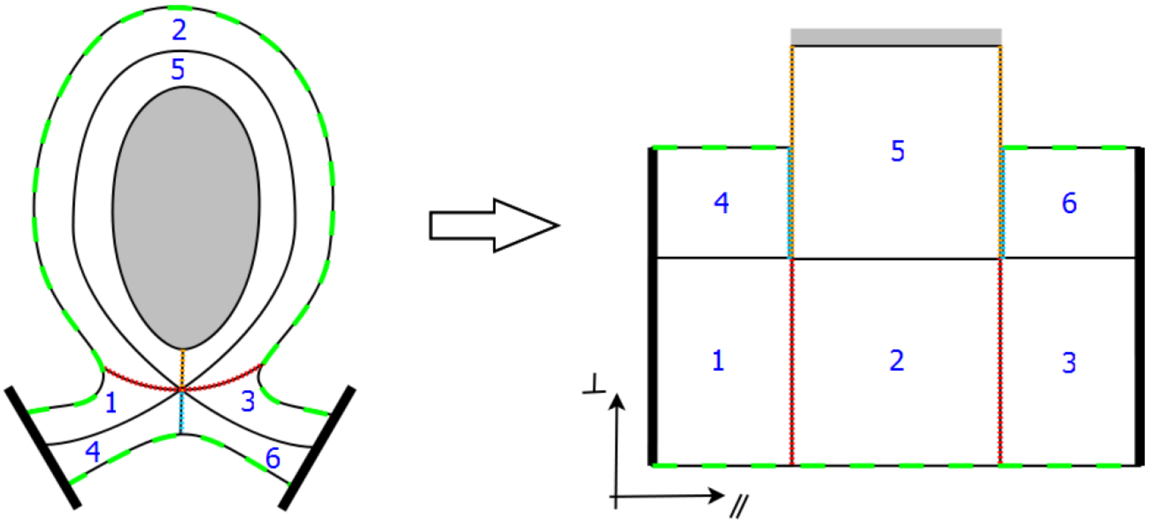

figure 3.3.2 Example of divertor configuration divided in subdomains, and transformation in a set of rectangular zones.

3.3.2 Calculating improvement

This work focused on the reduction of SOLEDGE program simulation time. We found that the convergence of calculation is time consuming and usually costs too much computation resources. For example, simulation of HL-2M device snowflake plus configuration at least need 5 months from initial condition。 Changing the boundary condition will also cost 3 months to convergence. So, it is imperative that we need a method to reduction the computation time and calculated amount, while ensuring the accuracy of results. In SOLEDGE simulation proceed, the computing time of one iteration depends on the number of grids and the iteration times for convergence relevant to the size of the minimal grid. Less grids number and bigger size of grid can effective reduce the time consumed. But a simple reduction obviously leads a low resolution of simulation results, and bad impact of the accuracy. This section presents a new method to effectively reduce the time consumed for SOLEDGE, ensuring the correctness:

First step, we generate two mesh for the same configuration with the low and high resolution, as shown in figure 3.3.3.

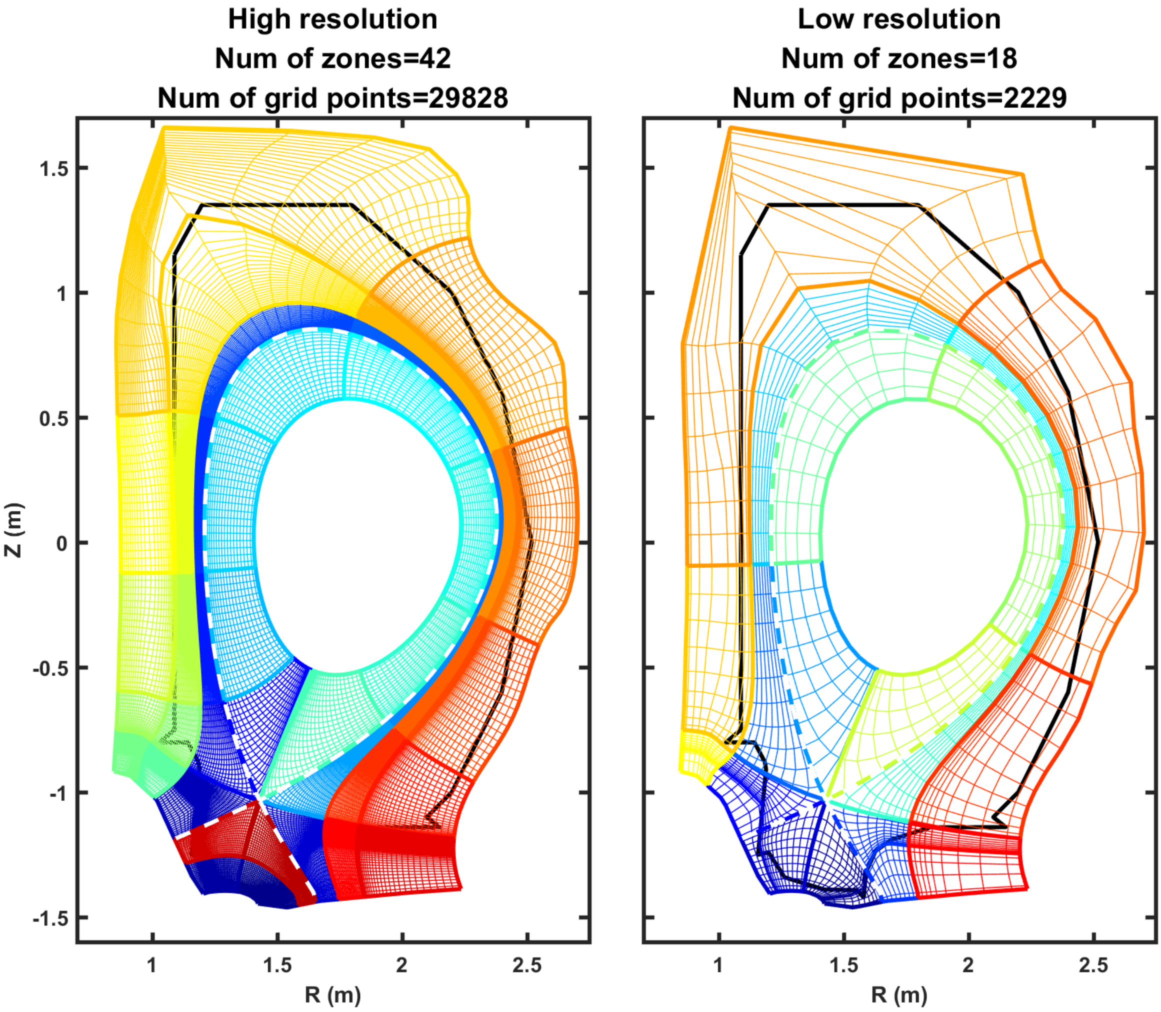

Figure 3.3.3 The mesh with high and low resolution for SN configuration.

Second step, the low-resolution mesh is used to calculate from the uniform initial condition and the results are translated to initial condition of the high-resolution grid as shown in figure 3.3.4. After a short calculation, we will get the high-resolution result.

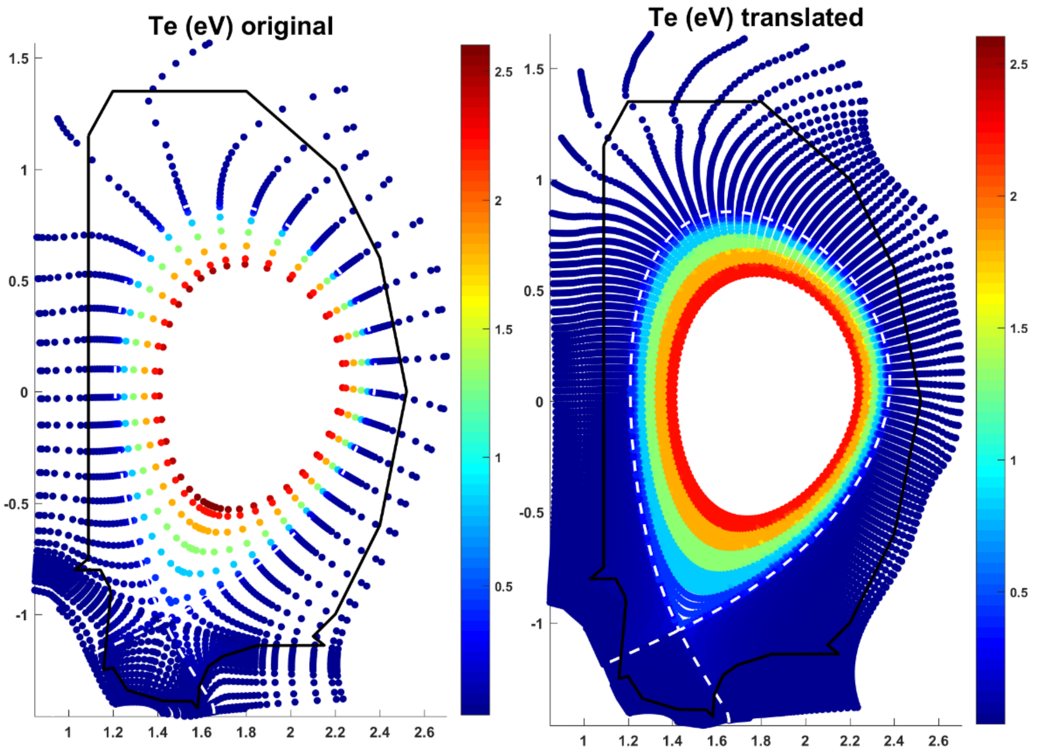

Figure 3.3.4 Left side: simulation result with the low resolution mesh. Right side: initial condition of the simulation with the high resolution mesh.

In order to verify this method, we designed an experiment to research on the impact to SOLEDGE simulation from resolution of mesh.

First step, we generate a high density grid 'case1', medium density 'case2', low density 'case3'. For simplified calculation, the configuration is single null divertor.

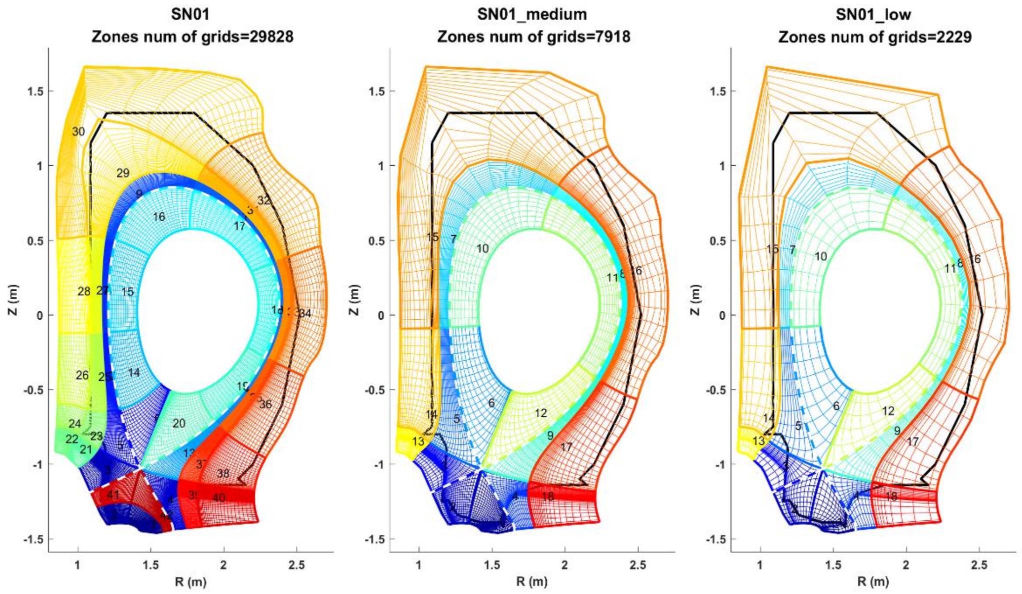

Figure 3.3.5 The mesh with high, medium and low resolution for SN configuration.

Second step, the three cases simulate from same initial condition and get the result1, result2, result3. To study the impact of grid density by comparison of these results, as shown in figure 3.3.6.

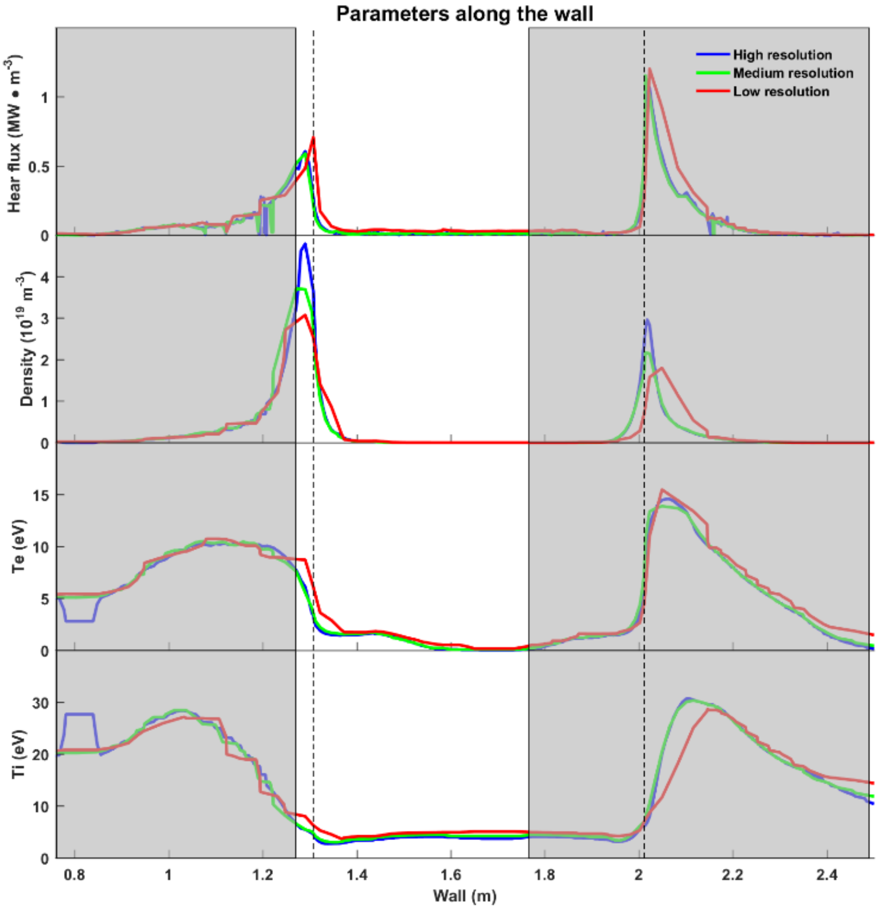

Figure 3.3.6 Comparison of the simulation results with low, medium and high resolution mesh.

Third step, translate the resut3 to the initial condition of case2 and compare the two results for case2, as shown in figure 3.3.7. These two calculation results agree very well with each other.

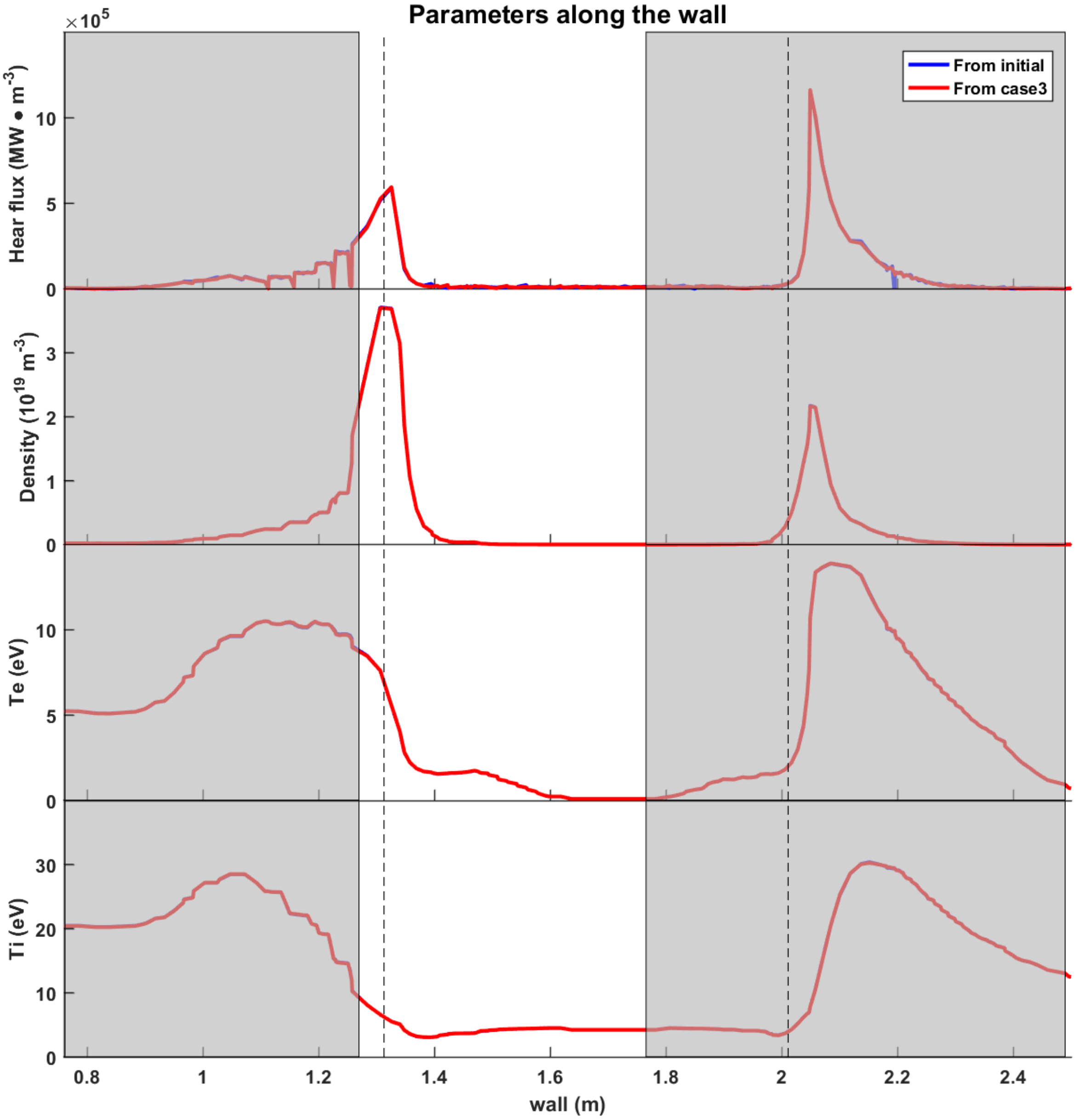

Figure 3.3.7 Comparison of two results for case2. Red line presents the simulation of which the initial condition is translated from case3's result. Blue line is the original simulation.

Fourth step, translate the resut3 to the initial condition of case1 and compare the two results for case1 to verify the validity and feasibility of the method, as shown in figure 3.3.8. These two results calculated by the simulation with high and low resolution mesh agree very well with each other. The accuracy of this method has been verified from this comparison.

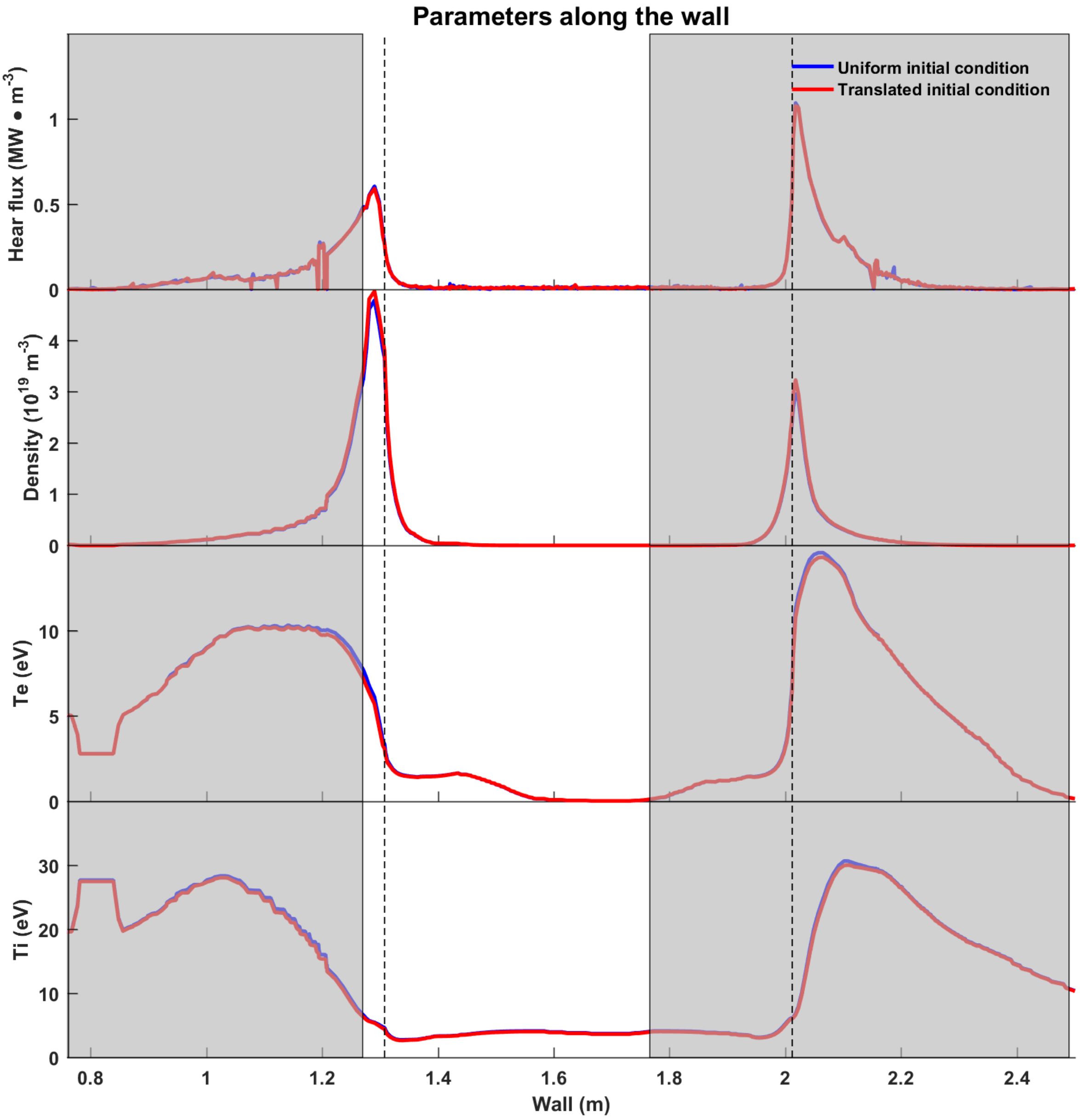

Figure 3.3.8 Comparison of two results for case1. Red line presents the simulation of which the initial condition is translated from case3's result. Blue line is the original simulation.

4. Synthetic diagnostics

This program (SYNDI) has been developed to simulate Tokamak diagnostic in 3D modeling, it can be used to prove correctness of plasma simulation code by comparing the calculated diagnosis signals and data from measured directly. SYNDI can also improve the diagnostic accuracy on the basis of simulative data. This report will introduce the bolometer module of SYNDI. For simulating the bolometer diagnostic, the classical method is generating the grid in chamber and calculate contribution to every detector from grids. For a median size Tokamak like WEST, if set the grid size as 1mm, it will have 1800*1200*15000 grids. And the bolometer diagnostic system has 16 detectors. In addition, when calculating the contribution to detector, the effect of diaphragms should be considered. Because one part of lights from the plasma will be intercepted by diaphragms. It can be equivalent to solving a geometrical problem that calculate the overlap solid angle between the detector and the corresponding diaphragm. This process include 5.2×10^{11} times geometrical calculations and would take too long time.

3.4.1 Principle of SYNDI synthetic diagnostic

In SYNDI, we use Monte-Carlo method to simulate the detector work process in opposite direction. In real physic process, the detector receives the radiation power from plasma, and the path of the ray is reversible. We assume that the detector emits a lot of rays, these rays across the diaphragm, reflect on the wall and cross plasma. The process that the rays cross plasma is equivalent to that the plasma radiate energy to detector. At last we count all the plasma that the rays pass through, the power load on the detector can be obtained. The simulated signal value expression:

$$\text{Signal} = \frac{P}{N} S_{diaph} \times a$$

P is total emission collected by detector. N is number of strays to project on the detector. S_{diaph} is diaphragm's area. a is solid angle from detector to diaphragm.

The SYNDI code require less computation and time than the classical method. The Monte-Carlo method provides to SYNDI the unique ability to simulate effectively the reflect contribution to the diagnostic, this is a great advantage over other diagnostic simulation codes that can only roughly estimate the reflect impact.

At first, we have developed a Monte-Carlo method code and a classical method code for a simple model. The model includes a detector, a diaphragm and a cube source. Suppose the detector center, diaphragm center and source on the X axis. The shape of detector and diaphragm is square and perpendicular to X axis, as shown in figure 3.4.1.

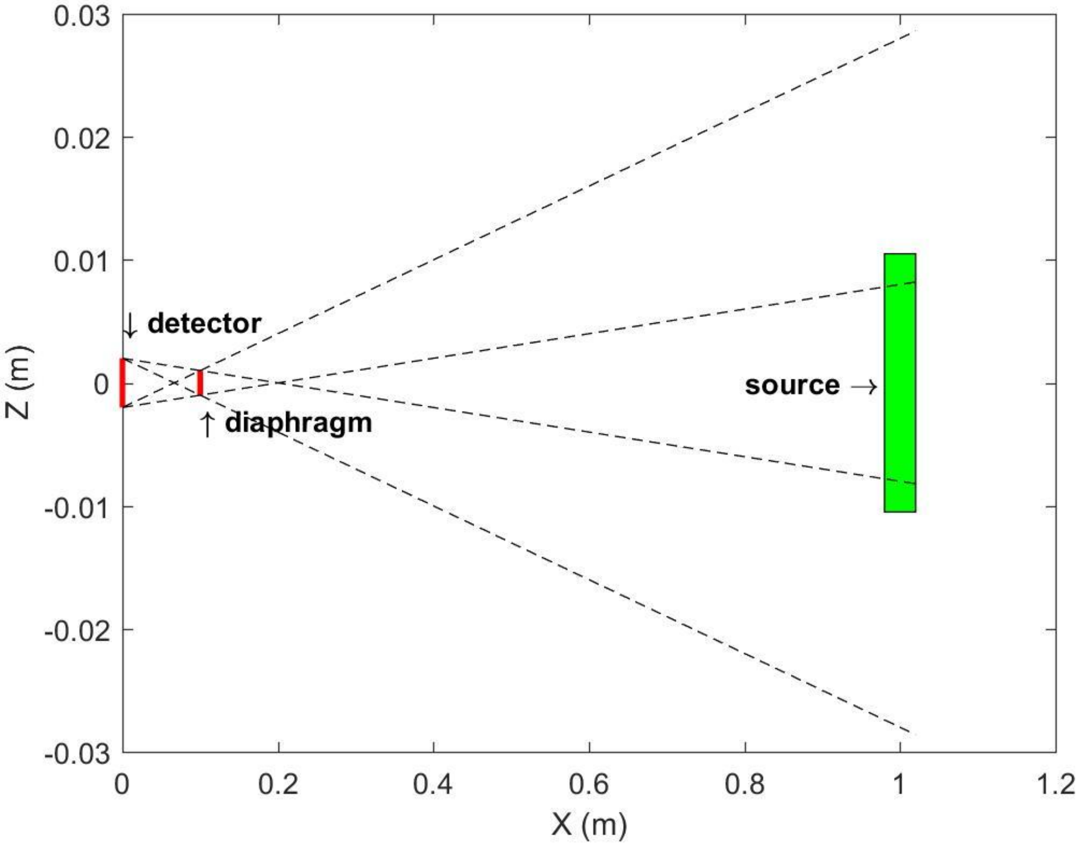

Figure 3.4.1 Simple mode for SYNDI.

To verify validity and feasibility of algorithms, we have scanned the model parameters and compare the results from two codes. Figure 3.4.2 shows the model with small and large size of detector. In figure 3.4.3, the results from two codes agree well during the process of scanning the detector size.

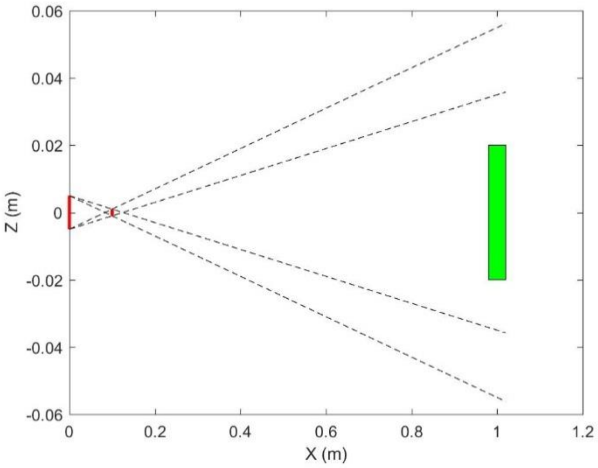

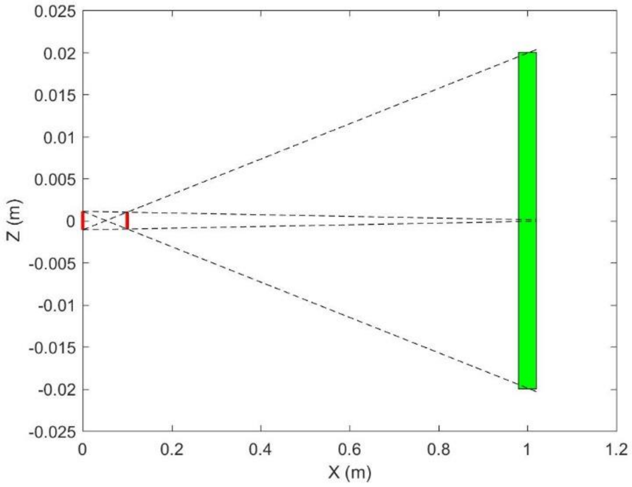

Figure 3.4.2 Simple mode for SYNDI. Top side: detector with lager size. Bottom side: detector with small size.

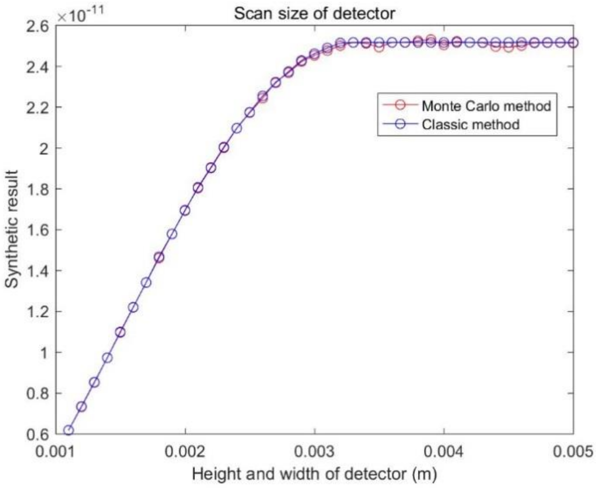

Figure 3.4.3 Comparison the results of the two codes for scanning the detector size.

Then we scan the size of source. Figure 3.4.4 shows the model with small and large size of source and figure 3.4.5 shows the results from two codes agree well during the process of scanning the source size.

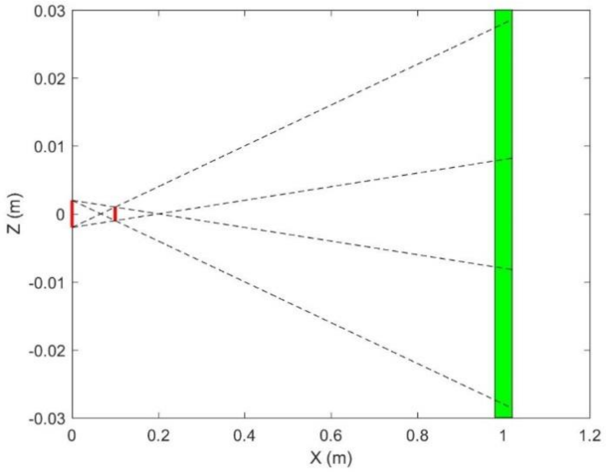

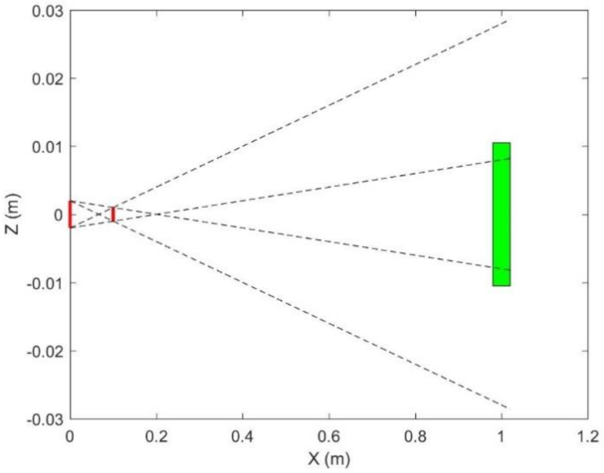

Figure 3.4.4 Simple mode for SYNDI. Top side: large source. Bottom side: small source.

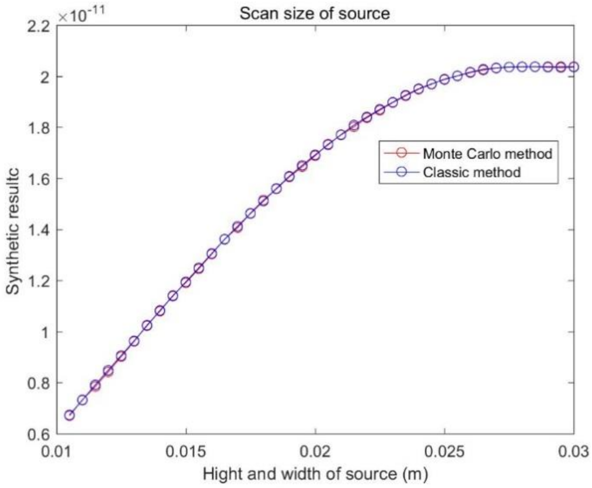

Figure 3.4.5 Comparison the results of the two codes for scanning the source size.

Scanning the position of detector on Z axis, the simple model is shown in figure 3.4.6 and the comparison of results is shown in figure 3.4.7.

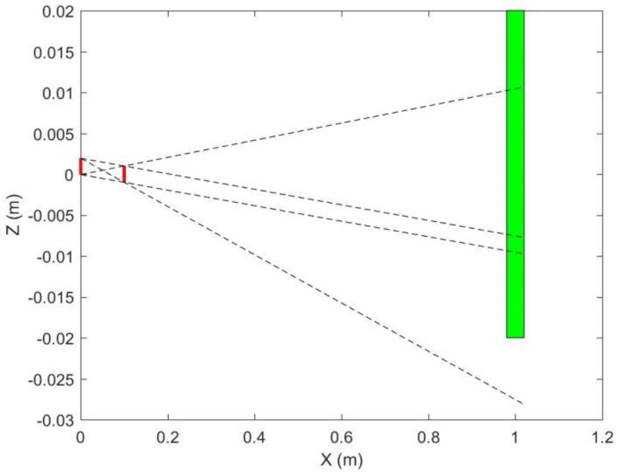

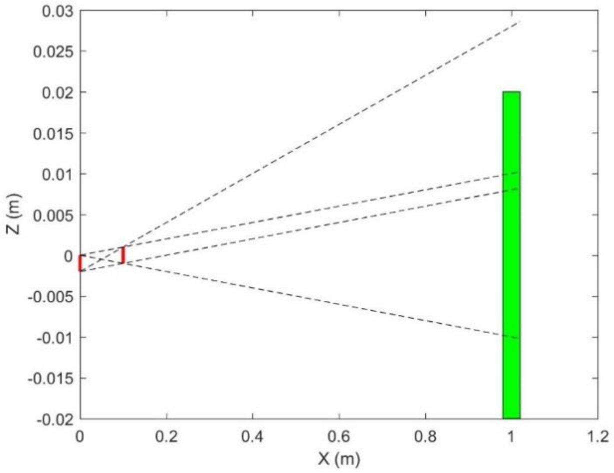

Figure 3.4.6 Simple mode for SYNDI with the scanning of detector position .

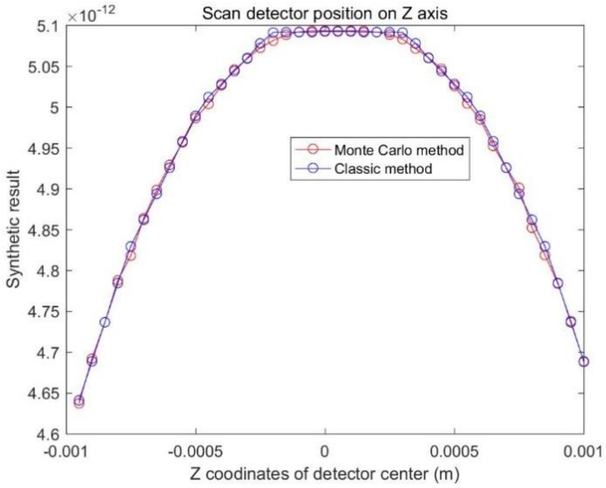

Figure 3.4.5 Comparison the results of the two codes for scanning the position of detector.

3.4.2 SINDY for tokamak

Using the SINDY in tokamak, the input data include the diagnostic system information like the detector and diaphragm's position, size, direction, shape and plasma emission profile. Figure 3.4.6 shows the track of a ray emitted from the detector. The red line represents the path in plasma, and the red star is the position of reflect.

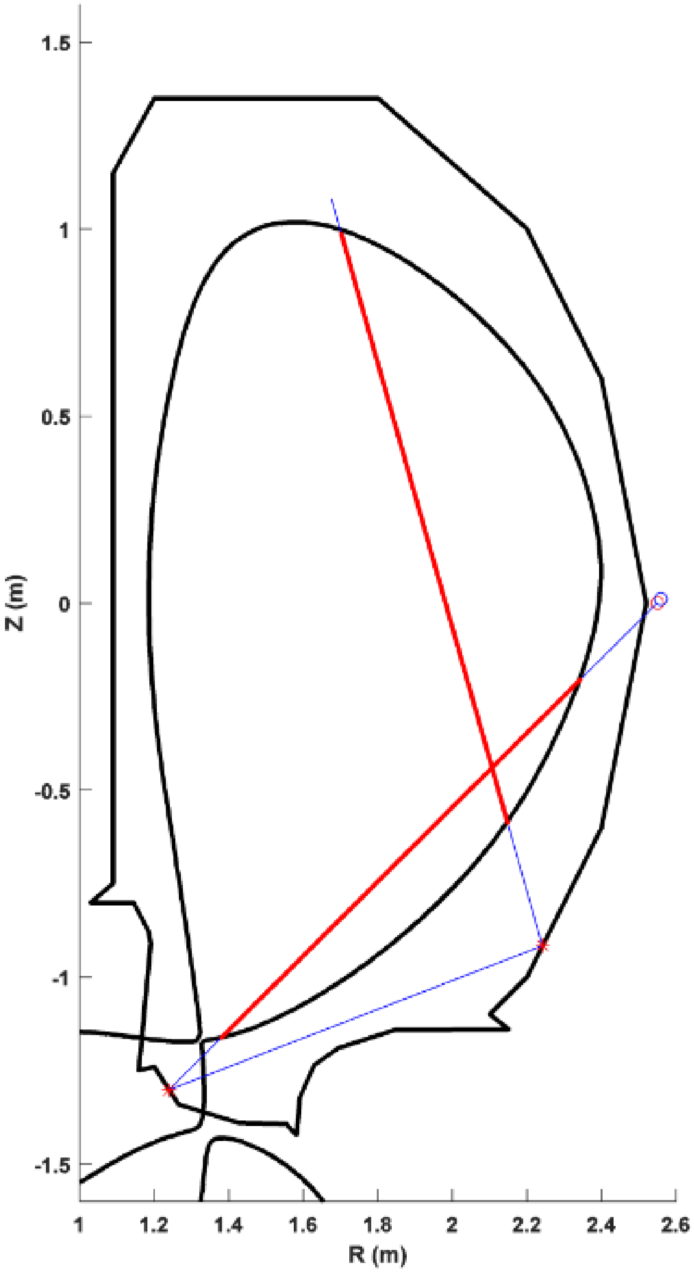

Figure 3.4.6 It shows the track of a ray emitted from the detector

To verify validity of algorithms, the comparison of the results from SINDY and the theoretical estimation has shown in figure 3.4.8. Here, we scanned the detector's position on R axis and the source is a small plasma as shown in figure 3.4.7.

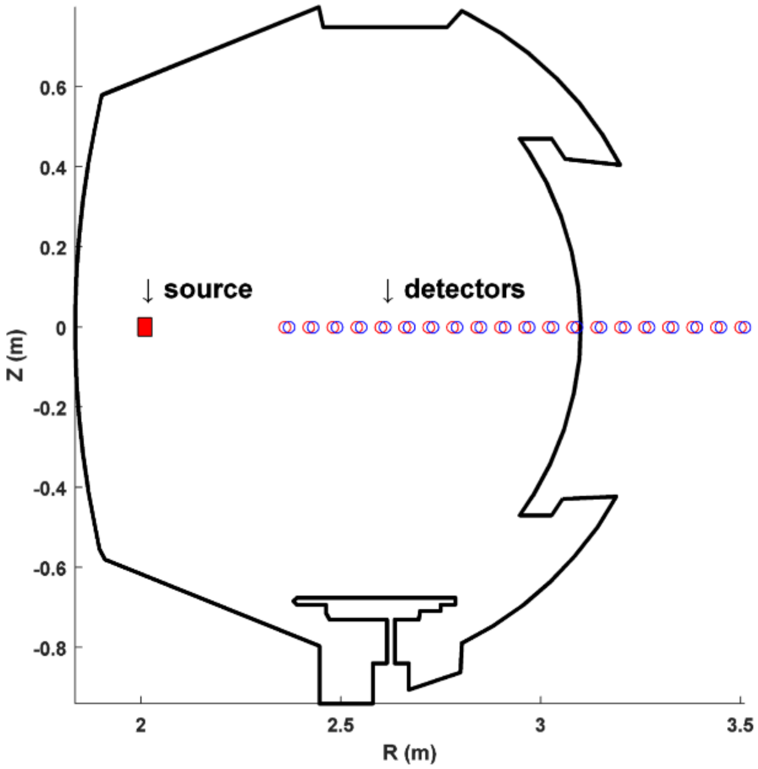

Figure 3.4.7 The simple tokamak model and the position of detector is scanned on R axis.

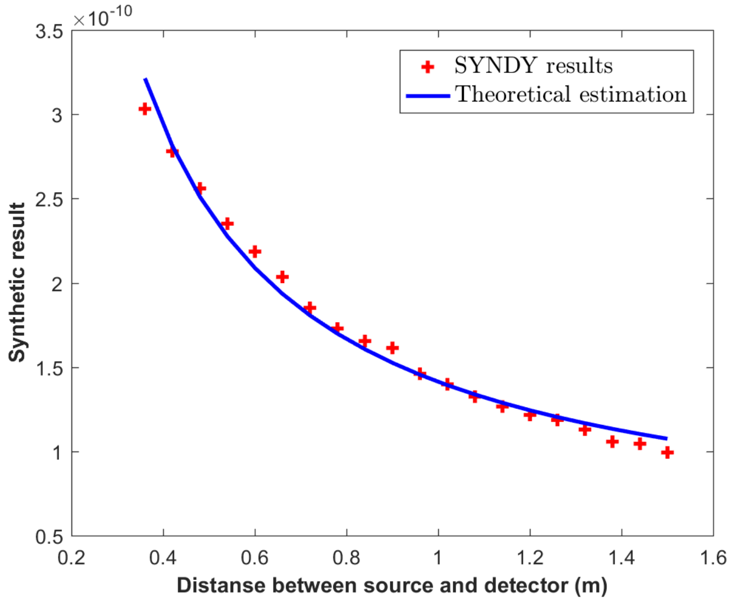

Figure 3.4.8 Comparison the results from SINDY and theoretical estimation for the simple model in figure 3.4.7.

3.4.3 Synthetic bolometer

In WEST device, the Bolometer system are plotted on figure 3.4.9. The red lines represent the central axis of the bottom channels, the black lines represent the boundary of each channel. Figure 3.4.10 shows the top side of bolometer system.

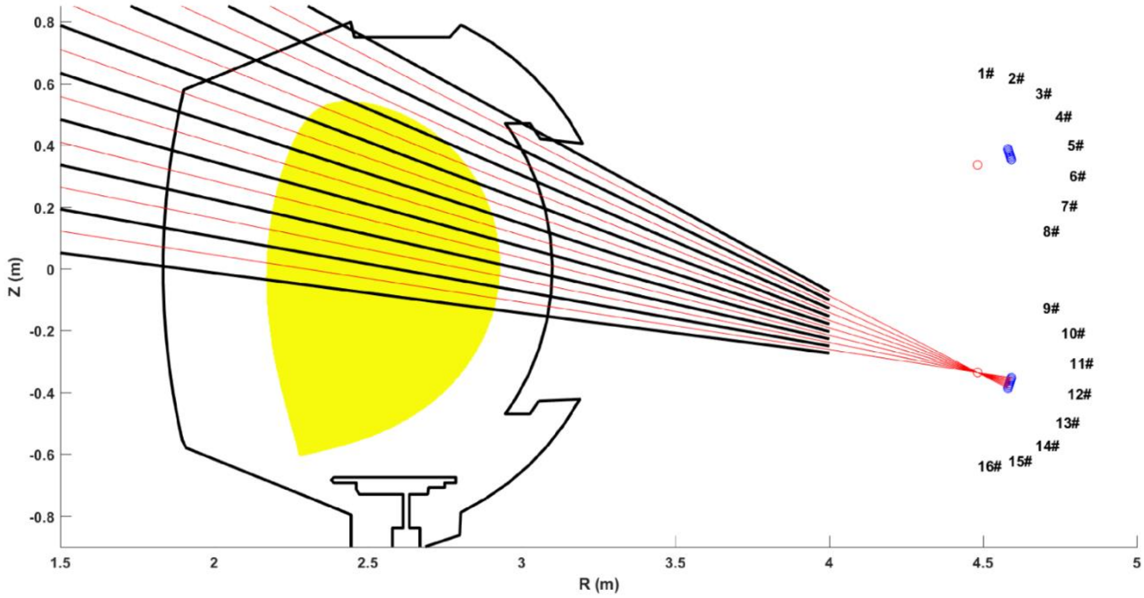

Figure 3.4.9 Bottom Bolometer system.

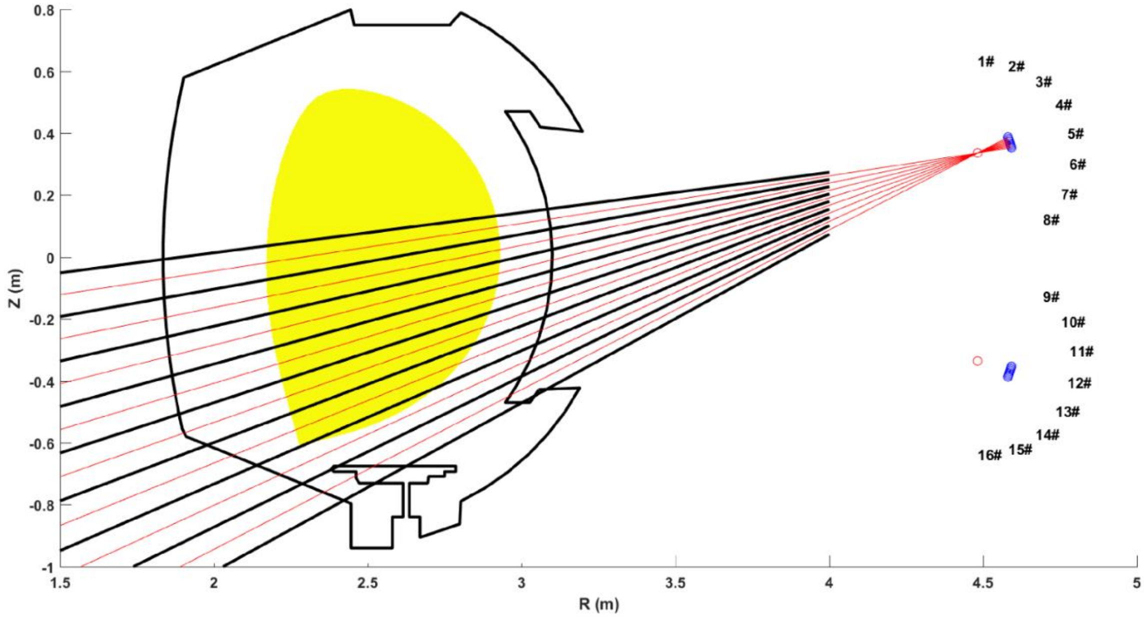

Figure 3.4.10 Top Bolometer system.

Some typical plasma radiation profiles have been used to simulate the Bolometer diagnostic as shown in figure 3.4.11-13:

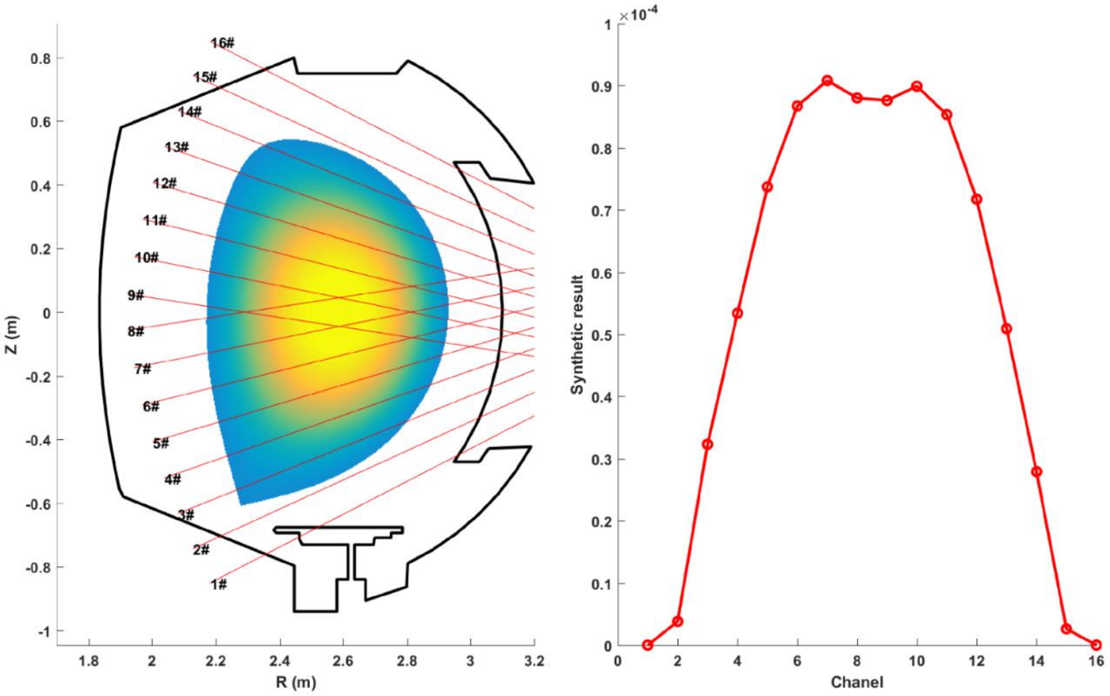

Figure 3.4.11 Typical plasma radiation profile and simulated measurements of bolometers.

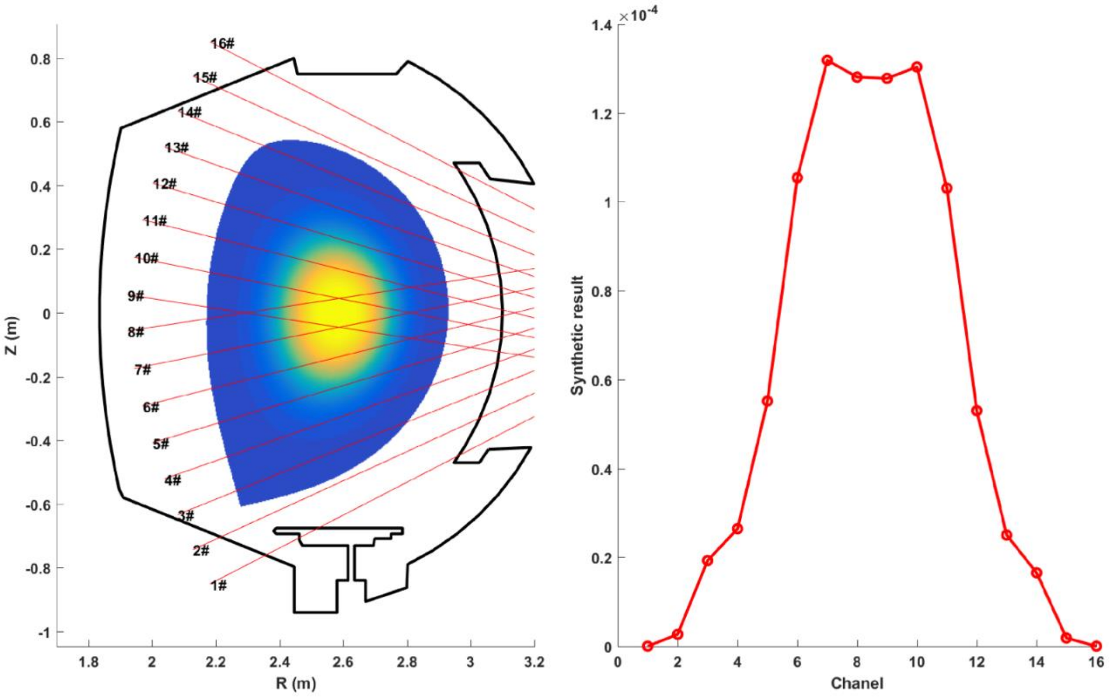

Figure 3.4.12 Typical plasma radiation profile and simulated measurements of bolometers.

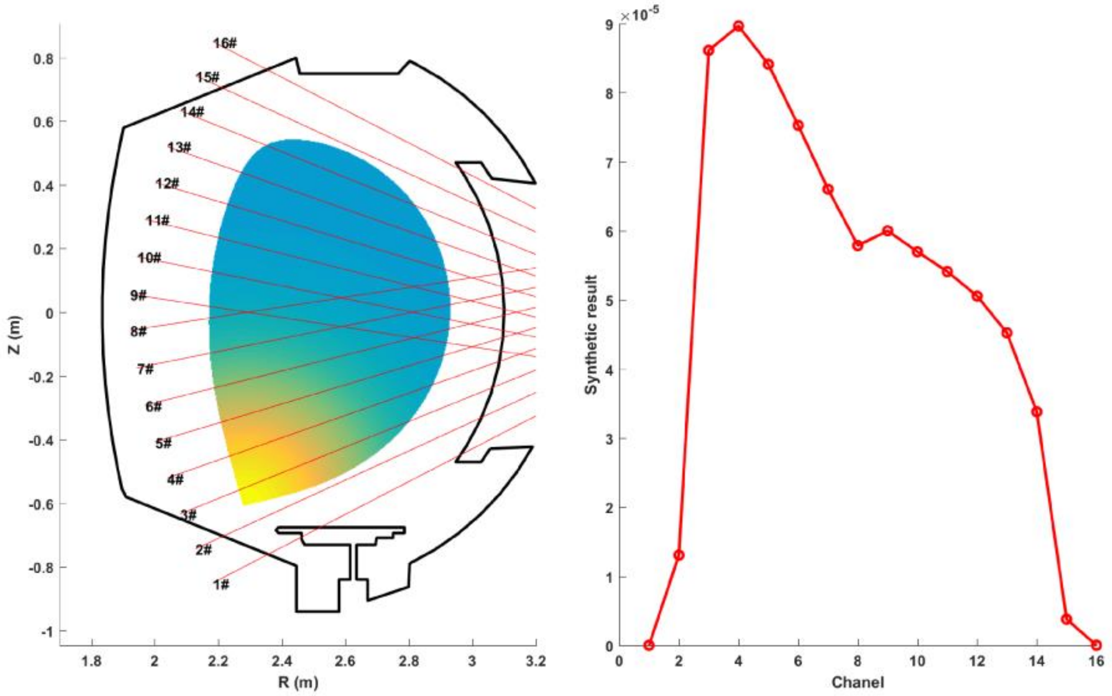

Figure 3.4.13 Typical plasma radiation profile and simulated measurements of bolometers.

Then the error of synthetic bolometer diagnostic error has been analyzed. The number of Phots we set will impact the accuracy of SANDI code simulating bolometer diagnostic. We use the 8# channel and a typical plasma radiation profile to research the influence to calculation error from the Phot number. The sight line of 8# channel pass through the plasma core area. We have scanned the Phot numbers for one detector from 200 to 1e5. For each parameter we have calculated 20 samples, the relative standard deviation and max relative error of the calculation have been plotted in figure 3.4.14. Even there are only 200 Phot in one detector, the max relative error is 0.17% and the relative standard deviation is 0.07%.

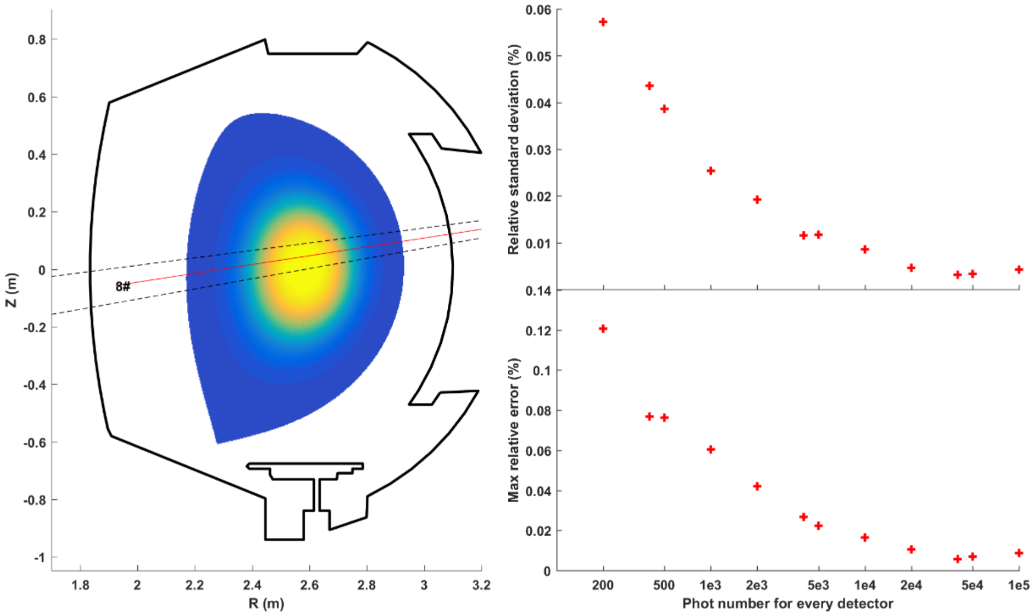

Figure 3.4.14 Error analysis of calculation error for 8# channel.

3.4.4 Visible Camera

The synthetic camera has been modeled as a 10X10 detector array and calculate light intensity signal of every detector, as shown in figure 3.4.15. Then the effect of reflection coefficient is shown in figure 3.4.16, the reflection coefficient on the wall scanned from 0 to 0.8 and the simulated camera pictures list in the right side.

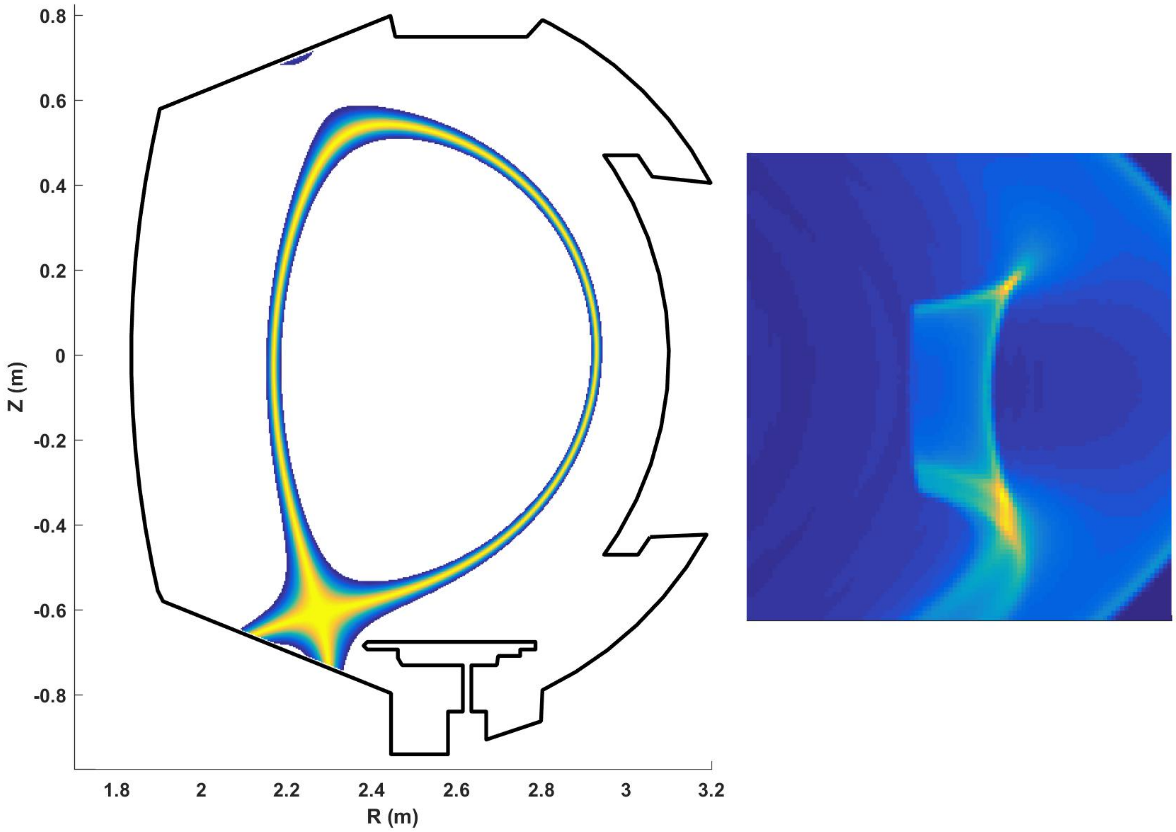

Figure 3.4.15 The synthetic camera for WEST.

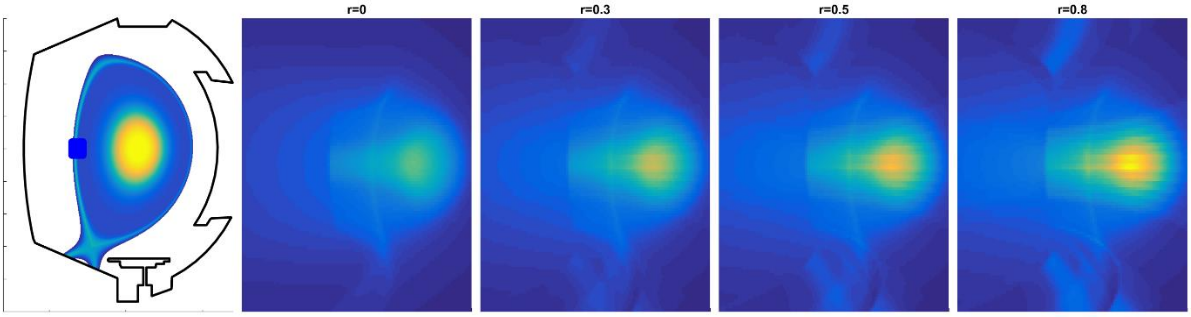

Figure 3.4.16 Scan the reflection coefficient from 0 to 0.8

Chapter IV: WEST simulations

1. Introduction to WEST

In this chapter, we consider SOLEDGE simulations for WEST experiments. The aim is twofold: on one side, we want to investigate the non-standard WEST divertor configuration on plasma transport combining results from both experiments and simulations. On the other side, the comparison between real experiments and simulations is a necessary step to have a certain level of confidence in the numerical tool before applying it to evaluate plasma transport in the divertor configurations of the HL-2M tokamak currently under construction at SWIP, analysis that will presented in chapter 5 and 6.

4.1 Introduction of WEST

In order to test the ITER divertor components under combined heat and particle loads in a tokamak environment, WEST (Tungsten Environment in Steady State Tokamak) project [1,2] transformed Tore Supra into a diverted machine with the ability to study actively cooled tungsten monoblocks under heat (10~20MW) and particles load ($10^{27}\ Dm^{-2}$) of ITER long pulse operation (above 100s). The typical operational parameters are illustrated in table 4.1.1. The additional heating and current drive system includes ion cyclotron resonance heating (ICRH) up to 9 MW, lower hybrid current drive (LHCD) with maximum 7 MW and electron cyclotron resonance heating (ECRH) with 0.6 MW.

Plasma current I_p	1 MA
Toroidal field Bt	3.7 T
Major radius R_0	2.5 m
Minor radius a	0.5 m
Elongation κ	1.3~1.8

Triangularity δ	0.5~0.6
Volume V_p	$15m^3$
Greenwald density n_{GW}(1MA)	$1.5 \times 10^{20} m^{-3}$
Heat flux from ICRH P_{ICRH}	9 MW
Heat flux from LHCD P_{LHCD}	7 MW
Heat flux from ECRH P_{ECRH}	0.6 MW
Pulse duration t_{flattop}	1000s

TABLE I. TYPICAL OPERATIONAL PARAMETERS FOR WEST

WEST has equipped low divertor with ITER-like W monoblocks and W coated upper divertor, baffle, inner bumper, as shown in figure 4.1.1. The remaining main chamber is covered by stainless steel.

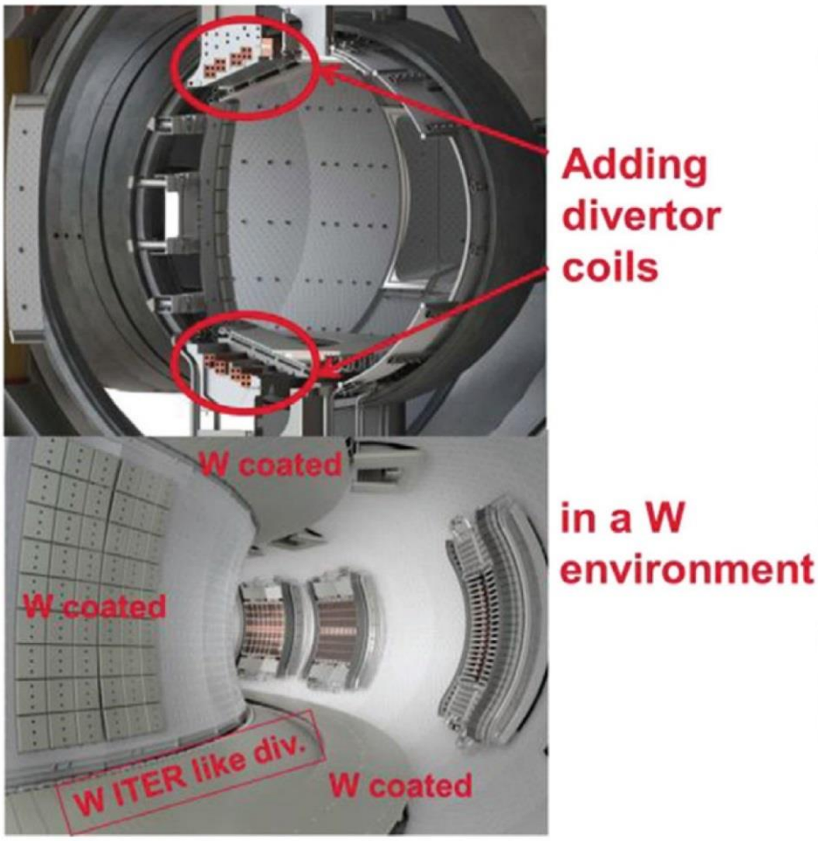

Figure 4.1.1. CAD views of WEST

WEST can provide elongated lower or upper single null, or double null configurations. The plasma magnetic surface of a standard elongated lower single null plasma is represented in figure 4.1.2.

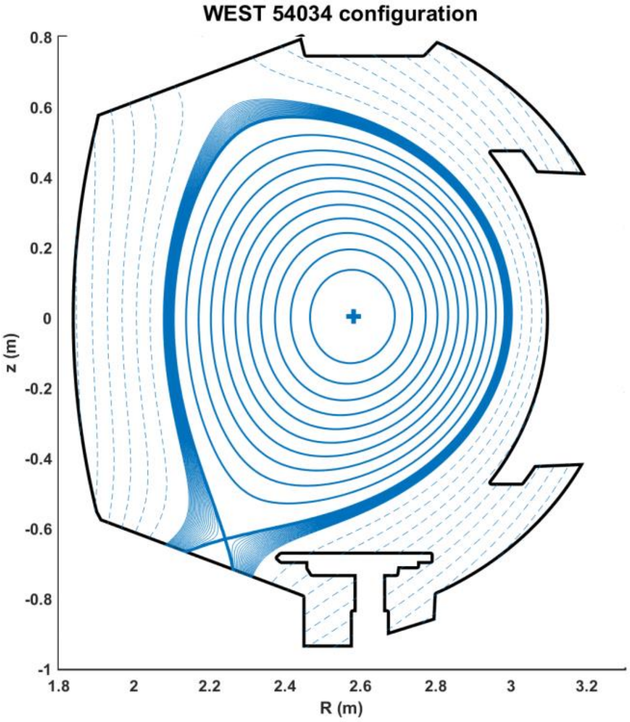

Figure 4.1.2. WEST cross section for lower single null configuration. The blue lines represent the cross section of the magnetic flux surfaces. The black line represents the wall geometry of the vacuum vessel.

The operation of WEST started in December 2016 with the first plasma. Since then three other campaigns have been performed, with the X-point configuration obtained during the C2 campaign in 2017 and with the increasing of heating power during C3 and C4 campaign, respectively in 2018 with Pinj up to 4.5 MW and 2019 with Pinj up to 7MW.

[1] Bucalossi J. et al 2014 Fusion Eng. Des. 89 907
[2] C. Bourdelle et al 2015 Nucl. Fusion 50 063017

2. Analysis of WEST experiment in Single Null divertor configuration and comparison with SOLEDGE simulations

We focus on a recent long discharge in WEST, the shot #55049 of C4 campaign obtained in September 2019. We report below the main time traces of the experiment. The LH injected power was about 4MW for more than 10s, the total radiated power around 2.5MW, central line integrated density of about $4*10^{19}m^{-2}$ and plasma current of 500 kA with a height of the X point of about 80 mm from the wall.

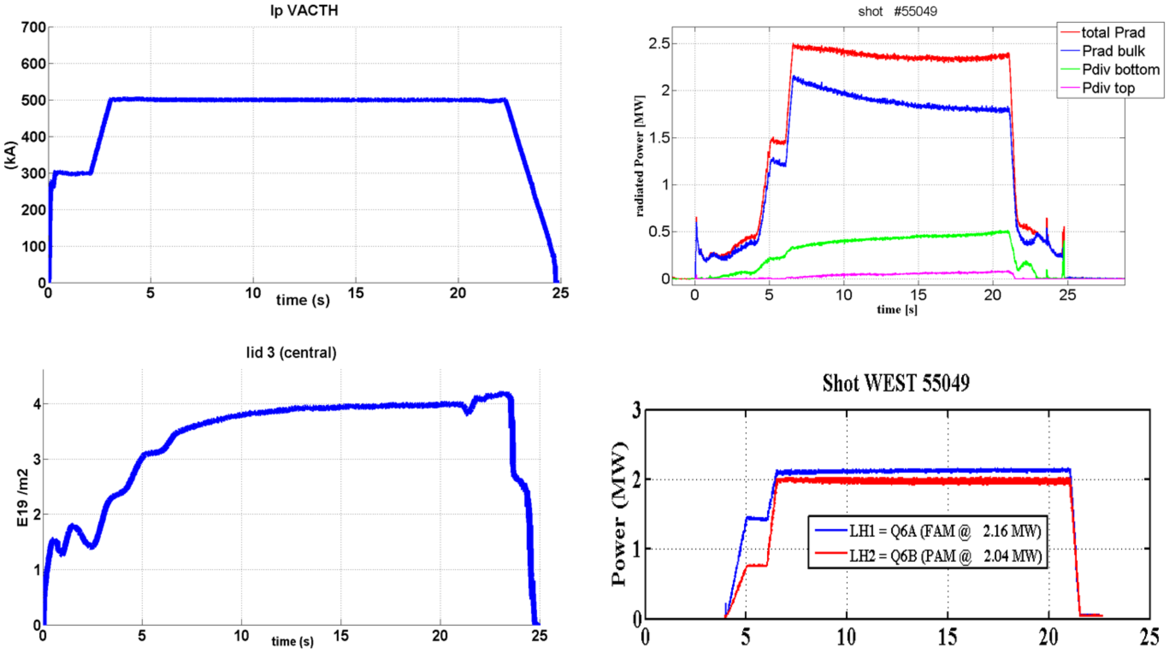

Figure 4.2.1. Time traces of basic parameters during the shot 55049.

One of the striking features of many WEST experiments is the strong amount of radiated power, both in the core and edge region. Using transport code can help on many issues like obtaining a better understanding of the divertor density regime in which the experiment is running as well as for the estimation of the amount of light impurities like Oxygen responsible for the high level of radiated power in the SOL region.

In order to proceed with SOLEDGE simulation one has first to build the mesh grid related to the specific magnetic equilibrium of the experiment, shown in Fig. 4.1.2. This operation is performed using the mesh grid generator specific to SOLEDGE2D code. Starting from the data on magnetic field and magnetic flux one can obtain the grid as shown in Figure

4.2.2. The splitting of the mesh in 34 zones is due to the fact that in SOLEDGE one uses OpenMP parallel calculation for accelerating the speed of convergence.

The meshes are aligned with the magnetic flux surfaces. For taking into account the realistic wall geometry an immersed boundary condition method called penalization has been implemented. This provides SolEdge2D the unique capability to treat the realistic first wall geometry and simulate effectively both the near than the far SOL, this is a great advantage over other well stablished edge codes like SOLPS and EDGE2D that can efficiently simulate the near SOL only. By the way thanks to these specificities of SOLEDGE code, the distribution of heat and particle fluxes all along the vessel wall are calculated, helping in recovering a consistent power balance in the analysis of experimental data.

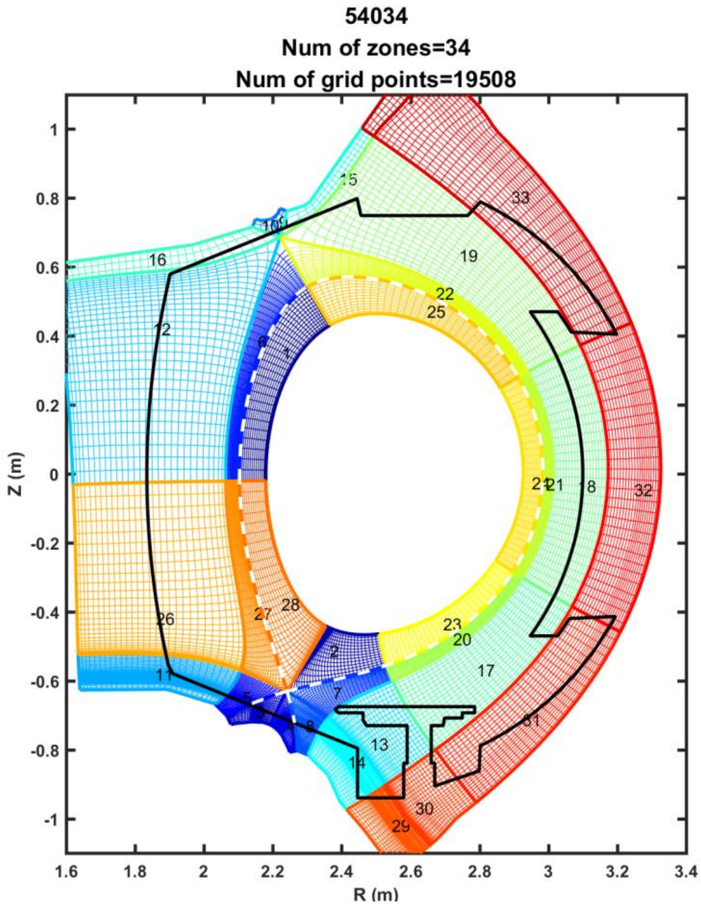

Figure 4.2.2 Grid of WEST #55049 SN configurations used for SolEdge2D code. The different color lines represent the grids of different subdomains, the black solid line under the grids represents the wall of vacuum chamber, and the white dash line represents the plasma separatrix.

The next step is to set up the input parameters for the simulation related to the specific discharge under investigation. We focus on the flattop phase and we consider measurements between 15 and 20 seconds. As we have seen the total power injected into the discharge P_{tot} is about 4MW with a radiated power in the bulk $P_{radiated,bulk}$ of about 2MW. One has also to take into account power losses P_{ripple} due to the ripple of the toroidal field, inducing bad coupling between injected power and the plasma. These power losses are difficult to estimate precisely, we consider around 10% of the total injected one. So, for the SOLEDGE simulation one can estimate a $P_{in}=P_{tot}-P_{radiated,bulk}-P_{ripple}=1.5$ MW.

The other important input parameter for the SOLEDGE simulation is the plasma density at the separatrix at the outer midplane. The measurements from

experiment come from reflectometry and reciprocating Langmuir probes and have large error bars, as shown in Fig. 4.2.3. The set up chosen for this simulation consists in specifying a target density at the OMP separatrix position that is obtained dynamically in the code with feedback control loop on the gas puff injection. The position of gas puff in the simulation domain is indicated by the red arrow in Figure 4.1.2 and the red lines on the wall represent the pumping surfaces with the recycling coefficients set equal to 0.9. The recycling coefficients of the other parts of the walls is settled to 0.99. The drifts, neutral-neutral collisions and D2 molecules are not taken into account.

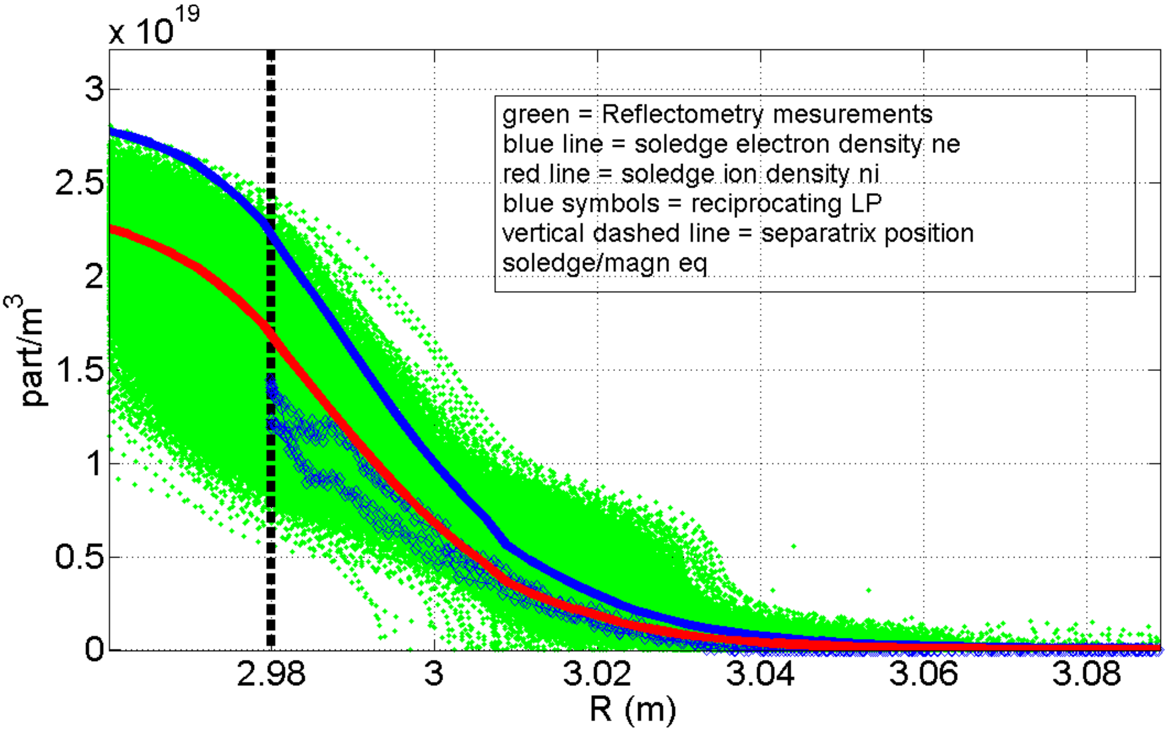

Figure 4.2.3 Outboard midplane radial profiles for electron density obtained from reflectometry measurements (green symbols) and reciprocating Langmuir probes (blue symbols). The position of the separatrix is indicated with a vertical dashed black line. The

solid lines represent results from SOLEDGE simulations. In blue the electron density and in red the Deuterium ion density.

The radial transport coefficients are settled to a typical L-mode value as specified in table 4.2.1

Parameter	**D**	$\boldsymbol{\nu}$	$\boldsymbol{\chi_e \chi_i}$	$\boldsymbol{P_{in}}$	$\boldsymbol{n_{sep}}$	$\boldsymbol{n_O}$
Value	$0.6\ m^2 S^{-1}$	$1m^2 S^{-1}$	$1m^2 S^{-1}$	2MW	1.9×10^{19}	1%

Table 4.2.1 Simulation parameters for SolEdge2D–EIRENE simulation. D is cross-field mass diffusivity perpendicular to the flux surface, $\boldsymbol{\nu}$ is momentum diffusivity, $\boldsymbol{\chi_e \chi_i}$ is heat flux diffusivity for electrons and ions, P_{in} is the power flux from the core at the core–edge interface, shared by ions and electrons as follows: P_{ions}=700kW, $P_{electrons}$=800kW. $n_{e,sep}$ is the electron density at separatrix, $\boldsymbol{n_{Oxygen}}$ represents the percentage of Oxygen with respect to Deuterium density injected at the core boundary.

For this simulation drifts, neutral-neutral collisions and D2 molecules have not been taken into account. The recycling coefficients of the walls is 0.99. We put the $v_{pintch} = 0$ in these simulations. Simulation setup is always time-dependent due to the explicit numerical algorithm implemented in SolEdge2D, but we analyses just the final steady state for each density value.

As an illustration, figure 4.2.3 shows density, parallel Mach number, electron and ion temperature 2D profiles for the WEST #54034 SN configuration. Simulation parameters are listed in table 4.2.1.

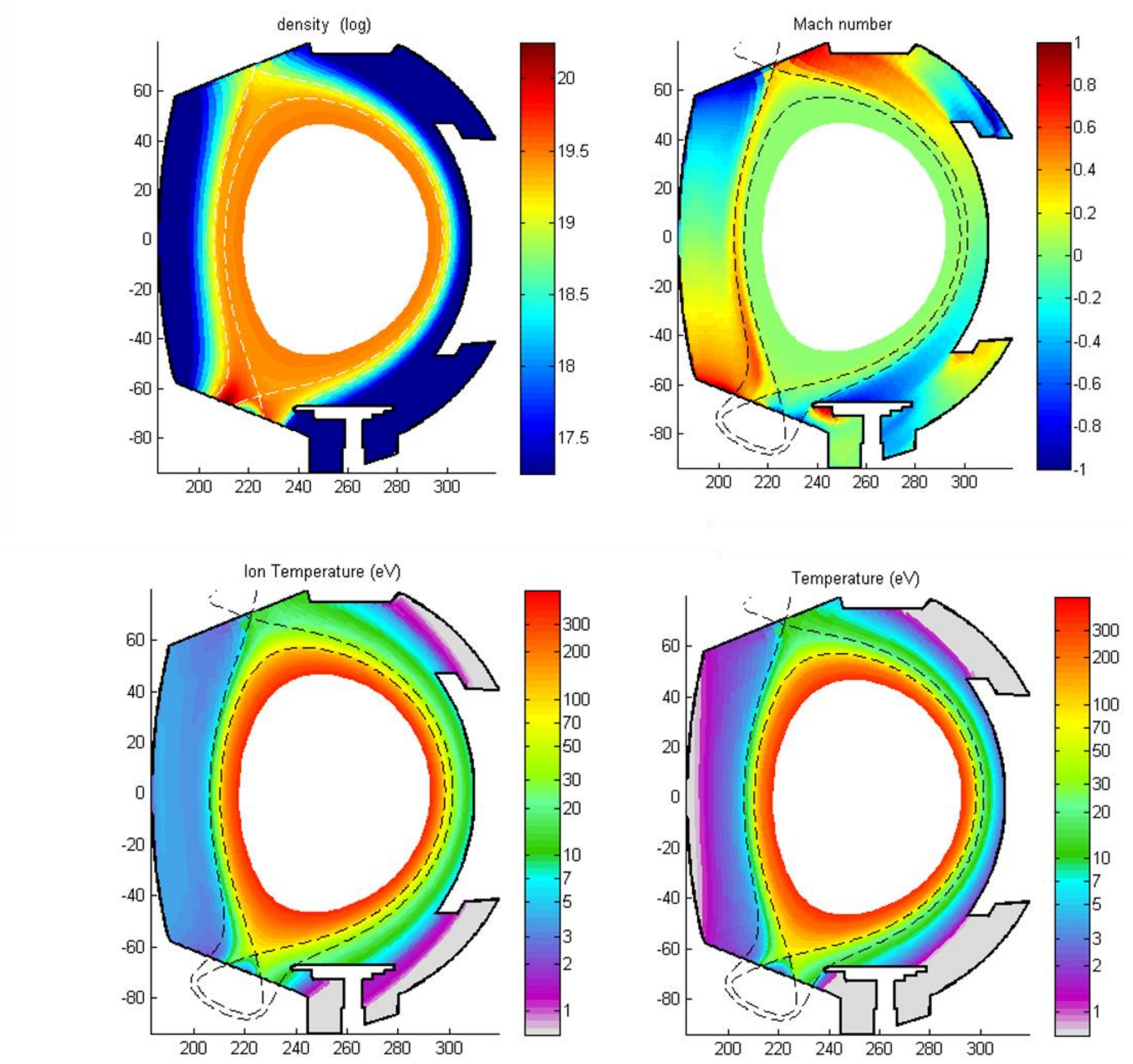

Figure 4.2.3 Example of SolEdge2D–EIRENE 2D outputs for the WEST SN plasma: density, parallel Mach number, electron and ion temperature contour plot for a deuterium plasma with 3% of injected Oxygen impurity.

As a first comparison one can look at the plasma electron temperature at the OMP obtained from the code and from reciprocating Langmuir probe, as shown in Figure 4.2.4.

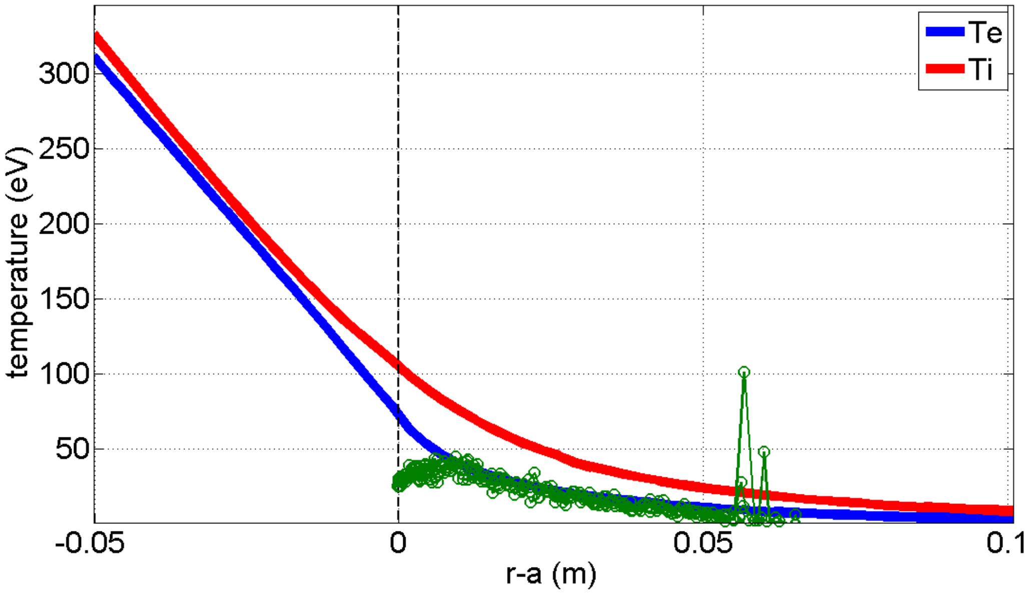

Figure 4.2.4 OMP radial profiles of electron plasma temperature obtained from SOLEDGE simulation (blue line) and from reciprocating Langmuir probe (green symbols). The Deuterium ion plasma temperature from SOLEDGE simulation is also shown (red line). The vertical black dashed line represents the separatrix position from SOLEDGE meshgrid.

It is now important to see if the divertor target profiles obtained from the SOLEDGE simulations are in agreement with Langmuir probe measurements. In Figure 4.2.5 we show this comparison at the outer strike point on parallel ion saturation current, electron density and temperature as well as parallel heat flux. The agreement is very good and indicates that the divertor is at the transition from sheath limited to high recycling regime.

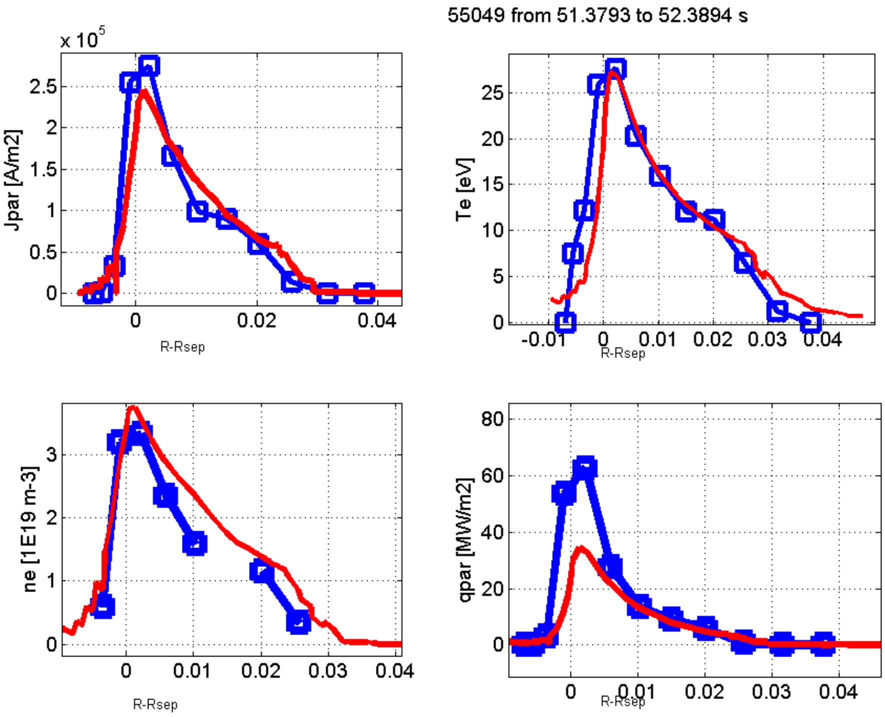

Figure 4.2.5 Ion saturation parallel current, electron temperature, electron density and parallel heat flux on outer divertor target computed with Soledge2D-Eirene (red lines) and measured by Langmuir probes (blue symbols and line).

One of the main goals of SolEdge2D– EIRENE is the calculation of the heat flux on the plasma facing components. The figure 4.2.6 shows the distribution of the total heat flux along the wall and the total load on each component. Here, the incident plasma flux, radiated flux, reflected power and recombination have been taken accounted into the total heat flux. The figure 4.2.4 clearly shows the dominant role of the lower divertor plate in heat load $P_{lower} = 1290.5kW, P_{lower}/P_t = 65.5\%$, 10.4% of the 2MW SOL power falls on the up divertor plate and 11.7% on the dome.

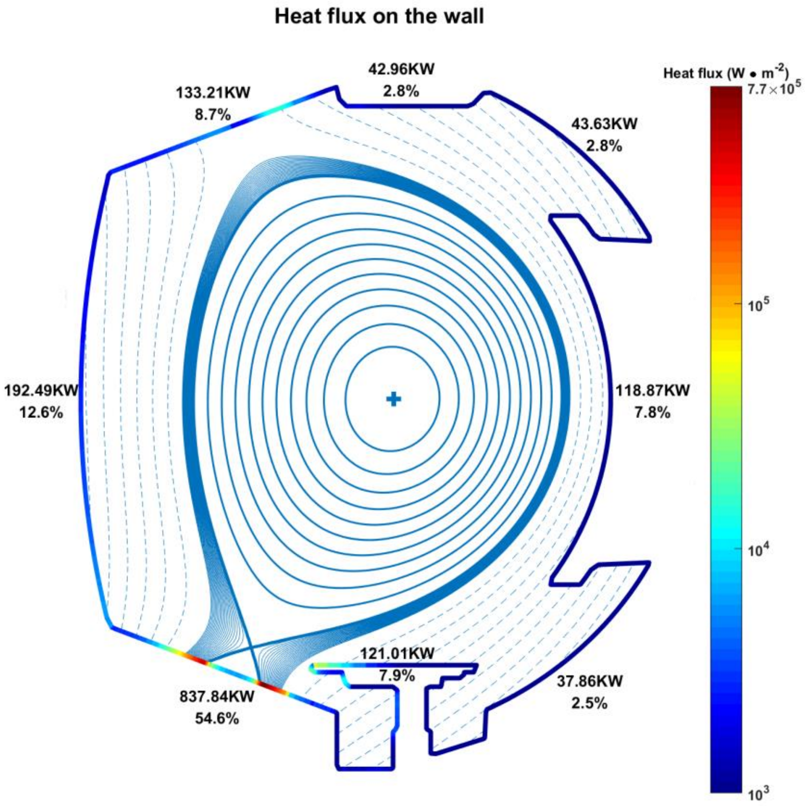

Figure 4.2.6 Heat flux distribution on the wall.

SolEdge2D-EIRENE simulations also provide the distribution of plasma parameters Te, Ti and ne along the wall, as shown in figure 4.2.7.

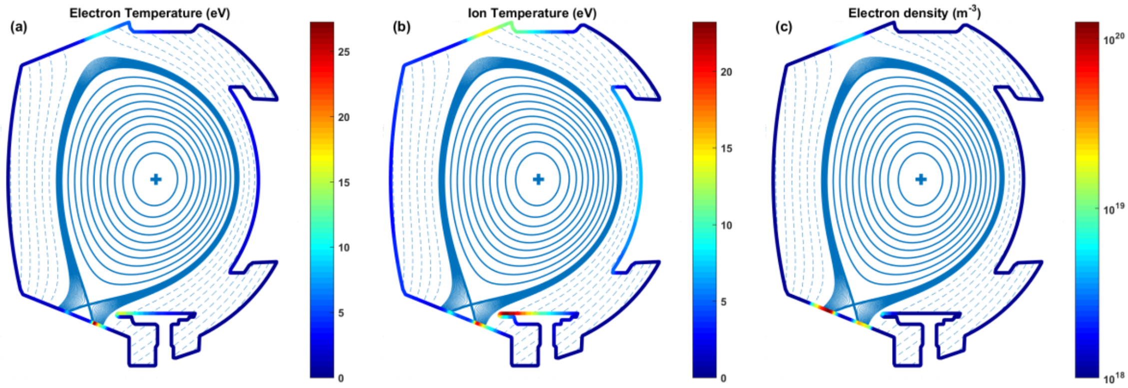

Figure 4.2.7 Example of SolEdge2D–EIRENE 2D outputs for the SN plasma: density, electron and ion temperature profile on the wall.

Considering the impurities, figure 4.2.8 shows the 2D contour plot of Oxygen density and radiation power.

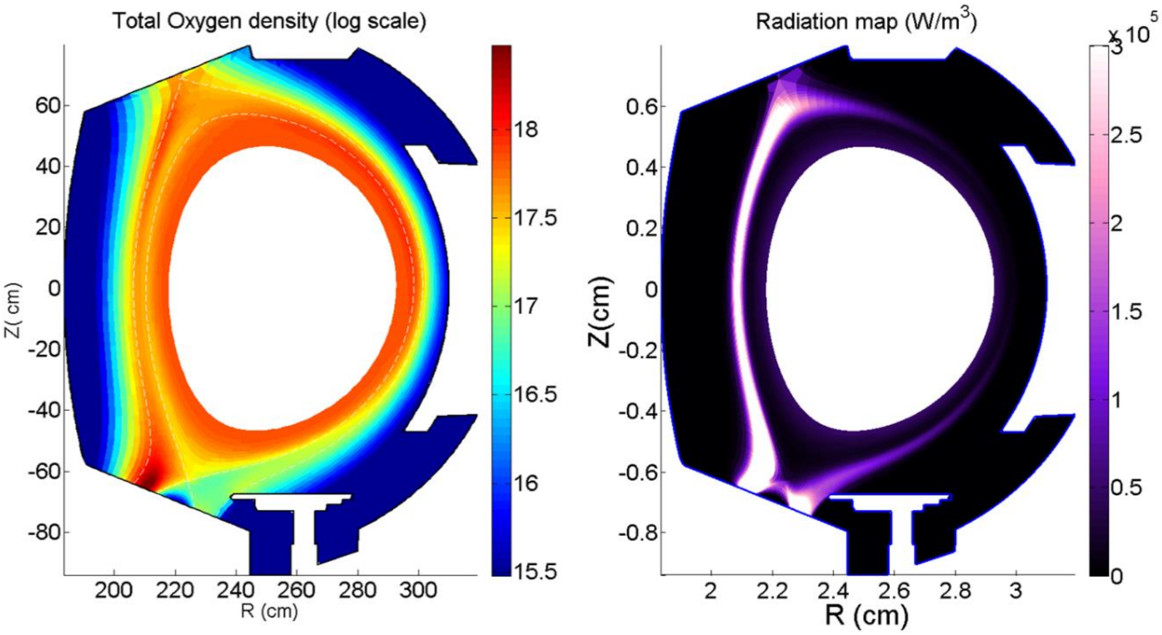

Figure 4.2.8 The 2-D profiles of Oxygen density and radiation map. The total radiated power in the simulation is about 780 kW

3. SYNDI for WEST

Using SYNDI, figure 4.3.1 shows the synthetic fast camera based on the 2-D profile of Oxygen radiation distribution calculated by SolEdge2D. Figure 4.3.2 shows the synthetic bolometer measurements for WEST. With the agreement between simulation results and diagnostic data, the correctness of the simulation is further verified.

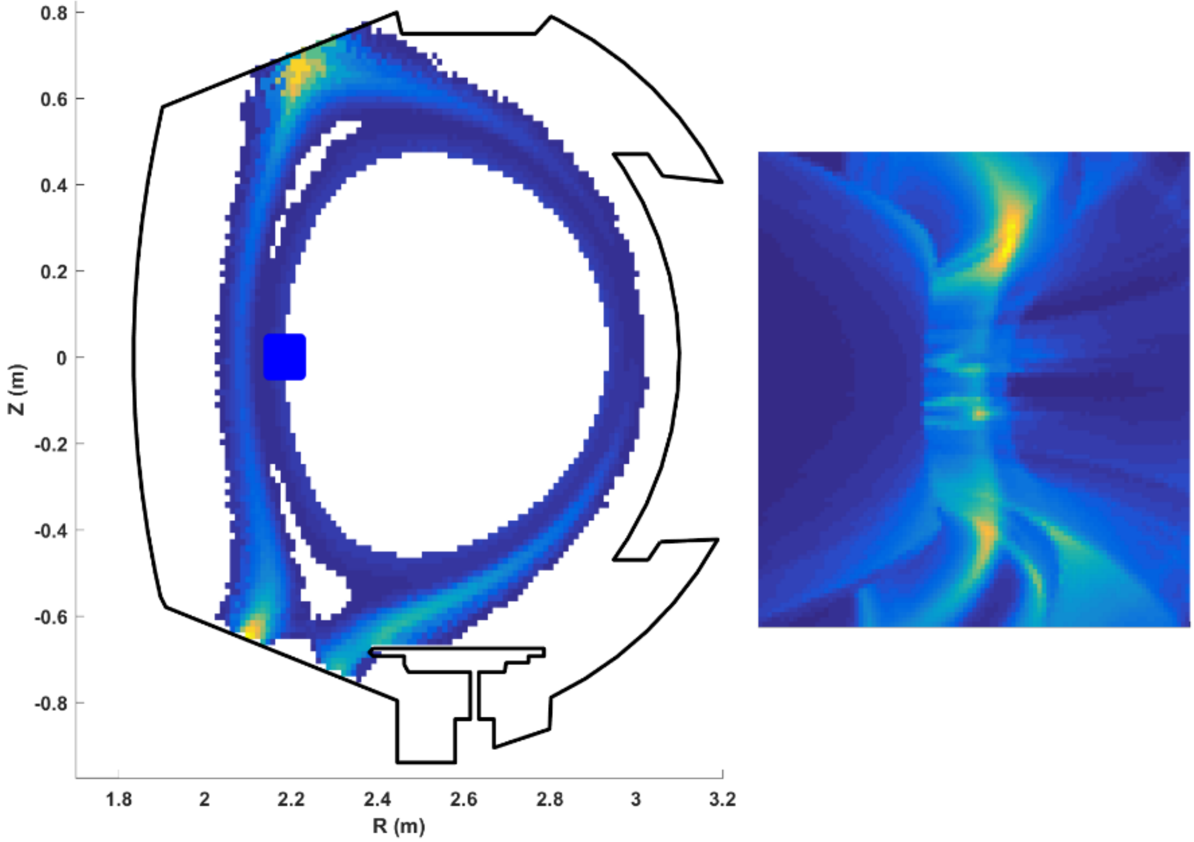

Figure 4.3.1 The left shows the radiation distribution and right side is synthetic fast camera.

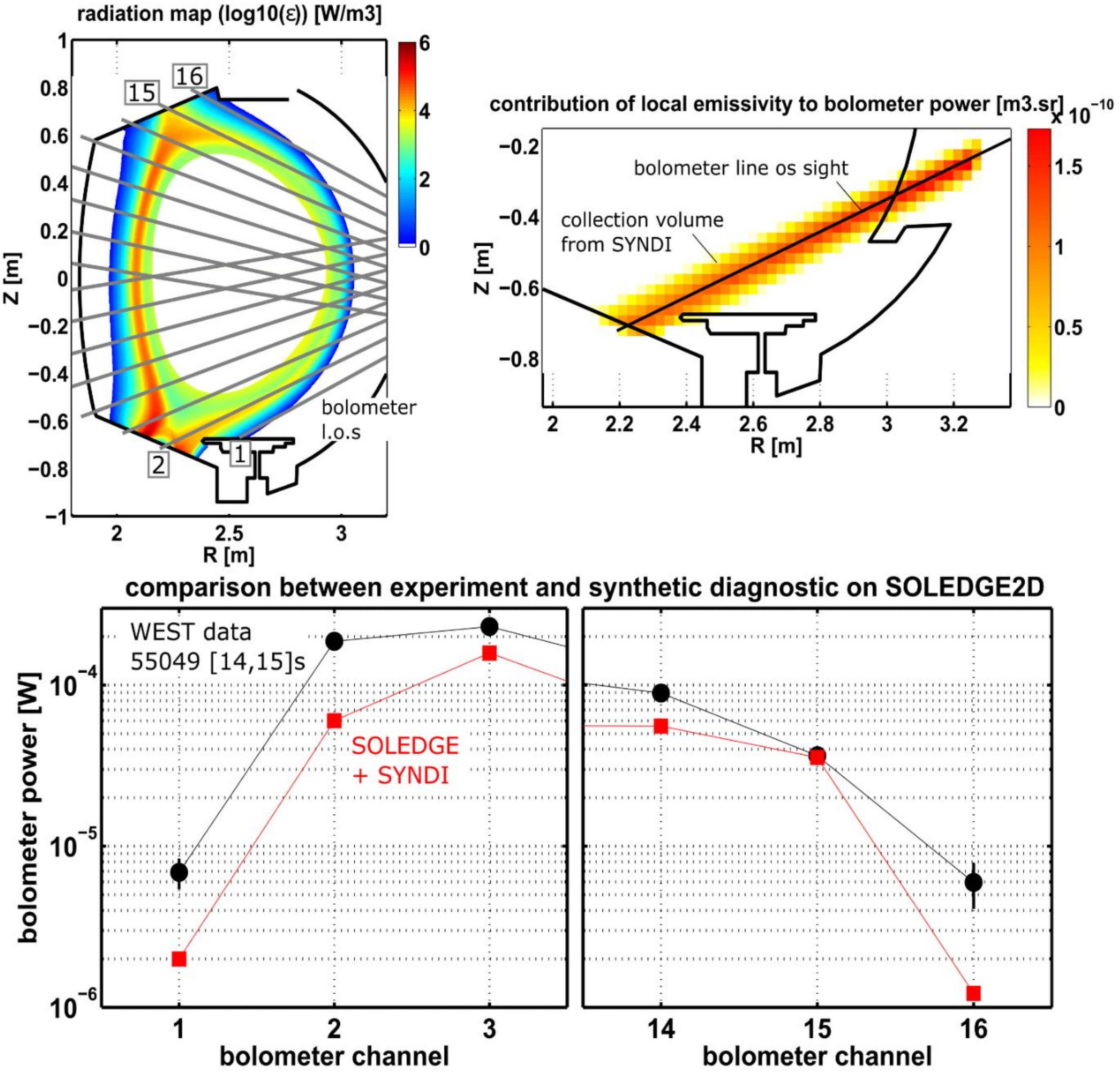

Figure 4.3.2 Synthetic bolometer for WEST.

Finally we also compare simulation results with experimental ones about radiated power. We consider the bolometer channels intercepting the edge and SOL plasma in WEST, that are channels from one to three and from 14th to 16th as shown on Figure 4.3.2 top left panel. On the bottom panels we compare the estimation from experimental data (black symbols) with the ones obtained from the application of SYNDI to radiated map from SOLEDGE simulation. One can notice that the simulation reproduces quite well the qualitative behavior and even a good quantitative comparison is obtained on the upper divertor channels.

Now that the SOLEDGE code has shown to match quite well experimental results from present machines we now step forward to investigate plasma transport in alternative divertor configurations foreseen for the HL-2M tokamak currently under construction at SWIP, China

Chapter V: HL-2M simulations

1. HL-2M device

For chapter 6, the simulations are run for the preparation of the tokamak HL-2M, currently under construction at the SWIP laboratory [1]. HL-2M aims at investigating the potential benefit of advanced divertor geometries with respect to the reduction of peak heat loads onto the divertor targets, with up to 20MW of additional power available. The typical operational parameters are as follows:

TABLE 5.1.1 TYPICAL OPERATIONAL PARAMETERS FOR HL-2M

Plasma current I_p (MA)	**1.2**
Toroidal field Bt (T)	**2.2**
Major radius R_0 (m)	**1.78**
Minor radius a (m):	**0.65**
Elongation κ	**1.8 - 2**
Triangularity δ	**> 0.5**
Volt-second ΔΦ (Vs)	**14**
Heating power (MW)	**20**

According to the overall requirements of the HL-2M installation project, the poloidal coils are composed of a central solenoid coil (CS) and a forming field coil (PF). The PF and Cs coils are disposed between the vacuum chamber (VV) and the toroidal field coil (TF), and is symmetrically arranged with respect to the midplane. The average stray magnetic field in the plasma region is less than 0.002T. The CS coil, PF coils TF coil inner edge and vacuum chamber are shown in figure 5.1.1. The PF and CS coils parameters are listed in table 5.1.2. The CS coil is mainly used to provide the required volt-seconds during the plasma discharge. The PF coils are mainly used to form and control the plasma configuration, but the CS coil also has a large influence on the plasma configuration and needs to be taken into account in equilibrium configuration designing process.

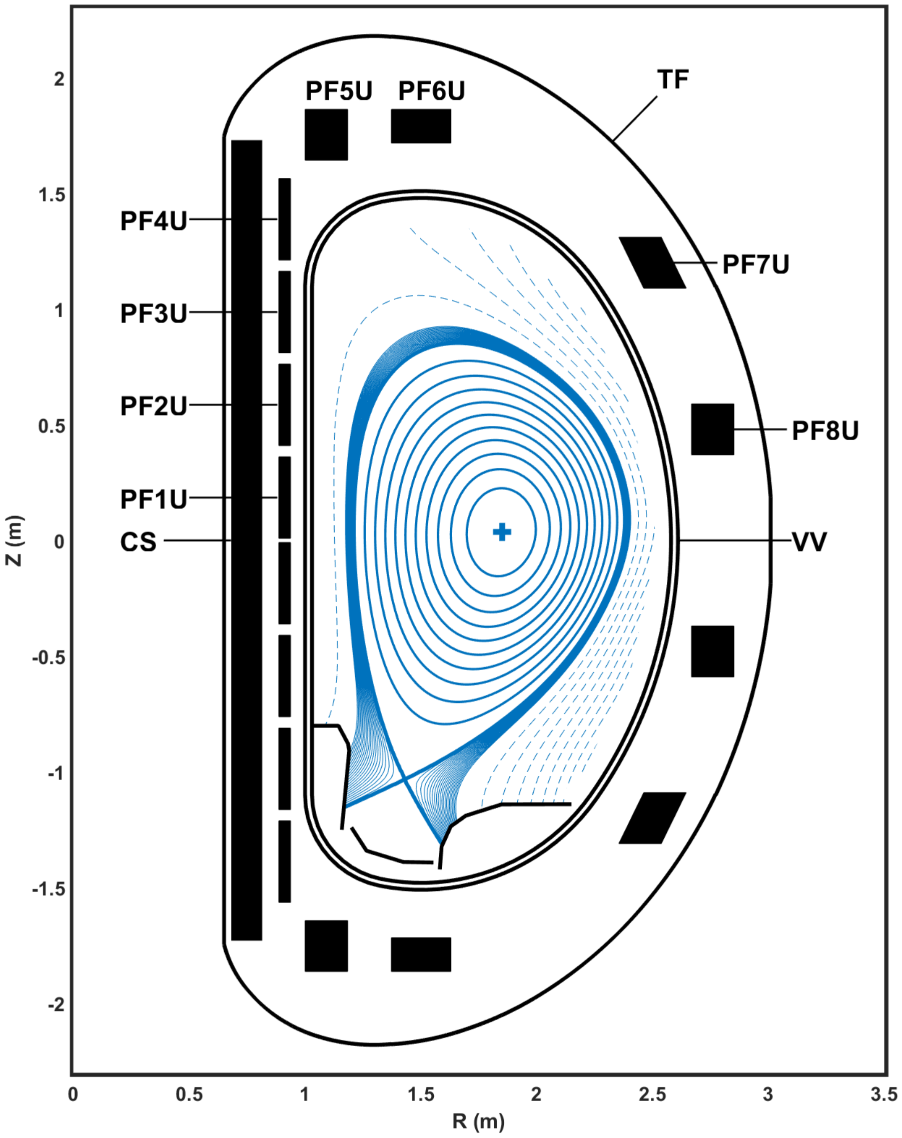

Figure 5.1.1 HL-2M device poloidal coils distribution.

Table 5.1.2 HL-2M device poloidal coils parameters.

	R(mm)	Z(mm)	w(mm)	h(mm)	Tilt angle(°)	Ncoil (Nr×Nz)	Imax (kA)
PF1	**912**	**185**	**50.4**	**352.4**	**0**	**28(2×14)**	**14.5**
PF2	**912**	**586**	**50.4**	**352.4**	**0**	**28(2×14)**	**14.5**

PF3	**912**	**987**	**50.4**	**352.4**	**0**	**28(2×14)**	**14.5**
PF4	**912**	**1388**	**50.4**	**352.4**	**0**	**28(2×14)**	**14.5**
PF5	**1092**	**1753**	**183**	**220**	**0**	**28(5×6)**	**38**
PF6	**1501**	**1790**	**257**	**146**	**0**	**27(7×4)**	**39.41**
PF7	**2500**	**1200**	**183**	**220**	**64**	**28(5×6)**	**39**
PF8	**2760**	**480**	**183**	**220**	**0**	**28(5×6)**	**35.29**
CS	**748**	**0**	**116.75**	**3442.3**	**0**	**96(2×48)**	**110**

[1] X.R. Duan et al 2017 Nucl. Fusion 57, 102013

2. Equilibrium configuration code

The task of the equilibruim configuration code is to calculate the flux distribution that satisfies the Grad-Shafranov (GS) equation, as in Equation (5.2.1, 5.2.2), based on the input plasma current, current density profile shape, and external coil current. Then the plasma configuration and parameters can be obtained from the flux distribution. Here the equilibrium configuration calculating code we used is developed on the Matlab program, based on the EFIT algorithm [2,3].

$$\Delta^{*}\psi = \frac{\partial}{\partial \mathrm{R}}\frac{1}{\mathrm{R}}\frac{\partial}{\partial \mathrm{R}}\psi + \frac{\partial^{2}}{\partial z^{2}}\psi = -\mu_{0}\mathrm{R}\mathrm{J}_{\mathrm{T}}(\mathrm{R},\psi) \quad (5.2.1)$$

$$\mathrm{J}_{\mathrm{T}}(\mathrm{R},\psi) = \mathrm{R}\frac{\mathrm{dP}}{\mathrm{d}\psi} + \frac{1}{\mu_{0}\mathrm{R}}\mathrm{F}\frac{\mathrm{dF}}{\mathrm{d}\psi} \quad (5.2.2)$$

Here J_{T} represents the plasma toroidal current density distribution, P represents the plasma pressure, and $\mathrm{F} = \mathrm{RB}_{\mathrm{T}}$ represents the polar current.

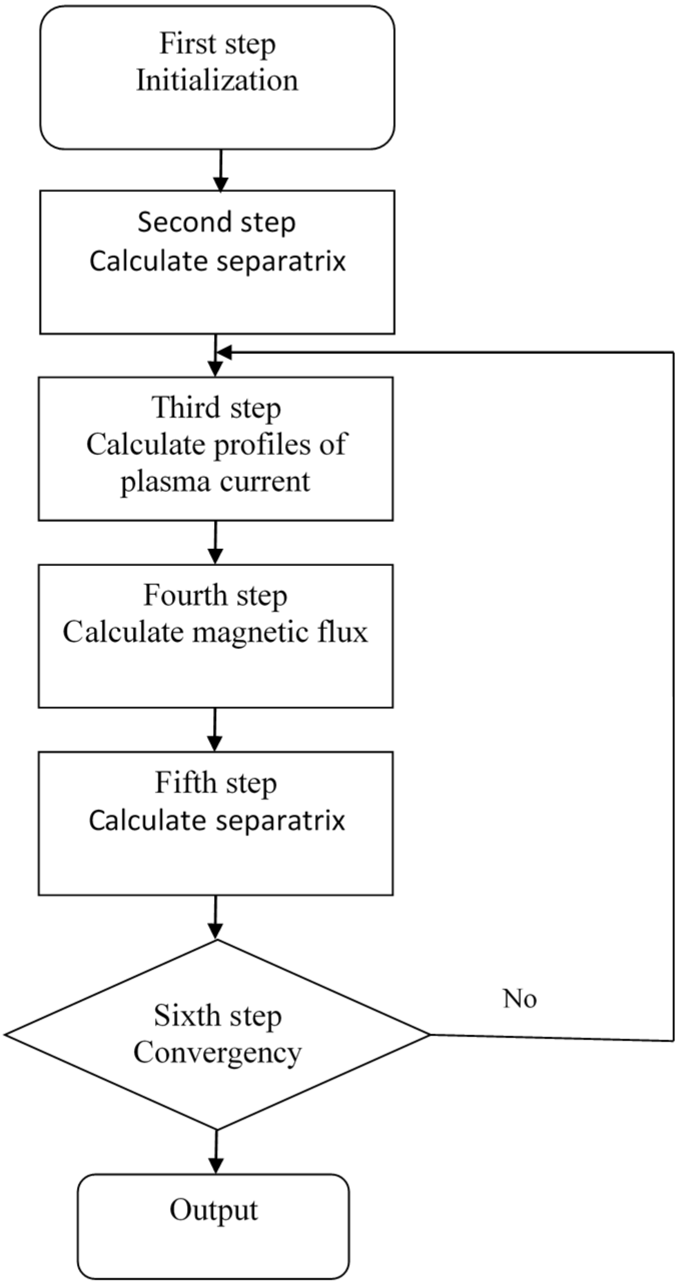

Figure 5.2.1 The process of equilibrium calculation

Figure 5.2.1 shows the flow of the EFIT equilibrium calculation. Below is a brief introduction to the solution process.

1. Initialization is mainly to input the external coil current, plasma current profile parameters; given the calculation area, divide the grid and give its parameters; give the initial plasma current density distribution. The plasma current profile parameters input here are mainly based on the selected current profile form, that is, the relationship between $J_T(R, \psi)$ and ψ. Generally, the GAQ model is used to describe the current density profile:

$$j(R,\psi) = j_0\left[\beta_{p0}\frac{R}{R_0}p(\psi) + (1-\beta_{p0})\frac{R_0}{R}f(\psi)\right] \quad (5.2.3)$$
$$p(\psi) = \left(1-{\psi_N}^{Np}\right)^{Mp}$$
$$f(\psi) = \left(1-{\psi_N}^{Nf}\right)^{Mf}$$

Where $\psi_N = (\psi - \psi_{axis})/(\psi_{bdry} - \psi_{axis})$, ψ_{axis} is the magnetic flux at the plasma magnetic axis and the maximum value of the magnetic flux in the calculation area, ψ_{bdry} is the plasma boundary flux, which is the first in the hole column configuration. The magnetic flux value of the contact limiter. R_0 is the characteristic radius of the tokamak device. There are only two free parameters J_0 and β_{p0}. J_0 is the normalized parameter expressed by the total plasma current I_P. β_{p0} is the value of the polar specific pressure. M_P, N_P, M_F, N_F are GAQ model coefficients, which affect the shape of the current profile. Usually the coefficients M_P, N_P, M_F, N_F are constant, and different normalized fluxes affect the spatial distribution of the hoop current density. When calculating the initial current distribution, it is generally possible to first give the initial normalized magnetic flux distribution, and then use the GAQ model to calculate the corresponding current distribution. There are many options for the initial flux distribution, and a parabolic model is generally used:

$$\psi_N(r,z) = \begin{cases} [((r-R_0)^2 + (z-Z_0)^2)/e^2]/a^2 & \text{inside limiter} \\ 0 & \text{outside limiter} \end{cases} \quad (5.2.4)$$

Where R_0 and Z_0 are preset magnetic flux distribution centers, e is a preset elongation ratio, and a is a preset plasma small radius.

2. While searching for plasma boundaries, we also need to find the magnetic axis and boundary flux, and then calculate the normalized flux based on $\psi_N = (\psi - \psi_{axis})/(\psi_{bdry} - \psi_{axis})$.

3. In the equilibrium calculation mode, the GAQ model is generally used to discribe the toroidal current density distribution. As described above, the normalized magnetic flux uses the latest calculation results.

4. Calculating the poloidal magnetic flux is the solution of the Grad-Shafranov equilibrium equation. There are usually two algorithms. One is the finite difference method + double cycle simplification method DCR (Double Cyclic Reduction). The DCR is a direct solution, presented by Hockney and G.Golub in 1965, Buneman gave the Fortran calculation program for the Poisson equation of the Cartesian coordinate system [4], and Buzzbee did a detailed study of the algorithm [5]. The DCR method is used in multiple equilibrium code, such as the EQUCIR 3rd Edition, which was completed in 1987 on JT-60, and the MEUDAS equilibrium Code, which was completed in JT-60U in 2002; EFIT

code written for the DIII-D device; the equilibrium code for PLT and PDX Tokamak at the Princeton Plasma Physics Laboratory by Jonson et al. Since the basic arithmetic operations of this algorithm can be vectorized, they are widely used in high performance parallel computers.

First, the finite difference method simplifies the Grad-Shafranov second-order partial differential equation into a large algebraic equation system. The coefficient matrix is symmetrically positive, the diagonal elements are dominant and a large number of 0 elements:

$$\frac{(\mathrm{\psi_{i+1,j}} - 2\mathrm{\psi_{i,j}} + \mathrm{\psi_{i-1,j}})}{(\Delta \mathrm{r})^2} + \frac{(\mathrm{\psi_{i,j+1}} - 2\mathrm{\psi_{i,j}} + \mathrm{\psi_{i,j-1}})}{(\Delta \mathrm{Z})^2} - \frac{1}{\mathrm{r_i}} \frac{(\mathrm{\psi_{i+1,j}} - \mathrm{\psi_{i-1,j}})}{2\Delta \mathrm{r}} = -\mu_0 \mathrm{r_i} \mathrm{J}_{i,j} \ (5.2.5)$$

The boundary conditions need to be calculated using the Green's function method. Setting $s = \left(\frac{\Delta r}{\Delta z}\right)^2$, the equation (5.2.5) can be simplified as:

$$\psi_{i,j-1} + \left[\frac{1}{s}\left(1 + \frac{\Delta r}{2r_i}\right)\psi_{i-1,j} - 2\left(1 + \frac{1}{s}\right)\psi_{i,j} + \frac{1}{s}\left(1 - \frac{\Delta r}{2r_i}\right)\psi_{i+1,j}\right] + \psi_{i,j+1}$$
$$= -\Delta z^2 \mu_0 r_i J_{i,j} \ (5.2.6)$$

Here, $i = 2, \cdots, n_r - 1, j = 2, \cdots, n_z - 1$. Equation 5.2.6 can be expressed as:

$$\psi_{j-1} + A\psi_j + \psi_{j+1} = 2Q_j \ \ (5.2.7)$$
$$\psi_j = (\psi_2, \psi_3, \psi_4, \cdots, \psi_{n_r-1})$$

$$A = \begin{vmatrix} -2\left(1+\frac{1}{s}\right) & \frac{1}{s}\left(1-\frac{\Delta r}{2r_2}\right) & \cdots & \cdots & \cdots & 0 \\ \frac{1}{s}\left(1+\frac{\Delta r}{2r_2}\right) & -2\left(1+\frac{1}{s}\right) & \frac{1}{s}\left(1-\frac{\Delta r}{2r_3}\right) & \cdots & \cdots & \cdots \\ 0 & \cdots & \cdots & \cdots & \cdots & \cdots \\ \cdots & \cdots & \cdots & \cdots & \cdots & 0 \\ \cdots & \cdots & \cdots & \frac{1}{s}\left(1+\frac{\Delta r}{2r_{nr-2}}\right) & -2\left(1+\frac{1}{s}\right) & \frac{1}{s}\left(1-\frac{\Delta r}{2r_{nr-2}}\right) \\ 0 & \cdots & \cdots & \cdots & \frac{1}{s}\left(1+\frac{\Delta r}{2r_{nr-1}}\right) & -2\left(1+\frac{1}{s}\right) \end{vmatrix}$$

$$Q = \begin{vmatrix} -\frac{1}{2}\Delta z^2\mu_0 r_2 J_{2,j} + \frac{1}{2s}\left(1+\frac{\Delta r}{2r_2}\right)\psi_{1,j} \\ -\frac{1}{2}\Delta z^2\mu_0 r_3 J_{3,j} \\ \vdots \\ -\frac{1}{2}\Delta z^2\mu_0 r_{nr-2} J_{nr-2,j} \\ -\frac{1}{2}\Delta z^2\mu_0 r_{nr-1} J_{nr-1,j} + \frac{1}{2s}\left(1+\frac{\Delta r}{2r_{nr-1}}\right)\psi_{nr-1,j} \end{vmatrix}$$

Starting from the center grid point, ψ_{j-2} and ψ_j are used to represent ψ_{j-1}, ψ_{j+2} and ψ_j are used to represent ψ_{j+1}. Then, an equation relate to ψ_{j-2}, ψ_j, ψ_{j+2} is obtained, repeat the above method to further obtain the equations for ψ_{j-4}, ψ_j, ψ_{j+4}. Repeating this method, the equation of the center ψ_j and the ψ value of the boundary grid point is gotten. As the ψ of the boundary grid point is known, the ψ_j value of the central grid point is obtained. Then value of other grid points can be calculated. Change the value of i and repeat the above method to get the solution of all grid points. Therefore, the mesh must be satisfied to satisfy $n_r = 2^k + 1, n_z = 2^l + 1$, k, l are natural numbers, generally 129 can meet the accuracy requirements.

The second method is the Green function method. The Green function gives the relationship between the flux function ψ and the point current source in the Grad-Shafranov equation. The relationship between the whole plasma current and the flux function ψ can be obtained by the superposition principle. Therefore, the Green function can be used to directly solve the Grad-Shafranov equation. Given the arrangement and current value of the polar field coil and inputting the previously calculated plasma current density distribution, the equilibrium equation can be directly solved to obtain the spatial distribution of the flux function.

[2] Lao L L, Ferron J R, Groebner R J, et al. Equilibrium analysis of current profiles in tokamaks[J]. Nuclear Fusion, 1990,30(6):1035.
[3] Lao L L, John H S, Stambaugh R D, et al. Reconstruction of current profile parameters and plasma shapes in tokamaks[J]. Nuclear fusion, 1985,25(11):1611.
[4] Buneman O. A compact non-iterative Poisson solver [R]. Report 294 Stanford University Institute for Plasma Research, Stanford Calf. 1969.
[5] Buzbee B L, et al. On direct methods for solving Poisson's equations [J]. SIAM Journal Numerical Analytic, 1970, 7(4):627

3. Construction of Snowflake configurations

The snowflake configurations can be provided by 16 independently powered poloidal field coils, represented in figure 5.3.1, 5.3.2. This allows an extreme flexibility both in the core plasma shape, with a large variety of shaping parameters available, as well as in divertor configurations. For the first phase of the project, divertor surfaces will be carbon materials, and stainless steel for the remaining main chamber.

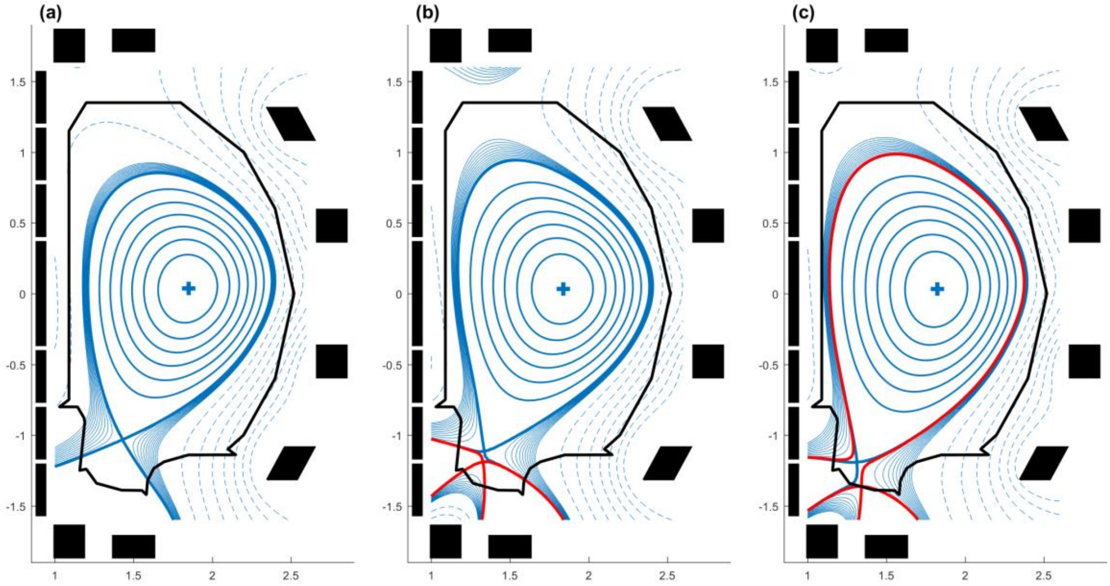

Figure 5.3.1. HL2M cross section with the 16-poloidal field coils (black boxes). (a) single null (SN), (b) snowflake plus (SF+), (c) snow flake minus configuration (SF-). The blue lines represent the cross section of the magnetic flux surfaces, while the red lines represent the flux surface corresponding to the second X-point. The black line represents the wall geometry of the vacuum vessel.

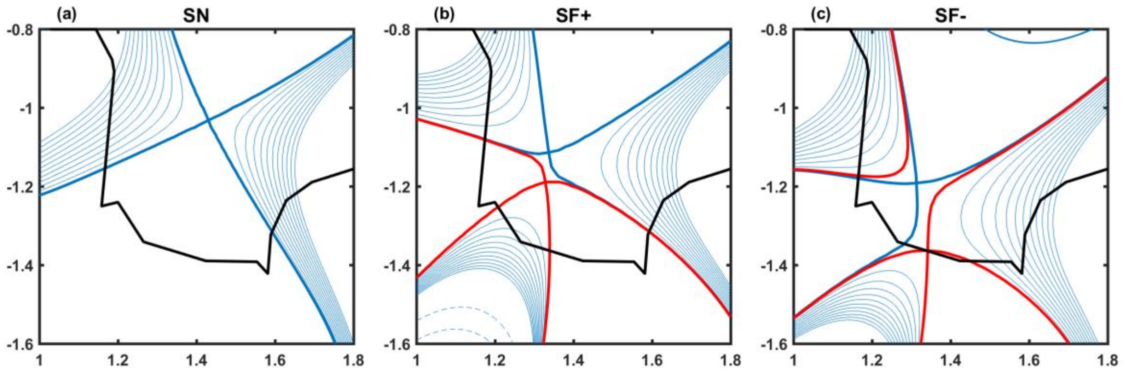

Figure 5.3.2. The plasma flux surface in divertor region for (a) single null, (b) snow flake plus, (c) snow flake minus configurations. The blue lines represent the plasma flux surface and the red lines represent the flux surface correspond to the second X-point.

The currents in poloidal coils for three configurations has shown in table 5.3.1, 5.3.2, 5.3.3. For the first phase of the project, divertor surfaces will be carbon materials, and stainless steel for the remaining main chamber.

Table 5.3.1 HL-2M device poloidal coils currents for SN.

Up coils	**I (kA)**	**Imax (kA)**	**Down coils**	**I (kA)**	**Imax (kA)**
PF1U	-6.867	**14.5**	**PF1D**	-7.867	**14.5**
PF2U	0.667	**14.5**	**PF2D**	-3.667	**14.5**
PF3U	6.667	**14.5**	**PF3D**	6.667	**14.5**
PF4U	8.000	**14.5**	**PF4D**	12.667	**14.5**
PF5U	9.000	**38**	**PF5D**	19.333	**38**
PF6U	4.000	**39.41**	**PF6D**	20.000	**39.41**
PF7U	-15.333	**39**	**PF7D**	-21.867	**39**
PF8U	-7.333	**35.29**	**PF8D**	-14.467	**35.29**

Table 5.3.2 HL-2M device poloidal coils currents for SF+.

Up coils	**I (kA)**	**Imax (kA)**	**Down coils**	**I (kA)**	**Imax (kA)**
PF1U	-13.000	**14.5**	**PF1D**	13.000	**14.5**
PF2U	-10.200	**14.5**	**PF2D**	14.000	**14.5**
PF3U	-4.500	**14.5**	**PF3D**	4.800	**14.5**
PF4U	-1.000	**14.5**	**PF4D**	15.600	**14.5**
PF5U	-9.200	**38**	**PF5D**	-25.000	**38**
PF6U	6.400	**39.41**	**PF6D**	22.000	**39.41**
PF7U	-17.600	**39**	**PF7D**	-19.000	**39**
PF8U	-8.000	**35.29**	**PF8D**	-15.800	**35.29**

Table 5.3.3 HL-2M device poloidal coils currents for SF-.

Up coils	I (kA)	Imax (kA)	Down coils	I (kA)	Imax (kA)
PF1U	-12.600	**14.5**	**PF1D**	-14.000	**14.5**
PF2U	-10.000	**14.5**	**PF2D**	-14.000	**14.5**
PF3U	-3.500	**14.5**	**PF3D**	-5.500	**14.5**
PF4U	1.000	**14.5**	**PF4D**	15.000	**14.5**
PF5U	-10.200	**38**	**PF5D**	-18.500	**38**
PF6U	7.000	**39.41**	**PF6D**	15.600	**39.41**
PF7U	-17.500	**39**	**PF7D**	-16.500	**39**
PF8U	-8.200	**35.29**	**PF8D**	-16.000	**35.29**

The sensitivity of the poloidal coil current to alternative configuration has been studied in this section. At first the disturbance has been injecting into each poloidal coil current separately, and we focus on the effect to the position of X-point. In figure 5.3.3, the disturbance $\Delta I_{coil} = \pm 1\%$ has been injected into every coil current, the red dots represent the position of the disturbed primary X-point and the green dots represent the position of the second X-point. For SN configuration, the impact is smallest, the maximum change distance of the primary X-point is 8.4mm. The SF+ configuration is most sensitivity to the poloidal coil current, the change distance 49.8mm for primary X-point and 42.3mm for second X-point. The SF- configuration is more stable than SF+, $\Delta R_{max} = 14mm$ for primary X-point and $\Delta R_{max} = 10.4mm$ for second X-point.

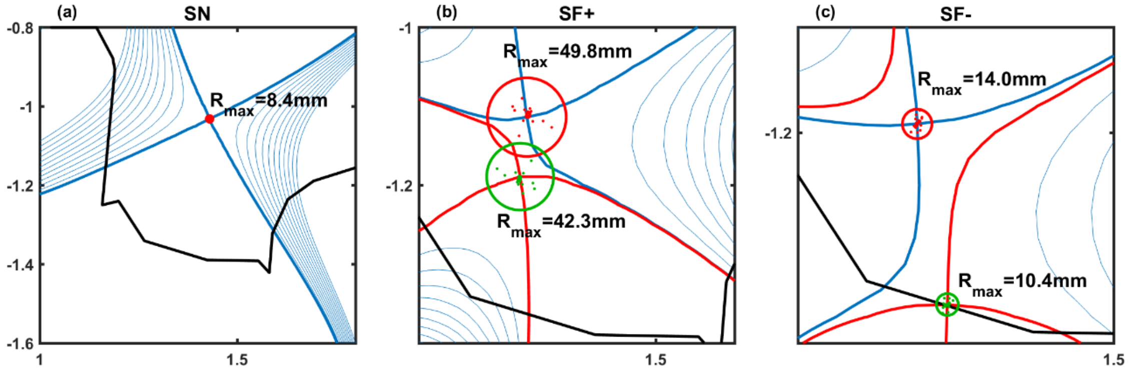

Figure 5.3.3 The position of primary X-points (red dots) and second X-points (green dots) impacted by the 1% disturbance to each poloidal coil current.

Then the disturbance $\Delta I_{coil} = random[-1\%, 1\%]$ has been injected into all poloidal coil currents, and the position of X-points are shown in figure 5.3.4. This situation is more realistic and the fluctuation of X-point position is larger. The fluctuation $\Delta R_{max} = 18.6mm$ for SN and $\Delta R_{max} = 26.7mm,\ 19mm$ for SF- configuration, but it is steal stable for these two configurations. As shown in figure 5.3.4 (b), the fluctuation of two X-points is too larger to maintain the SF+ configuration.

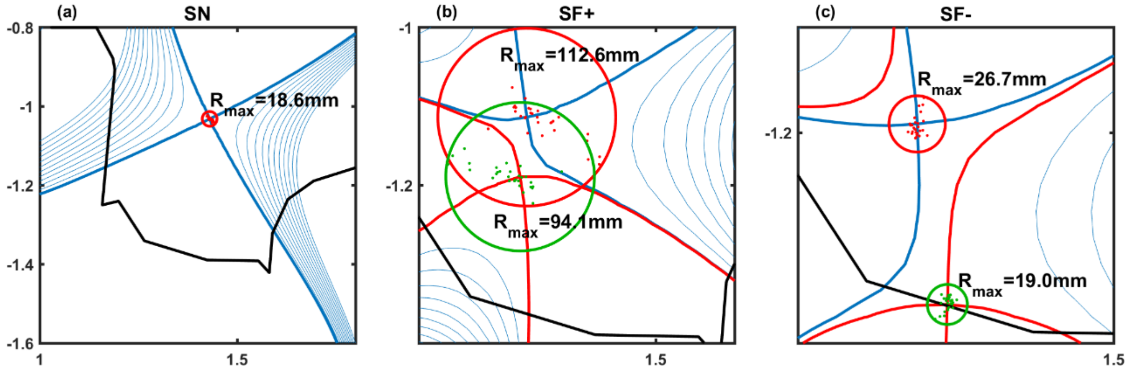

Figure 5.3.4 The position of primary X-points (red dots) and second X-points (green dots) impacted by the random disturbance to all poloidal coil current.

4. Simulation setup

We explore detachment in SN configuration using density ramps and with a simulation set up related to parameters listed in table 5.4.1. The drifts, neutral-neutral collisions and D2 molecules are not taken into account. The recycling coefficients of the walls is 0.99.

Some basic characteristics of this density ramp simulation are illustrated in figure 5.4.1 along with the magnetic geometry. In figure 5.4.1(a), the SN configuration for HL-2M has been shown, the blue arrow 1#, 2# marked the strike points for separatrix. The black solid lines represent the chamber wall, and the green line on the wall represent the passive pumping with the recycling coefficient 0.9. The drifts, neutral-neutral collisions and D2 molecules are not taken into account.

In simulation, we set the electron density on core–edge interface from $1 \times 10^{19} m^{-3}$ ramp to $8 \times 10^{19} m^{-3}$, thus increasing the separatrix density (n_{sep}), from $0.36 \times 10^{19} m^{-3}$ to $2.91 \times 10^{19} m^{-3}$, seeing in figure 5.4.1(b). The power inject into SOL region is fixed at 1.5MW, and the radiative power increases throughout the density ramp, as shown in figure 5.4.1(d).

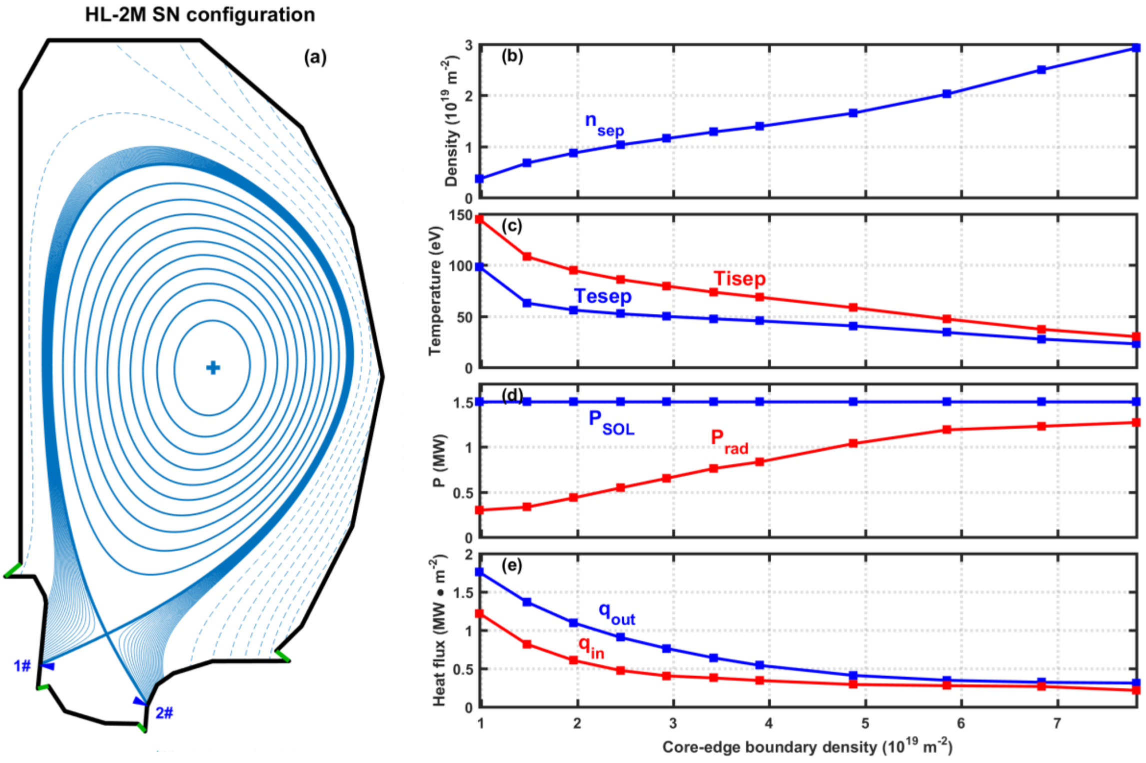

Figure 5.4.1 (a) SN magnetic equilibrium. (b) separatrix electron density on midplane, also called upstream density. (c) upstream electron temperature (blue line) and ion temperature (red line). (d) Power injected into the SOL region (blue) and radiative

power computed during the simulation (red). (e) peak value of heat flux outer target (blue line) and inner target (red line).

Parameter	**D**	$\boldsymbol{\nu}$	$\chi_e\chi_i$	$\boldsymbol{P_{in}}$	$\boldsymbol{n_{cb}}$
Value	$1\ m^2S^{-1}$	$0.6m^2S^{-1}$	$2m^2S^{-1}$	1.5MW	$1\times10^{19}-8\times10^{19}m^{-3}$

Table 5.4.1. Input parameters for the SolEdge2D–EIRENE simulations. D is the cross-field mass diffusivity perpendicular to the flux surface, $\boldsymbol{\nu}$ the momentum diffusivity, χ_e, χ_i the heat flux diffusivity for electrons and ions. P_{in} is the power flux entering the simulation domain at the core–edge interface, equally shared by ions and electrons. n_{cb} is the density at the core–edge interface.

The meshes of SN configuration for SolEdge2D-EIRENE code are plotted in figure 5.4.2. It should be noticed that the flux surfaces aligned meshes for SolEdge2D don't need to suitable to describe the first wall geometry and cover the entire vacuum chamber. This provides to SolEdge2D the unique ability to treat the realistic complex first wall geometry and simulate effectively both the near and the far SOL, this is a great advantage over other well stablished edge codes like SOLPS and EDGE2D that can efficiently simulate the near SOL only. Based on the parallel calculation of the 42 zones, it can accelerate the speed of convergence.

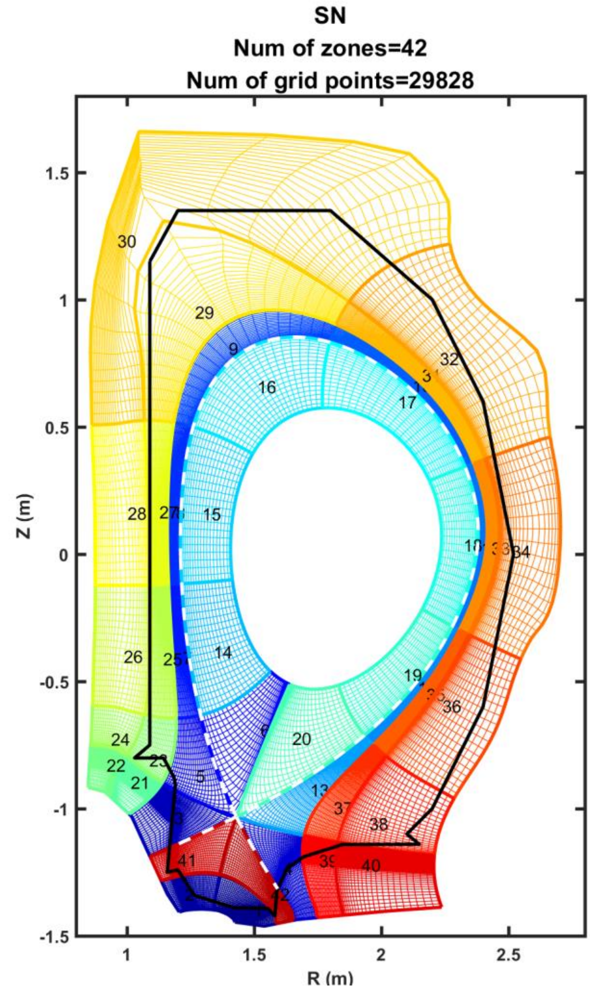

Figure 5.4.2: Grid of HL-2M SN configurations used for SolEdge2D-EIRENE code. The different color lines represent the grids of different zone, the black line represents the wall of vacuum chamber, and the white dash line represents the plasma separatrix.

As an illustration, figure 5.4.3 shows 2D contour plots of density, parallel Mach number, electron and ion temperature for the HL-2M SN configuration and the simulation parameters are listed in table 5.4.1, $n_{sep} = 0.36 \times 10^{19}\ m^{-3}$. We put the $\mathrm{v_{pintch}} = 0$ in these simulations. Simulation setup is always time-dependent due to the explicit numerical algorithm implemented in SolEdge2D, but we analyses just the final steady state for each density value.

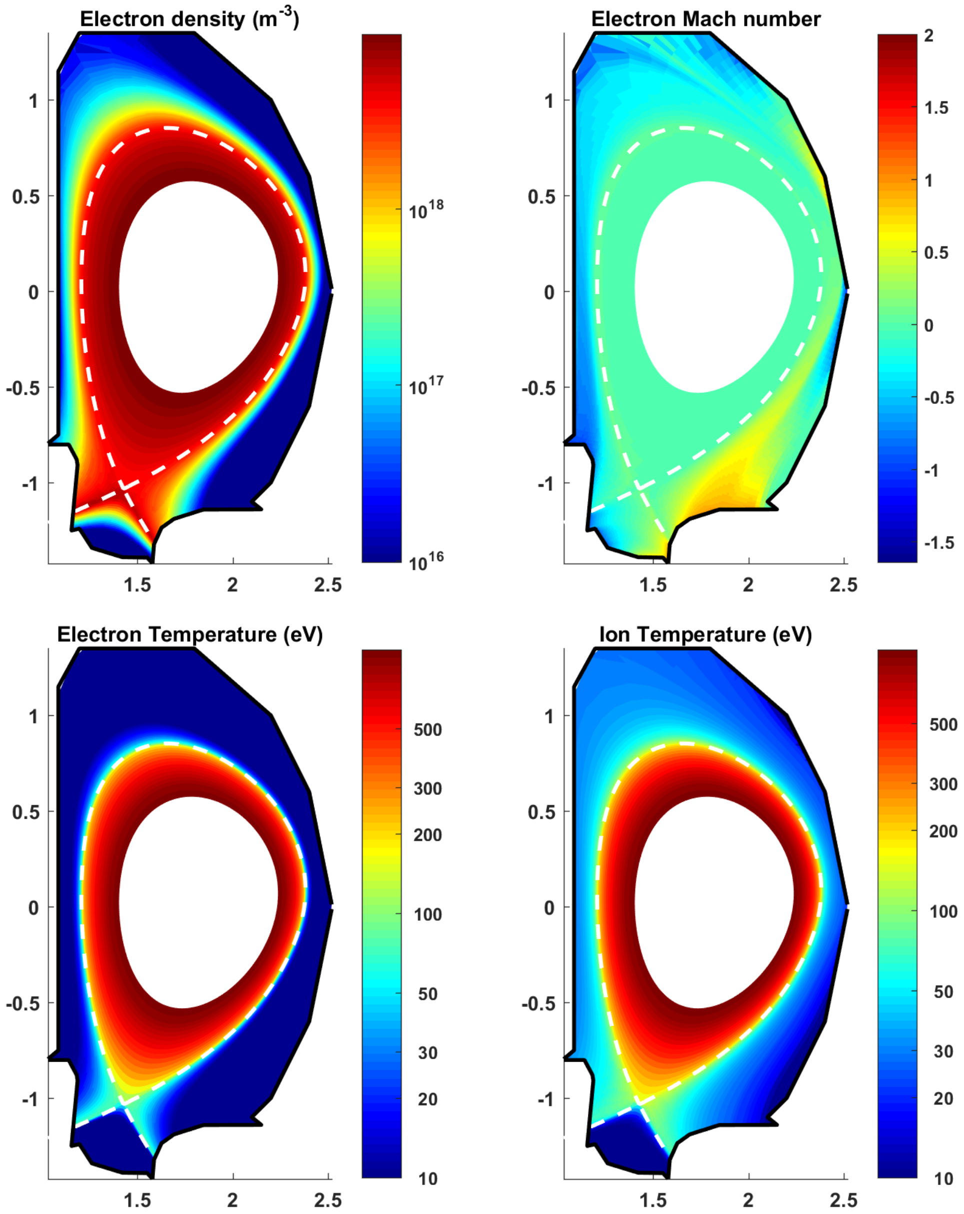

Figure 5.4.3 Example of SolEdge2D–EIRENE 2D outputs for the SN plasma: density, parallel Mach number, electron and ion temperature profile for a pure deuterium plasma with P_{in} = 1.5 MW $n_{sep} = 0.36 \times 10^{19}\ m^{-3}$. The transport parameters are shown in table 5.4.1.

The figure 5.4.4 shows the distribution of the heat flux along the wall and the total energy flux on each components. Although the constraints on the divertor are by far the most stringent, in long pulse operation heat deposition on other components, even remote from the plasma, plays an important role too. In addition, heat flux on diagnostic components such as mirrors have to be assessed.

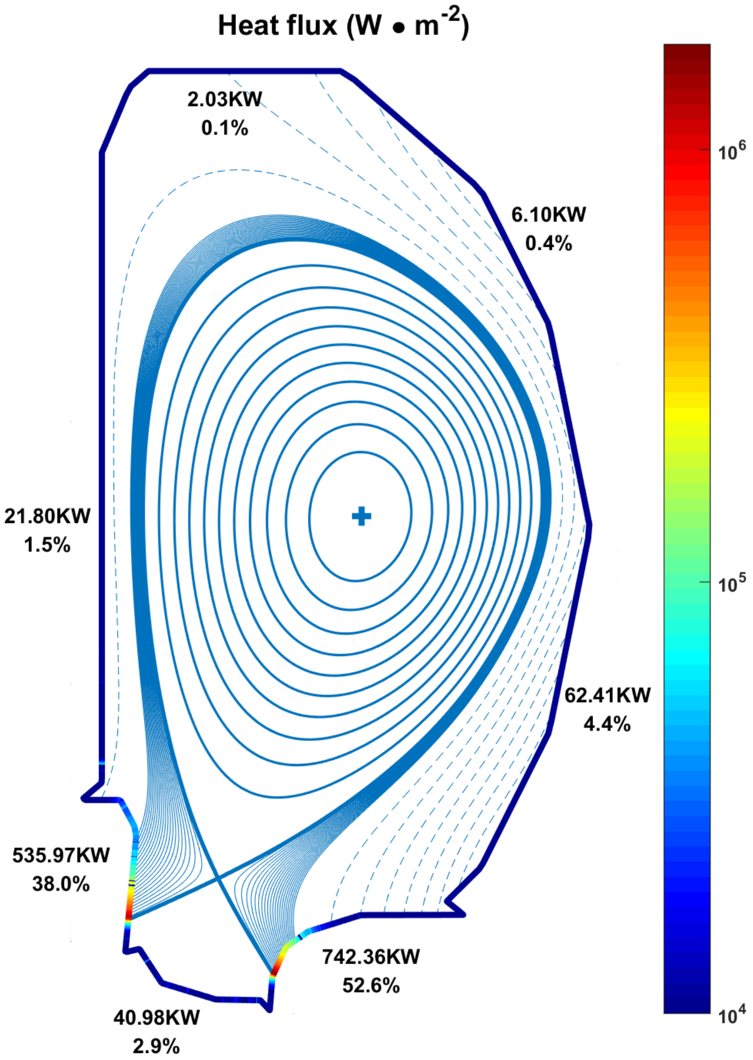

Figure 5.4.4 The heat flux profile on wall and the total energy flux on each component with P_{in} = 1.5 MW $n_{sep} = 0.36 \times 10^{19}\ m^{-3}$.

SolEdge2D-EIRENE simulations also can provide the distribution of plasma parameters (Te, Ti and n_e) along the wall for HL-2M SN configuration, as shown in figure 5.4.5.

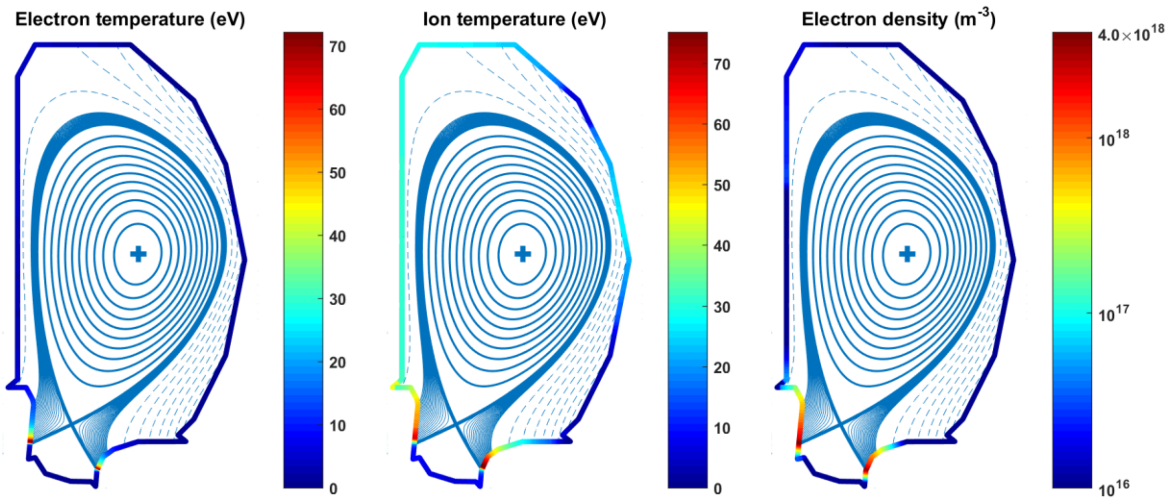

Figure 5.4.5 Example of SolEdge2D–EIRENE 2D outputs for the SN plasma: density, electron and ion temperature profile on the wall with P_{in} = 1.5 MW $n_{sep} = 0.36 \times 10^{19}\ m^{-3}$.

5. Detachment process

Then, we present some key features of the detachment process on outer target for the SN configuration. In figure 5.5.1, we plot the ion flux and pressure on outer target as a function of midplane separatrix density for the discharge. With the constant input power, the total ion flux on outer target increase with the increasing upstream density, and the tendency of increase eased after $n_{sep} = 2 \times 10^{19}\ m^{-3}$, as shown in figure 5.5.1(a). The peak value of ion flux rollover at $n_{sep} = 1.38 \times 10^{19}\ m^{-3}$, figure 5.5.1(c), and the ion flux on strike point begin to decrease at $n_{sep} = 1.15 \times 10^{19}\ m^{-3}$, figure 5.5.1(e). In figure 5.5.1(b), the integral pressure reaches the maximum value at $n_{sep} = 1.38 \times 10^{19}\ m^{-3}$ respectively. An obviously loss of peak pressure between target and upstream occurs at $n_{sep} = 1.38 \times 10^{19}\ m^{-3}$, and the roll-over for integral pressure occurs at $n_{sep} = 1.15 \times 10^{19}\ m^{-3}$.

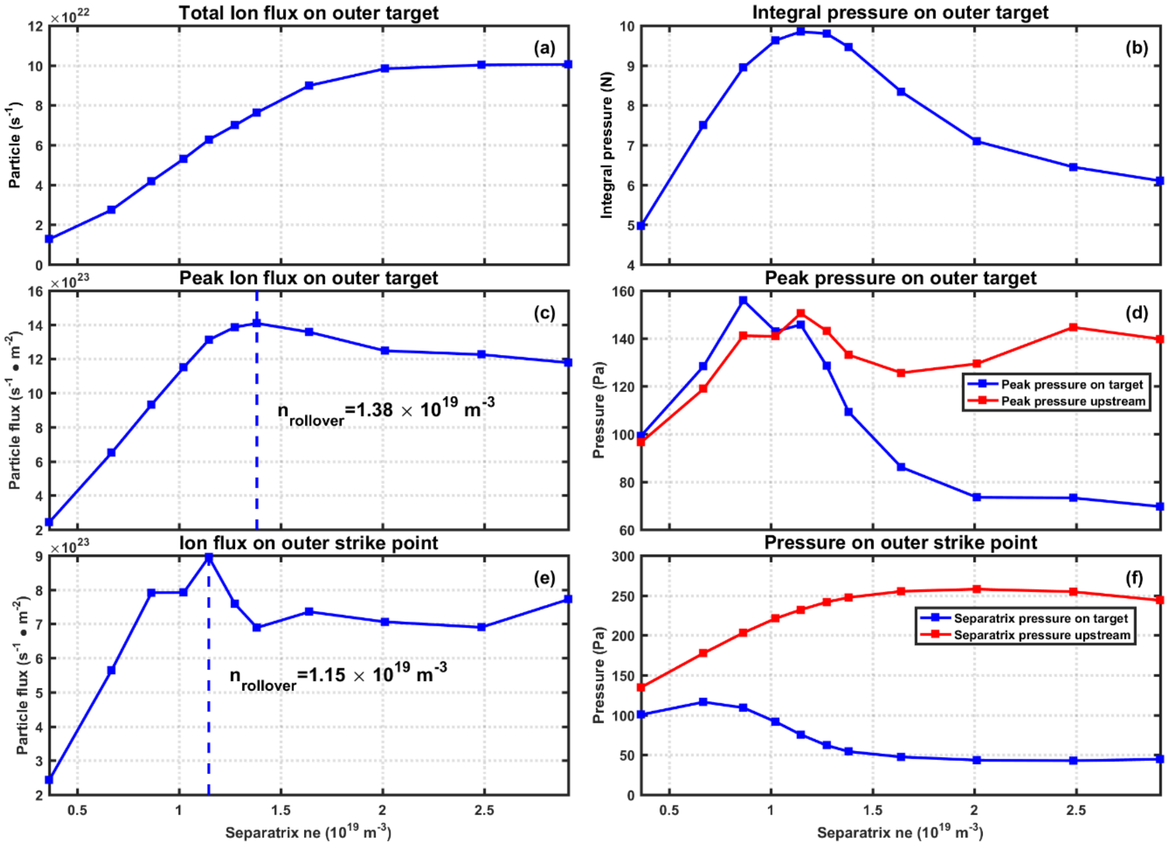

Figure 5.5.1. Density ramp simulation for SN configuration with 1.5 MW input power. In the left column, the dependence of the ion flux on outer target is shown as a function of midplane separatrix density. On the top side (a), shown the dependence of integral particle flux ($\int \Gamma_t \cdot ds$). on the middle side (c), the peak value of ion flux on outer target is shown (blue solid line) and the dash vertical line represent the rollover density. on the bottom (e), the ion flux on strike point is plotted. In right column the same dependence is plotted for pressure on outer target. On top side (b), the intergral pressure on outer target $\int p \, ds$ is shown. on the middle side (d), the blue line represents the peak value of pressure on outer target, and the red line represents the upstream pressure at the same magnetic tube as on target. on the bottom (f), the pressure on strike point (blue line) and upstream (red line) are shown.

In figure 5.5.2, we consider the dissipation of ion particle flux on outer target. In figure 5.5.2(a), the black line represents the ion flux density Γ_i which is expected to be proportional to n_u^2 according to the simple 2-point model in high-recycling regime, equation (2.2.14). In figure 5.5.2(a), the orange line shows the peak value of ion flux on outer target as a function of separatrix density.

Initially, the ion flux increases approximately linearly with the separatrix density, then clearly roll-over at $n_{sep} = 1.38 \times 10^{19} m^{-3}$, characterizing the onset of detachment. A degree of detachment (DoD) can be defined as the ratio of the target ion flux expected from the 2-point model and the simulation result [1, 2], the DoD being ≫1 for deep detachment. The DoD, orange line in figure 5.5.2(b), reaches values up to 15. It should be noticed that the value of DoD is not absolute, it depends on the separatrix density, for which we force DoD=1, and in this case we use the lowest density.

[1] Loarte A, Monk R D and Martin-Solis J R 1998 Nucl. Fusion 38 331
[2] C. Theiler, et al 2017 Nucl. Fusion 57 072008

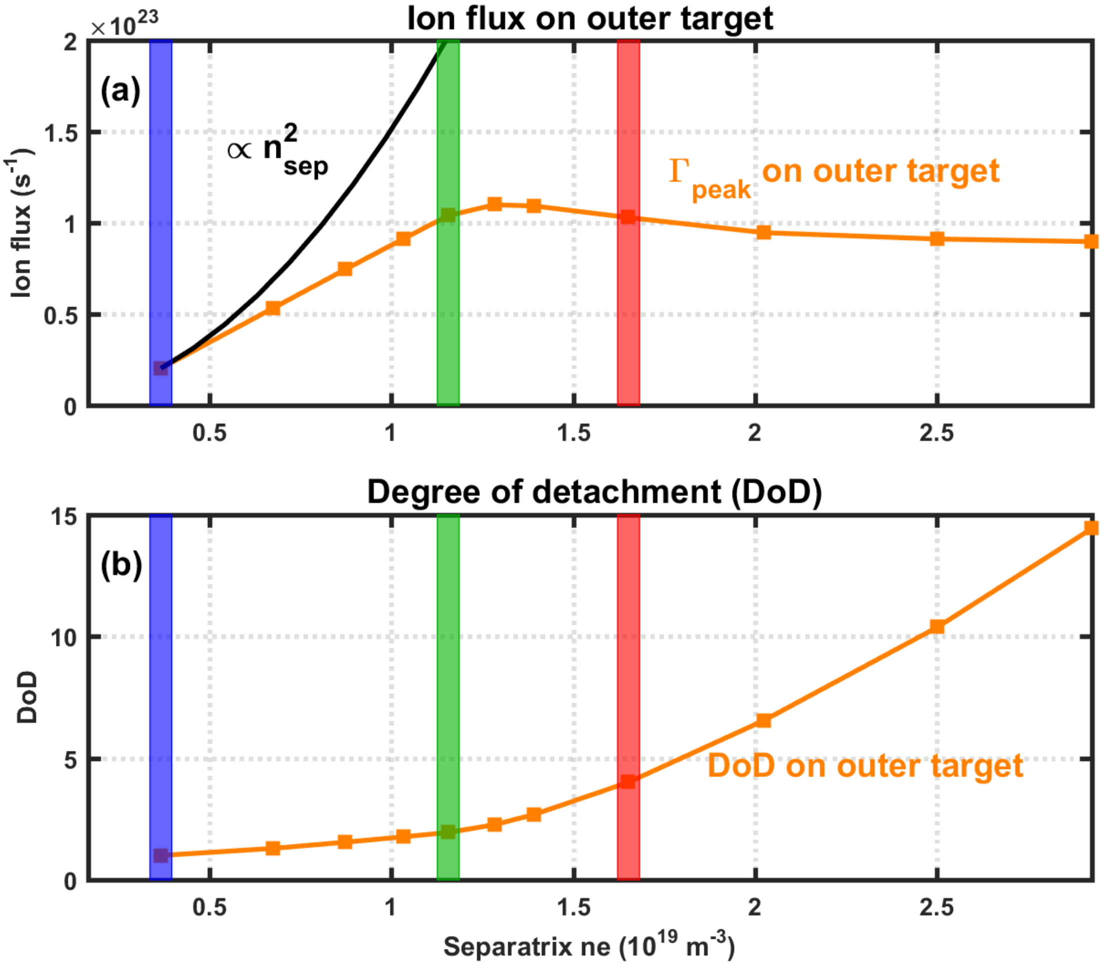

Figure 5.5.2. (a) Peak value of ion particle flux on the outer target (orange line) and expected ion particle flux based on 2-point model estimations (black line), expected to be proportional to $\langle n_u \rangle^2$. (b) Degree of detachment (DOD) on the outer target (orange line). The shaded region represents the three different plasmas, with separatrix densities $n_{sep} = 0.36 \times 10^{19} m^{-3}$ (blue), $n_{sep} = 1.15 \times 10^{19} m^{-3}$ (green), $n_{sep} = 1.64 \times 10^{19} m^{-3}$ (red). Profiles for these plasmas are shown in figure 5.5.3, using the same color code.

In figure 5.5.3, the density, electron temperature and total pressure profiles at the outer midplane and the divertor plate have been compared for different stages in the detachment process. Here, subscripts u and t denote upstream and target quantities and we use the normalized poloidal flux, $\psi_x = (\psi - \psi_m)/(\psi_b - \psi_m)$ as radial coordinate, where ψ_m is the poloidal flux value at the magnetic axis, and ψ_b its value at the separatrix. The three columns of profiles correspond to the three different separatrix densities marked by shaded regions in figure 6, the same color code being used. At the lowest density (left), the electron temperature and pressure match across the SOL between midplane and divertor target, indicative of the sheath limited regime, as shown in figure 5.5.3(b, c). Here the divertor electron pressure is normalized by a factor of 2 to account for the dynamic pressure of the sonic flow into the sheath in front of the target. At intermediate density, figure 5.5.3(e, f), a clear temperature gradient along the magnetic field already exists, Te on target is reduced to <20 eV. This is the high recycling regime. In the region near the strike point, Te is below 10 eV, figure 5.5.3(e), the pressure on target drops below that observed on the midplane, which indicates a local detachment at the strike point. This drop occurs in the near SOL with pressure balance still maintained in the far SOL. Finally, for the highest density case, Te on the target drops below 5 eV and a clear pressure gradient along the field is established on the entire target, figure 5.5.3(h, i), indicating the detachment plasma on outer target.

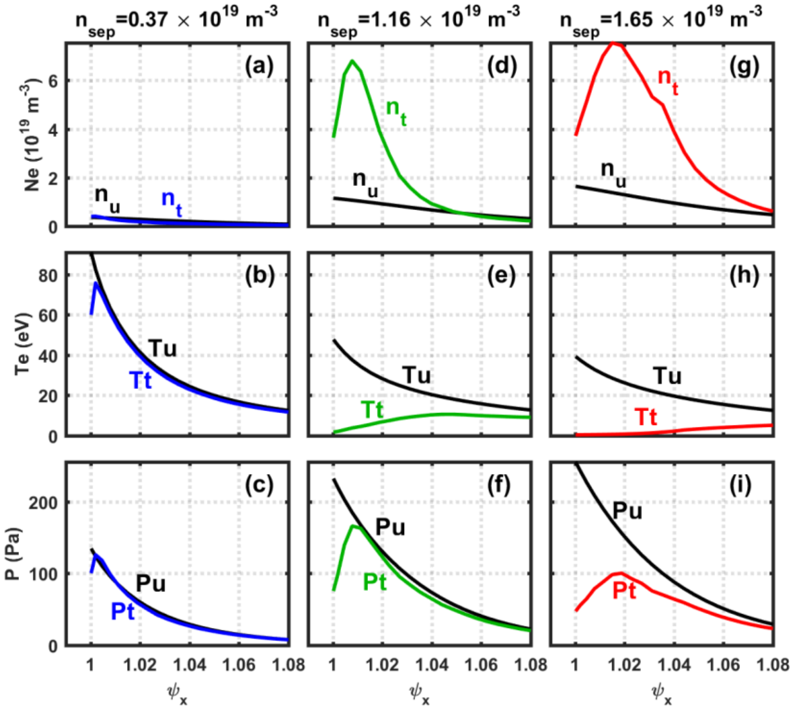

Figure 5.5.3. Comparison of density, temperature, and pressure profiles at the upstream (midplane) and the outer target versus increasing densities for SN configuration. The left column corresponds to the lowest separatrix density, as well as the blue shaded region in figure 5.5.2. The middle and right column correspond to intermediate and highest densities, also to the same color shaded region in figure 5.5.2.

Figure 5.5.4 shows the 2D profiles of ne and Te for the three different densities cases correspond to figure 5.5.3. For the attached plasma, $n_{sep} = 0.36 \times 10^{19} m^{-3}$, the electron temperature Te>20 eV and almost uniform in the region close to separatrix, figure 5.5.4(d). As the plasma density increases,$n_{sep} = 1.15 \times 10^{19} m^{-3}$, the temperature gradually decline from X-point to target along the magnetic line, and reduced to <5eV at strike point, figure 5.5.4(e). However, the volume of plasma with Te<5 eV is very small and concentrate near the strike point, it means that this case is a partial detachment. For the right column, $n_{sep} = 1.64 \times 10^{19} m^{-3}$, the profiles exhibit a very low temperature Te< 1 eV, and high density $n_e > 1 \times 10^{20} m^{-3}$ along the target, figure 5.5.4(c,f). Moreover, the volume of low Te greatly extends not only from the strike point along the target surface but also upstream along the separatrix.

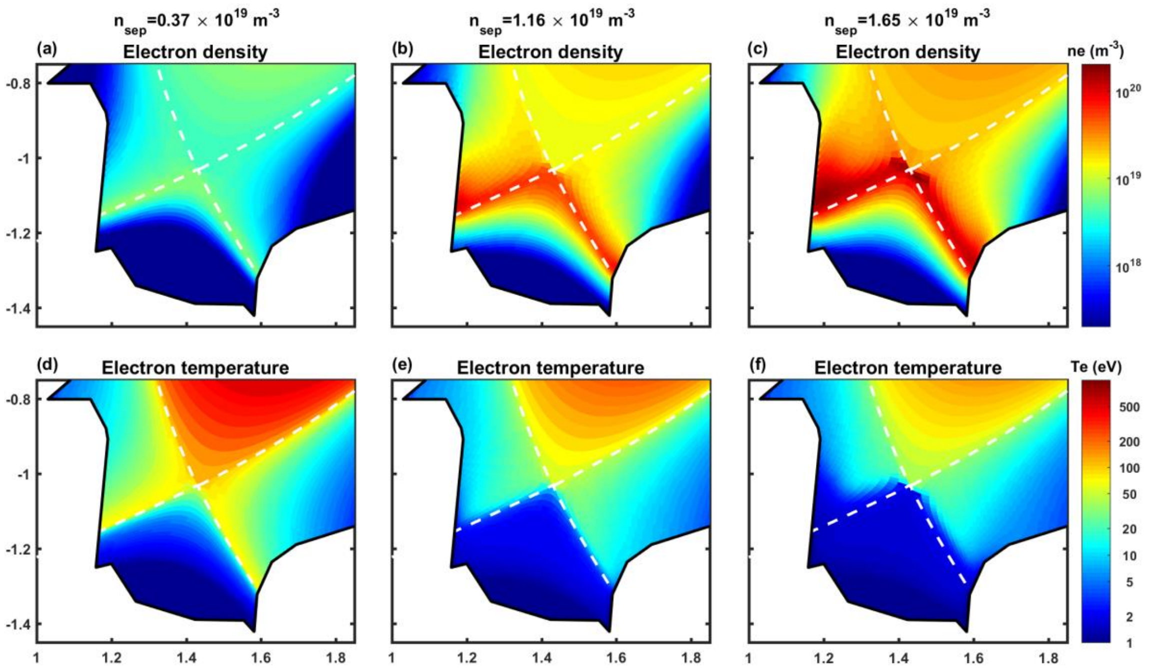

Figure 5.5.4. Te and ne profiles in divertor region for SN configuration with input power Pin=1.5MW, correspond to the three different densities cases as shown in figure 5.5.3.

The 2D profiles of neutral pressure and density for the three different plasmas density simulation are illustrated in figure 5.5.5. For lowest separatrix density, $n_{sep} = 0.36 \times 10^{19} m^{-3}$, neutral pressure and density are almost 0, figure 5.5.5(a, d).For middle column, ,$n_{sep} = 1.15 \times 10^{19} m^{-3}$, the neutral pressure region start to detach from the target, figure 5.5.5(b). As the plasma density increases, $n_{sep} = 1.64 \times 10^{19} m^{-3}$, the neutral pressure and density region extend along the separatrix to X-point, figure 5.5.5(c, f).

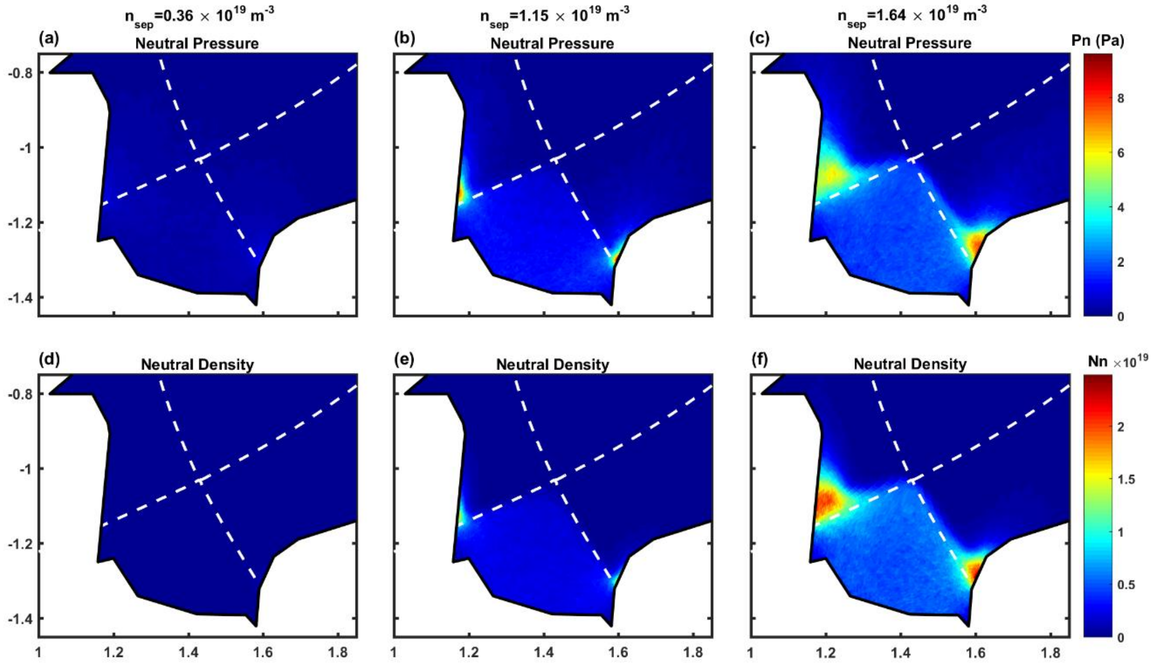

Figure 5.5.5. Neutral pressure and density in divertor region for SN configuration with same input power Pin=1.5MW. The left column corresponds to the low separatrix density, $n_{sep} = 0.36 \times 10^{19} m^{-3}$(sheath limited). The middle and right column correspond to mediate (high recycling), $n_{sep} = 1.15 \times 10^{19} m^{-3}$, and highest densities (detachment), $n_{sep} = 1.64 \times 10^{19} m^{-3}$.

6. Evolution of plasma parameters from midplane to target

In order to gain some more information on the SN plasma detachment process, the distribution of the heat flux, density, electron and ion temperature profiles on outer target are compared on figure 5.6.1 and the three different density cases in this figure correspond to figure 5.5.3.

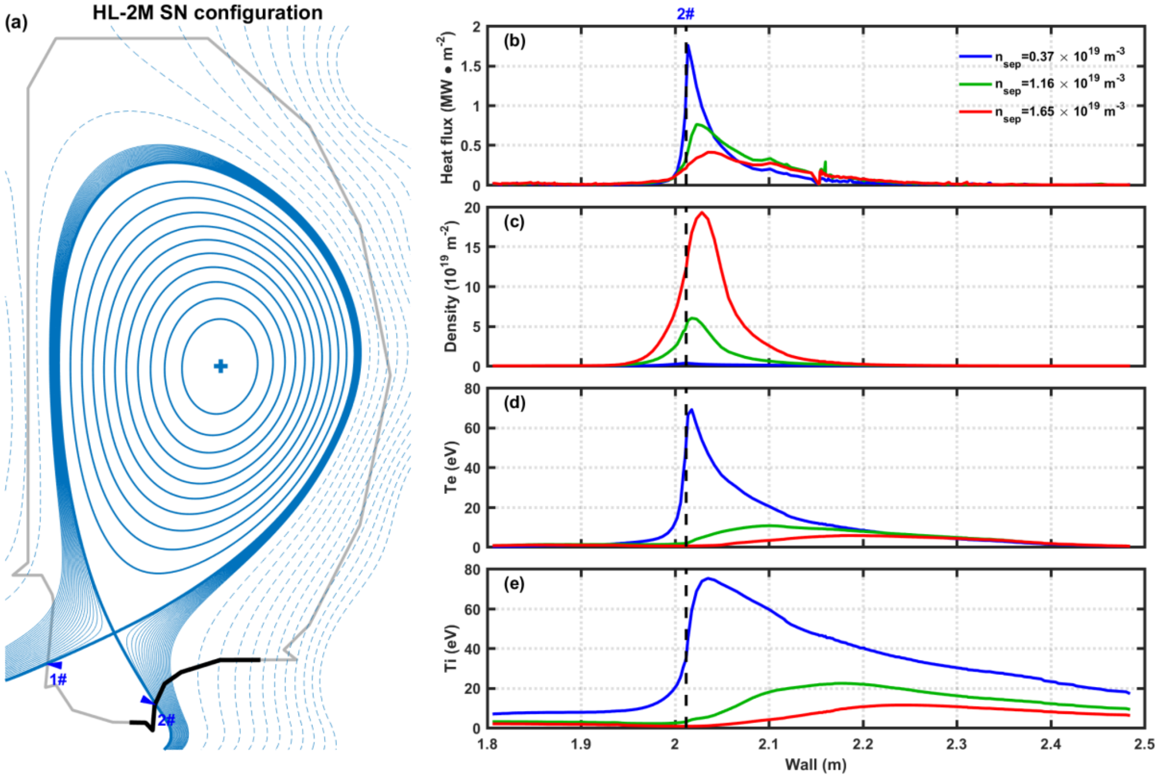

Figure 5.6.1. (a) typical SN magnetic equilibrium, the bold black line on the vacuum chamber wall represents the range of the outer target we studied. (b-e) Total heat flux, density, electron and ion temperature profiles along the outer target. The vertical, dash lines indicate the outer strike point. The three lines with different colors represent the three different densities plasma,.

As shown in figure 5.6.1(b), with the increasing separatrix density, plasma transfer from sheath limited to detachment phase, the peak value of heat flux reduces up to a factor of approximately 4 and negligible changes at distance from strike point >0.1m on the wall. With the separatrix density increasing from $0.36 \times 10^{19} m^{-3}$ to $1.64 \times 10^{19} m^{-3}$, by a factor ≈ 4.5, the peak value of density on outer target increase by a factor approximately 60, figure 5.6.1(c). Figure 5.6.1(d,e) reveals a clear reduction in Te and Ti, up to a factor 10 and a increase on the distance between the density peak and temperature peak, from ~5mm to ~20mm. It should be noticed that the heat flux q_t include the energy carried by the incidence particles (electron, ion and neutral particles), recombination energy. The radiated power on the wall is not taken into account.

To quantitative analysis of q_t, the heat flux profiles on outer target are plotted in figure 5.6.2. We focus on the peak region of heat flux on the outer target, correspond to the range with bold black line on the vacuum chamber wall as shown in figure 5.6.2(a), also to the range marked by the 'outer target' brace in figure 5.6.2(b). In figure 5.6.2(c, e), the plasma transfer from sheath limited to high recycling phase, the total power on outer target is almost no changed. Then the density increased to $n_{sep} = 1.64 \times 10^{19} m^{-3}$, figure 5.6.2(g), plasma detached, the total power decreases ~25%. In fact, when the heat flux transport by plasma decrease, the radiation power reached on the target increase, so the reduction of the total power on target is not so substantial. In the whole detachment process, the peak value of heat flux on outer target continues to reduces, up to by a factor of 4 and the λ_q for parallel heat flux continues to increase from ~8mm to 20mm, by a factor of 150%, in figure 5.6.2(d, f, h). The parallel heat flux reached the outer target is mapped to the midplane, and λ_q represents the width of the magnetic tube in 2-point model. Moreover, the position of the heat flux peak moves outward from the strike point during the plasma density ramp.

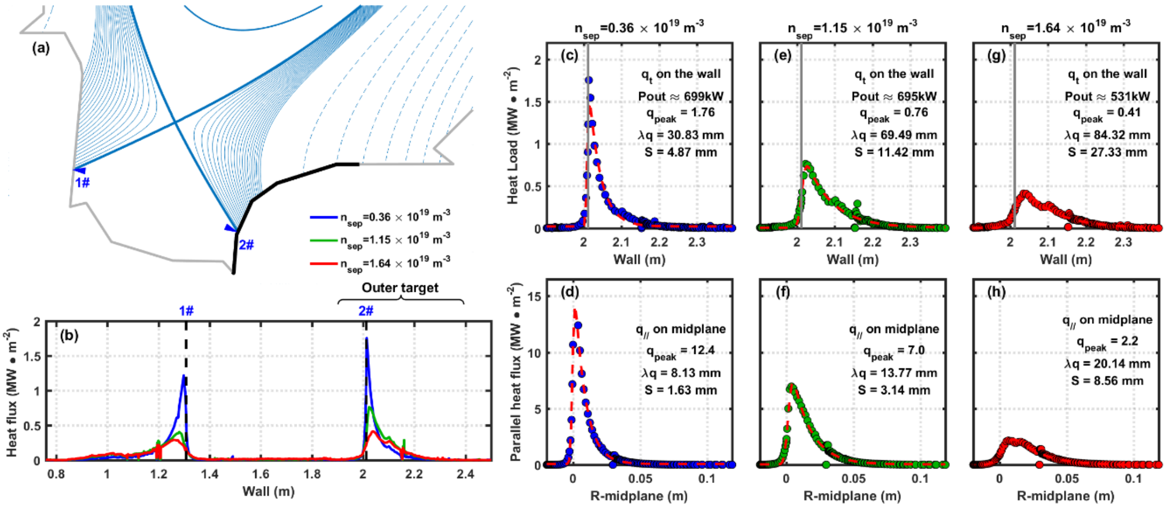

Figure 5.6.2. (a) the divertor region of flux surface. The bold black line on the vacuum chamber wall represent the outer target region. (b) The heat flux on the wall for three cases in figure 5.5.3 with the same color. The vertical, dash lines indicate the inner (1#) and outer (2#) strike point, also correspond to the marker '1#' and '2#' in (a). (c-h) Comparison of the heat flux on outer target q_t and the parallel heat flux $q_{\parallel}$ mapped to midplane. The shape parameters of the heat flux profile are also listed. The q_t on the wall is the heat flux transport by plasma. The parallel heat flux $q_{\parallel}$ is the parallel heat flux transported by plasma to the wall. The q_{peak} is the peak value of the profile. The geometry parameters λ_q and S represent the width and the spreading of profiles. The dash red line is a fit of exponential spread by Gaussian, $f = \frac{f_0}{2} e^{\left[(S/2\lambda_q)^2 - (x-x_0)/\lambda_q\right]} \times err + backgroud$. Here, f_0 is amplitude of the exponential, x_0 is center of the function, err is the complementary error function.

Then the figure 5.6.3 shows the components of the heat flux profiles on the wall: energy carried by electron, ion and neutral particles, potential energy from recombination. In figure 5.6.3(a), sheath limited regime, the energy carried by electron is dominates, then the ion, and the heat flux from neutral and recombination can be neglected. In high recycling regime, figure 5.6.3(b), the energy of electron is reduced and the effect of neutral and recombination become more obvious with the rising of plasma density. In the right side, figure 5.6.3(c) shows that, for detachment plasma, the heat flux on the wall dominated by the energy of recombination and the effects of electron, ion, neutral particles are similar.

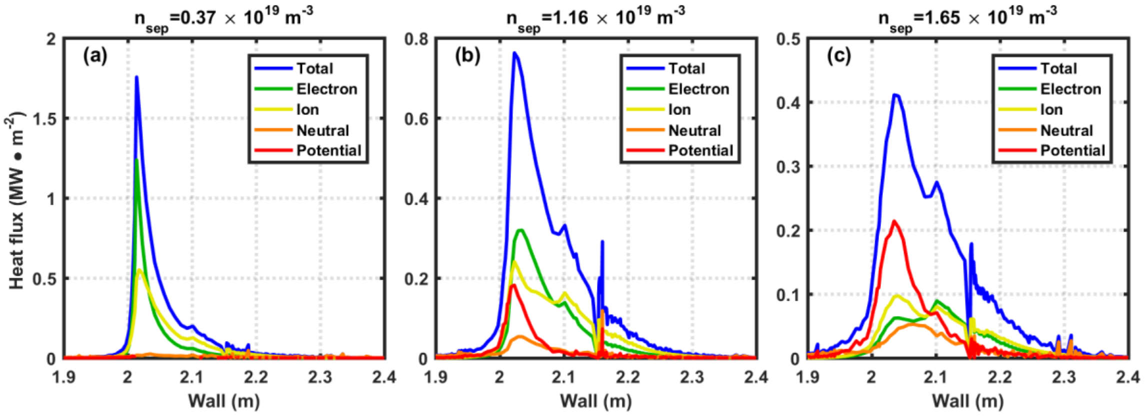

Figure 5.6.3 Components of the heat flux profiles on the wall. Blue lines represent the total power transport by plasma. It should be noticed that the radiation power is not included. The green, yellow and orange lines represent the energy of electron, ion and neutral particles separately.

The ion flux profiles on outer target for the three different density phases are plotted in figure 5.6.4. In figure 5.6.4(c, e) As the density increasing from $n_{sep} = 0.36 \times 10^{19} m^{-3}$ (sheath limited) to $n_{sep} = 1.15 \times 10^{19} m^{-3}$ (high recycling), by a factor approximately 3, the peak value of ion flux on the outer target Γ_t increases nearly 5-fold and the total particle flux reached the outer target increases 6-fold. But the width of ion flux decreases from the 47mm to 39mm for Γ_t and 9.8mm to 7.3mm for parallel flux $\Gamma_{\|}$, as shown in figure 5.6.4(d, f). During the process by which plasma transfer from high recycling to detachment, the peak value for both Γ_t and $\Gamma_{\|}$ almost remains unchanged, $\Delta_{\Gamma t}{\sim}1\%$ and $\Delta_{\Gamma\|}{\sim}4\%$, figure 5.6.4(g, h). At the same time, total flux reached outer target increased almost 50%. The width of $\Gamma_{\|}$ profile λ_{Γ} rises by ~11%. Comparison with evolution of the heat profiles in figure 5.6.2, it is apparent that λ_{Γ} is independent on λ_q.

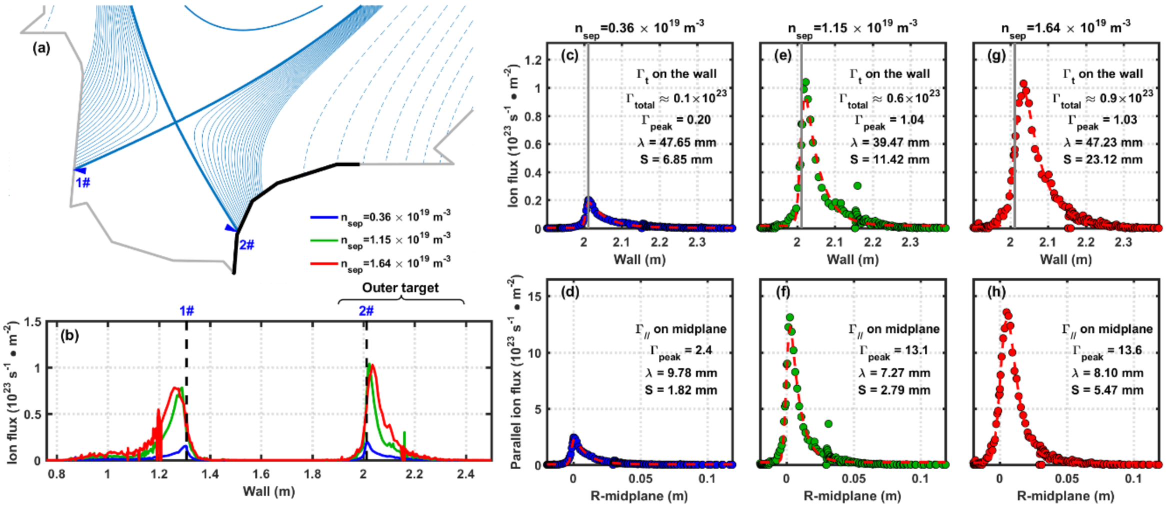

Figure 5.6.4. Quantitative analysis of ion flux profile on outer target. (a) The divertor region flux surface. (b) the ion flux profiles on the wall for three cases in figure 5.5.3. (c-h) Comparison of the ion flux profiles on outer target Γ_t and the parallel heat flux profiles on the midplane $\Gamma_{\|}$. The Γ_{peak} is the peak value of the profile and the meaning of geometry parameters λ and S are same with them in figure 5.6.2.

As the λ_q, representing the width of the magnetic tube for heat flux transport, can effectively reduce the peak value of heat flux on target, we want to get more information about the λ_q. The profiles of density and temperature on midplane has been analyzed in figure 5.6.5. During the separatrix density increase from $n_{sep} = 0.36 \times 10^{19} m^{-3}$ to $n_{sep} = 1.15 \times 10^{19} m^{-3}$ in attached regime, the radial width of density profile λ_{ne} increase ~10%, and the change of λ_{ne} in the region between $n_{sep} = 1.15 \times 10^{19} m^{-3}$ and $n_{sep} = 1.64 \times 10^{19} m^{-3}$, is also ~10%, shown in figure 5.6.5(a, d, g). Since the λ_q increase by a factor of 150% during the same plasma density ramp process, much more than λ_{ne}, there is no apparent correlation between the radial width of density profile λ_{ne} and λ_q. The width of temperature profiles, λ_{Te}, continuously increase from 13.4 mm, figure 5.6.5(b), to 28.22 mm, figure 5.6.5(h), by a factor of ~110%. The degree of variability in λ_{Ti} frofiles is between λ_{ne} and λ_{Te}, figure 5.6.5(c, f, i). Obviously, comparison with λ_{ne}, the change λ_q is more colosely related with the λ_{Te} and λ_{Ti}.

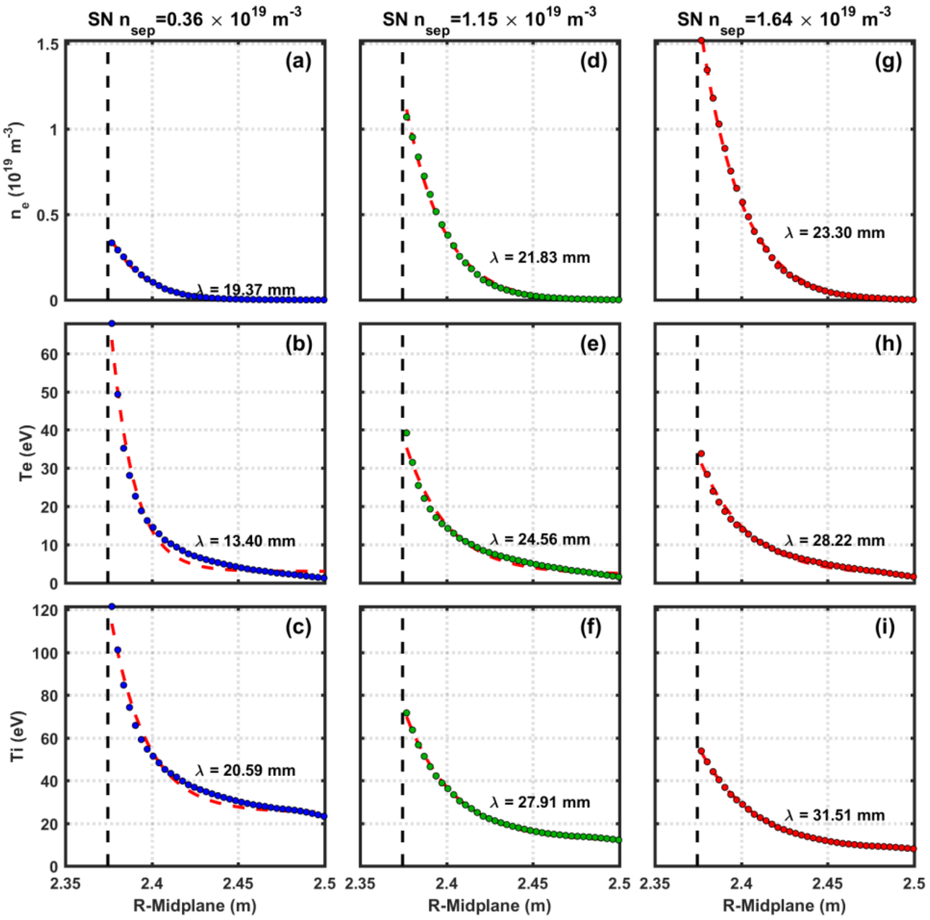

Figure 5.6.5. The density, electron temperature and pressure profiles on the midplane for three cases in figure 5.5.3. The vertical black dash line represents the plasma separatrix.

Then the λ of upstream n_e, T_e, T_i and parallel heat flux $q_{//}$ as a function of separatrix density is shown in figure 5.6.6. The width of ne profiles on upstream λ_{ne} (red line) increases in least, only increases ~20% before detachment and ~4% after detachment. During the attached regime, from $n_{sep} = 0.36 \times 10^{19} m^{-3}$ to $n_{sep} = 1.64 \times 10^{19} m^{-3}$, the trend of λ_{Te} and λ_{Ti} are similar to λ_q. For detachment plasma, $n_{sep} > 1.64 \times 10^{19} m^{-3}$, the λ_{Te} continues increasing, but λ_{Ti} and λ_q are flattened. It is apparent that the density ramp leads to a temperature profiles flatter on midplane in SOL region and extends the magnetic tube for transfer the heat flux, while the profiles changes little.

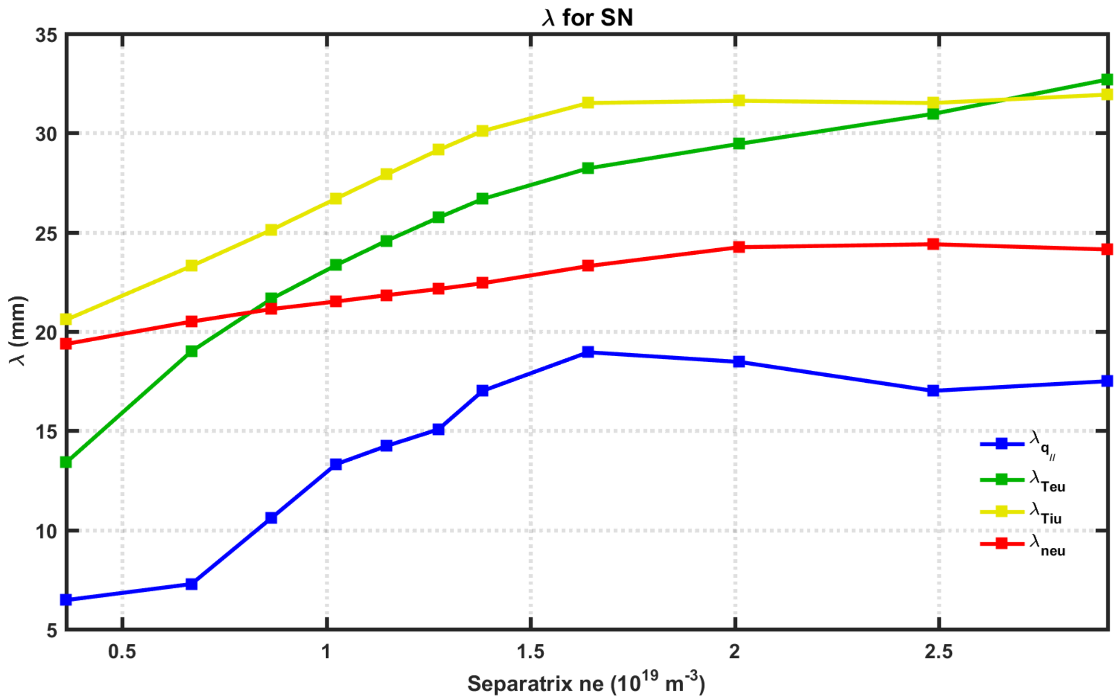

Figure 5.6.6. The width of upstream T_e (green line), T_i (yellow line), n_e (red line) and $q_{//}$ (blue line) profiles evolve during the plasma density ramp.

In figure 5.6.7, the plasma density n_t, ion temperature $T_{i,t}$ and electron temperature $T_{e,t}$ on outer target are plotted as a function of separatrix density. The roll-over of density on strike point occurs at $\mathrm{n_{sep}} \sim 1 \times 10^{19}\ \mathrm{m^{-3}}$, and the peak value of density continues increases. The Te on strike point drops to 10eV at $\mathrm{n_{sep}} \sim 0.87 \times 10^{19}\ \mathrm{m^{-3}}$, and the peak value of Te drop to 10eV at $\mathrm{n_{sep}} \sim 1.15 \times 10^{19}\ \mathrm{m^{-3}}$.

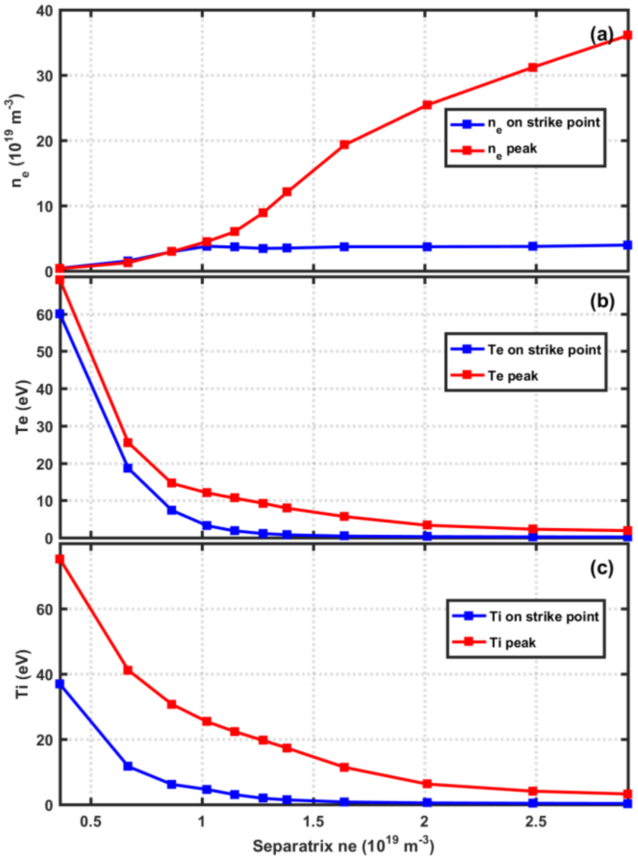

Figure 5.6.7. Plasma density, ion and electron temperature on outer strike point are plotted as a function of separatrix density for SN configuration. The blue lines represent the parameters on strike point and the red lines represent the peak value of parameters on outer target.

In figure 5.6.8, the peak value of neutral pressure (Pn) and neutral pressure on outer strike point for SN configuration is plotted as a function of the separatrix density. The peak value of Pn roll over at $n_{sep} = 1.38 \times 10^{19}\ m^{-3}$, same as the ion particle flux, and the Pn on strike point roll over at $n_{sep} = 1.15 \times 10^{19}\ m^{-3}$.

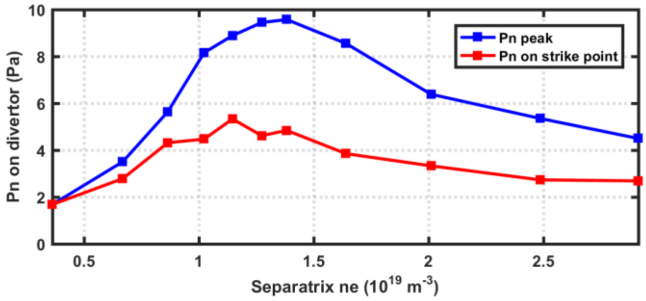

Figure 5.6.8. Neutral pressures on outer target as a function of separatrix density for SN configuration. The blue line represents the peak value of Pn and the red line represents the Pn on strike point.

7. Detachment window

Then, we start to investigate the energy dissipation in divertor region. Figure 5.7.1 shows the evolution of total radiation power during the plasma density ramp with the constant input power. When the plasma density is low, $n_{sep} \leq 0.9 \times 10^{19} m^{-3}$, the ratio of radiation power is almost 20% and change a little. With increasing the plasma density, $0.9 \times 10^{19} m^{-3} \leq n_{sep} \leq 1.64 \times 10^{19} m^{-3}$, the radiation power increase linearly with the separatrix density, from 20% to 70%. The tendency of increasing eased after $n_{sep} = 1.64 \times 10^{19}\ m^{-3}$ and the final value of radiation power ≈80%. The heat flux on outer target is higher than heat flux on inner target, by a factor of ~50%, at low density and decrease faster during the plasma density ramp. Finally, the thermal load on outer target almost equal to it on inner target, with the detachment plasma.

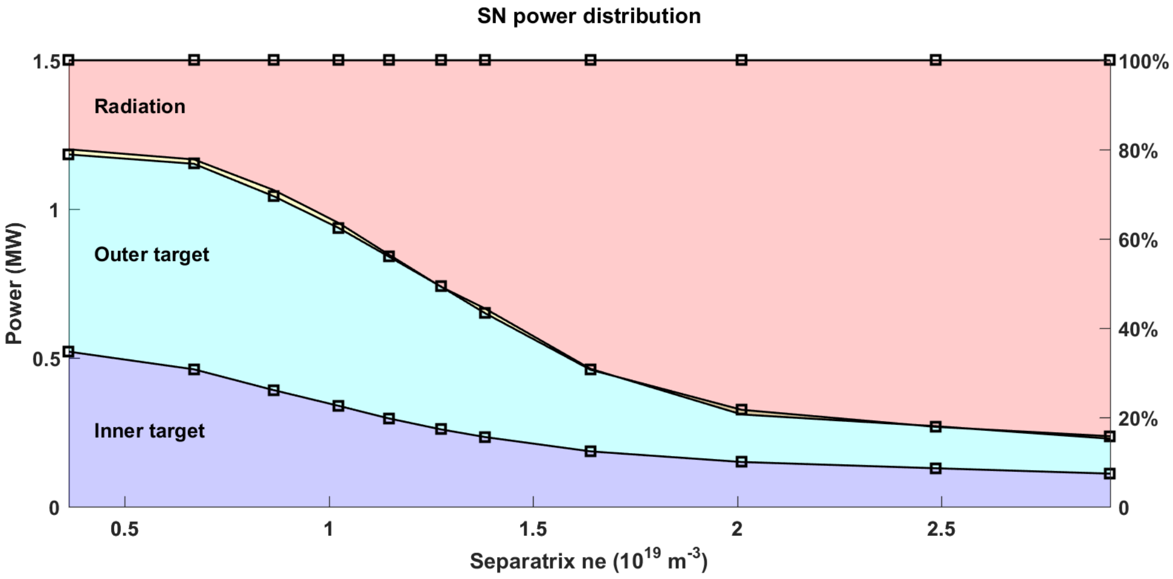

Figure 5.7.1. Total radiation power(red), heat flux on outer target (blue) and heat flux on inner target (purple) evolves during the plasma density ramp, with the constant input power =1.5MW.

The evolution of radiation profiles during the detachment process driven by separatrix density ramps are shown in figure 5.7.2. Focusing on the radiation along the outer leg, it is clear that, initially, the radiation region is concentrated near the strike point (figure 5.7.2(a)). Later in time, as the plasma density increases, and leg cools down (figure 5.7.2(b) and (c)) the front of the radiation region moves upstream towards the X-point. In the following, we will use the front of the cold, radiative region as the location of the detachment region. We determine this location as the position where the radiation power along the outer leg has dropped to half of its peak value. Then we evaluate the connection length of front edge along the outer leg between the strike point and X-point as a function of separatrix density. The result of this analysis is presented in figure 5.7.2(d).

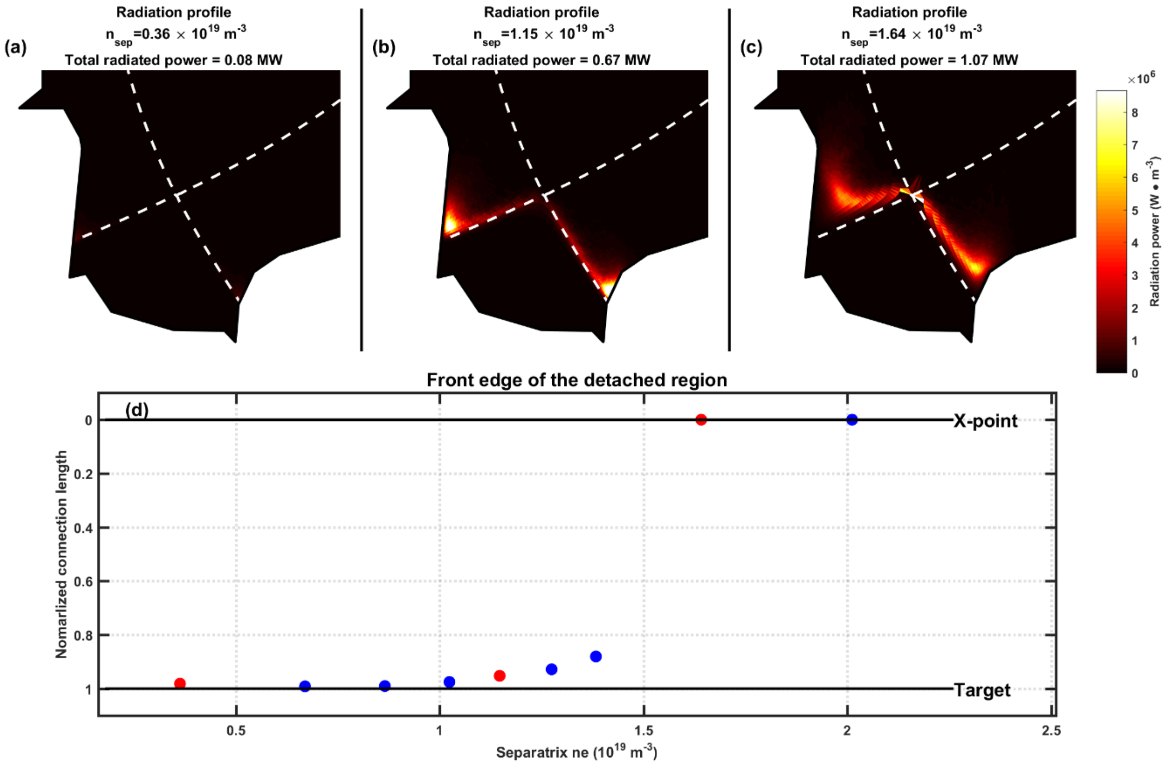

Figure 5.7.2. (a)–(c) Radiation profiles in the divertor volume for different time periods during the density ramp simulations. (d) Position of the front edge along the outer leg as a function of separatrix density (blue dots). The red dots represent the three different densities cases as shown above (a-c). We use the normalized connection length $l_{\|}/(l_{Target} - l_{xpoint})$

From the figure 5.7.2(d), the radiation starts to detach from the target at a separatrix density $n_{sep} \sim 1 \times 10^{19} m^{-3}$, about 30% lower than the roll-over density of the outer target ion flux, $n_{sep} = 1.38 \times 10^{19} m^{-3}$, as shown in figure 5.5.1(b) , and reach the X-point at $n_{sep} \sim 1.64 \times 10^{19} m^{-3}$. The density window between the start of the radiation front movement and when it arrives at the X-point $\Delta n_{sep} \sim 0.6 \times 10^{19} m^{-3}$.

The previous paragraph explained detachment process in the entire divertor region, include the dissipation of power, momentum and particle flux along the open field lines from the midplane to the divertor. The plasma density ramp simulation starts from attached plasma, $n_{sep} = 0.36 \times 10^{19} m^{-3}$, the electron temperature and pressure matched across the SOL between midplane and divertor target, figure 5.5.3(a, b, c). Then the separatrix density increase to $n_{sep} = 0.67 \times 10^{19} m^{-3}$, the total radiation power growth clearly tern up, figure 5.7.1, and the radiation region is on the target, figure 5.7.2. As the plasma density continues increasing, $n_{sep} = 0.87 \times 10^{19} m^{-3}$, the electron density on strike point drop to $T_{t\_st} \sim 10eV$, figure 5.6.7, the radiation region began to detach from the target, figure 5.7.2. There is also a clear pressure gradient along the separatrix from midplane to strike point, indicating a partial detachment close to the strike point, but further out into the SOL the plasma remains attached. Then the density on strike point roll-over at $n_{sep} = 1 \times 10^{19} m^{-3}$, at the same time, the electron temperature on strike point drop to 5eV, figure 5.6.7. The ion flux on strike point roll-over at $n_{sep} = 1.15 \times 10^{19} m^{-3}$ and a clear pressure gradient along the field has also established from midplane to outer target, figure 5.5.3(e,f). The peak value of ion flux and neutral pressure on outer target roll-over at $n_{sep} = 1.38 \times 10^{19} m^{-3}$, as shown in figure 5.5.3(c), 5.6.8. At the same time, a clear loss between peak value of upstream and target pressure begin to appear, figure 5.5.3(d). At $n_{sep} = 1.64 \times 10^{19} m^{-3}$, the radiation front reach the X-point, figure 5.7.2, the growth velocity of total radiation power is decelerated obviously, figure 5.7.1, and the λ_q stops increasing, figure 5.6.6.

The simulation results presented in this section show key characteristics of detachment, such as reduction of particle and heat fluxes reaching the target, a cooling of the plasma in the divertor leg, and the increase of parallel pressure gradients. In the following, when we compare the detachment behavior in different geometries, we mainly focus on the integrated and local drop of ion particle flux, energy dissipation, and pressure loss along the outer divertor leg from upstream (midplane) to target. The amplitude of the roll-over in ion particle flux and pressure are used as an indication of the level of detachment, and the upstream density range between the start of the radiation front movement and when it arrives at the X-point, is called the detachment window.

8. Simulation setup of SF+ and SF-

We now explore the effect of alternative divertor configurations. The detachment process in SN, SF+ and SF- configurations have been simulated with the same parameters as for the SN cases, listed in table 5.8.1. In figure 5.8.1 (d) - (f), the radial profile of poloidal flux expansion f_x, connection lengh $L_{\|}$ and incidence angle α_t along the outer divertor plate are plotted against the normalized magnetic flux ψ_x. The corresponding magnetic equilibriums are shown in figure 5.8.1 (a)-(c). For the SF+ configuration, the additional X-point in the private flux region strongly increases $L_{\|}$ near the strike point, as shown in figure 5.8.1 (e). At the flux surface closest to the separatrix, Δr~0.1mm on midplane, the parallel connection length is $L_{\|} \approx 120\ m$ for SF+ and $L_{\|} \approx 20\ m$ for SN. But the other geometry parameters, f_x and α_t, have not been affected and the position of strike points is also similar. In the SF- configuration, the second X-point in the SOL region obviously increases the flux expansion f_x, by a factor from 2 to 10, for the whole divertor target, figure 9(d). The incidence angle on the target has also been reduced from $\alpha_t \approx 4°$ to $\alpha_t \approx 1°$, due to short distance between the additional X-point and target, as shown in figure 5.8.1 (f).

Parameter	**D**	$\boldsymbol{\nu}$	$\boldsymbol{\chi_e \chi_i}$	$\boldsymbol{P_{in}}$
Value	$1\ m^2 S^{-1}$	$0.6 m^2 S^{-1}$	$2 m^2 S^{-1}$	1.5MW

Table 5.8.1 Input parameters for the SolEdge2D–EIRENE simulations.

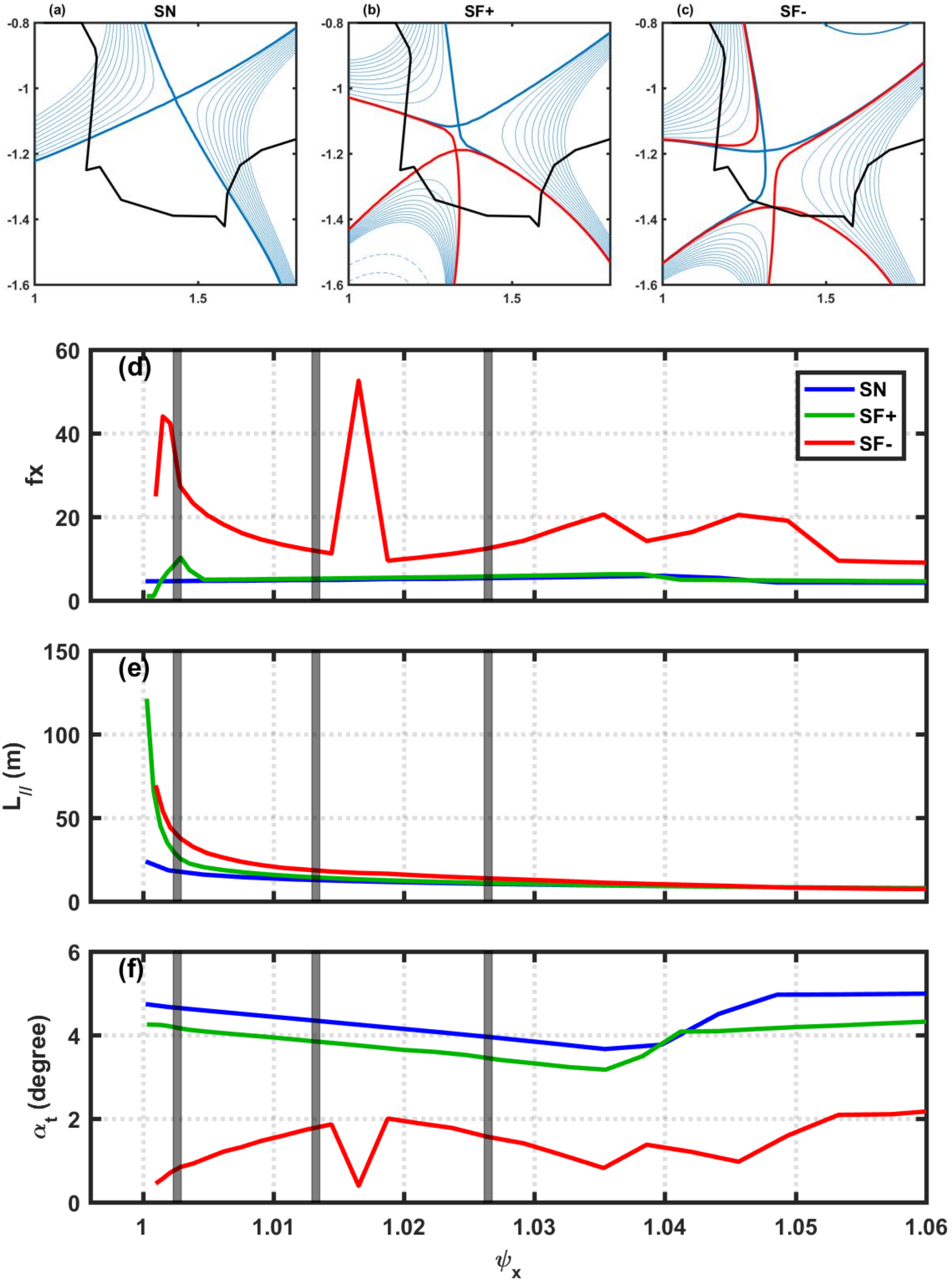

Figure 5.8.1 (a)-(c) show the divertor region of HL-2M SN, SF+, SF- configurations. For the snowflake minus plasma, the second X-point is near the wall. Panels (d)-(f) show radial profiles of poloidal flux expansion, connection length and magnetic field line incidence angles at the target of outer divertor leg. The colors correspond to the equilibria in (a)-(c). The vertical black lines represent the values of ψ_x corresponding to distances of 1mm 5mm and 10mm to the separatrix at the midplane.

Some basic characteristics of SF+ density ramp simulation are illustrated in figure 5.8.2. The power inject into SOL region is also fixed at 1.5MW.

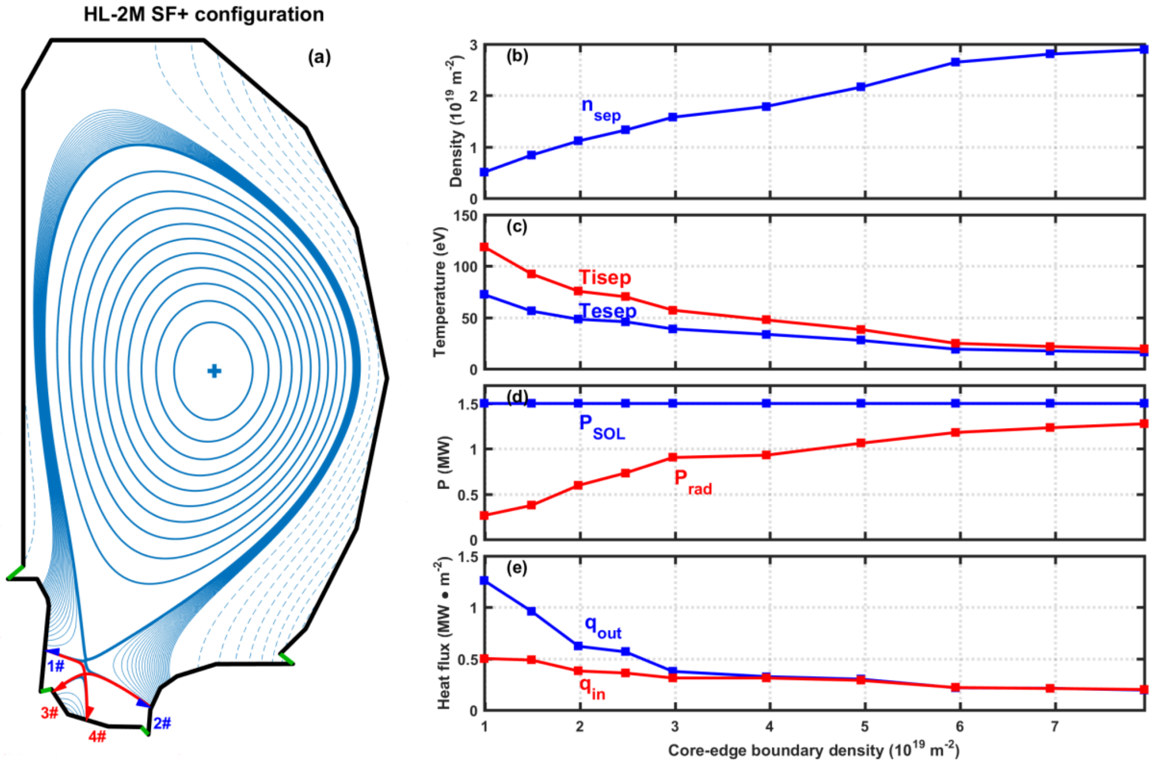

Figure 5.8.2 (a) SF+ magnetic equilibrium. (b) separatrix electron density on midplane, also called upstream density. (c) upstream electron temperature (blue line) and ion temperature (red line). (d) Power injected into the SOL region (blue) and radiative power computed during the simulation (red). (e) peak value of heat flux outer target (blue line) and inner target (red line).

The meshes of SF+ configuration for SolEdge2D-EIRENE code are plotted in figure 5.8.3.

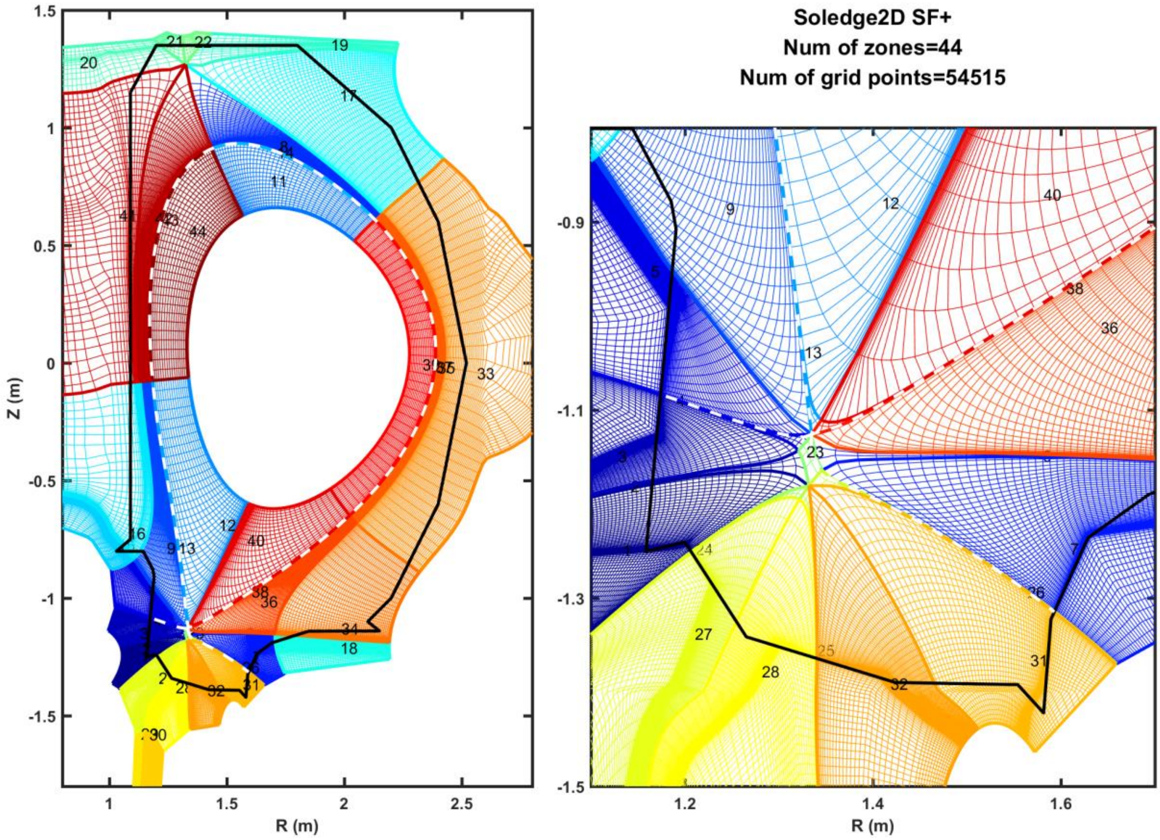

Figure 5.8.3 Grid of HL-2M SF+ configurations used for SolEdge2D-EIRENE code.

Figure 5.8.4 shows 2D contour plots of density, parallel Mach number, electron and ion temperature for the HL-2M SF+ configuration and the simulation parameters are listed in table 5.8.1, $n_{sep} = 0.5 \times 10^{19}\ m^{-3}$.

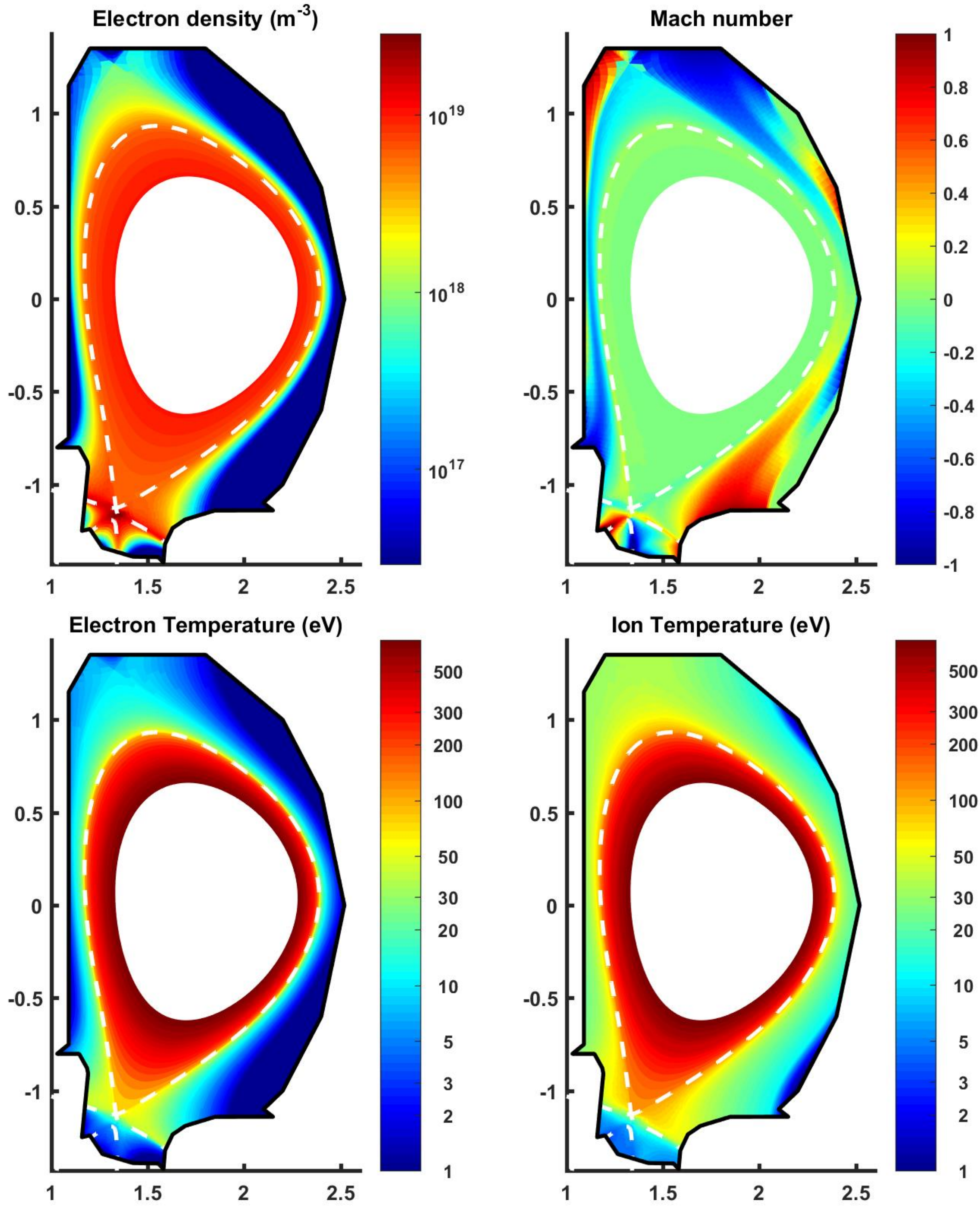

Figure 5.8.4 Example of SolEdge2D–EIRENE 2D outputs for the SF+ plasma: density, parallel Mach number, electron and ion temperature profile for a pure deuterium plasma with P_{in} = 1.5 MW $n_{sep} = 0.5 \times 10^{19}\ m^{-3}$.

In figure 5.8.5(a), the SF- configuration for HL-2M has been shown, the blue arrow 1#, 2# marked the strike points for separatrix, and the red arrow 3#, 4# marked the strike points for the flux surface correspond to second X-point. The black solid lines represent the chamber wall, and the green line on the wall represent the active pumping. In simulation, we set the electron density on core–edge interface from $1 \times 10^{19} m^{-3}$ ramp to $7 \times 10^{19} m^{-3}$, and consequently an increasing separatrix density (n_{sep}) up to detachment, from $0.4 \times 10^{19} m^{-3}$ to $2.4 \times 10^{19} m^{-3}$, see figure 5.8.5 (b). The power injected into the SOL region is fixed at 1.5 MW, and the radiative power increases throughout the density ramp, as shown in figure 5.8.5 (d).

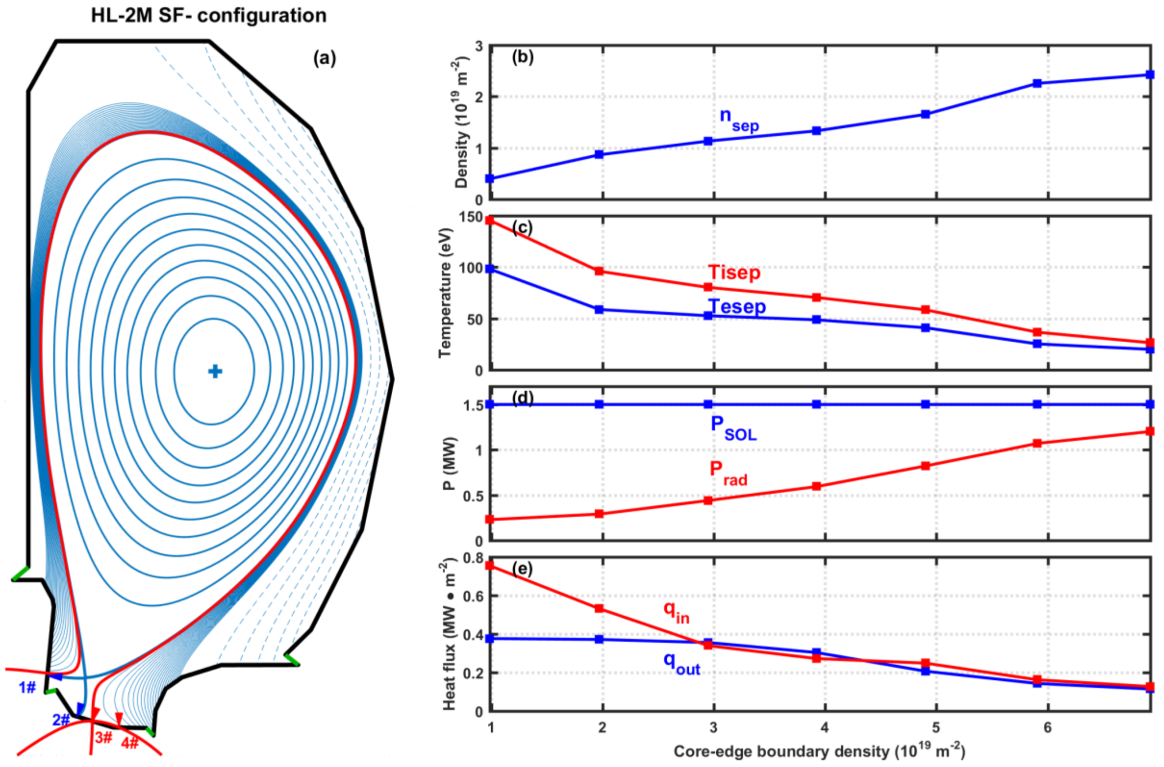

Figure 5.8.5 (a) SF- magnetic equilibrium. (b) separatrix electron density on midplane, also called upstream density. (c) upstream electron temperature (blue line) and ion temperature (red line). (d) Power injected into the SOL region (blue) and radiative power computed during the simulation (red). (e) peak value of heat flux outer target (blue line) and inner target (red line).

The meshes of SF- configuration for SolEdge2D-EIRENE code are plotted in figure 5.8.6. Figure 5.8.7 shows 2D profiles of plasma parameters for HL-2M SF- configuration.

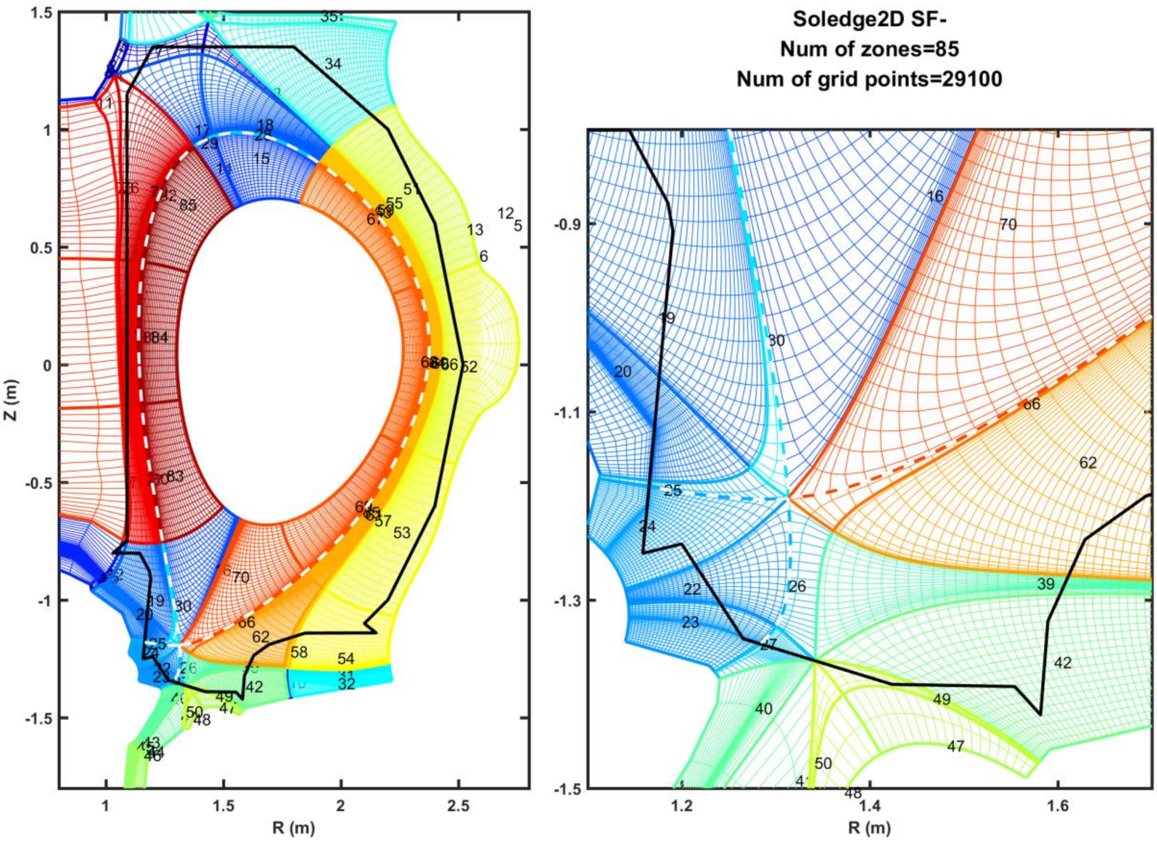

Figure 5.8.6 Grid of HL-2M SF- configurations used for SolEdge2D-EIRENE code.

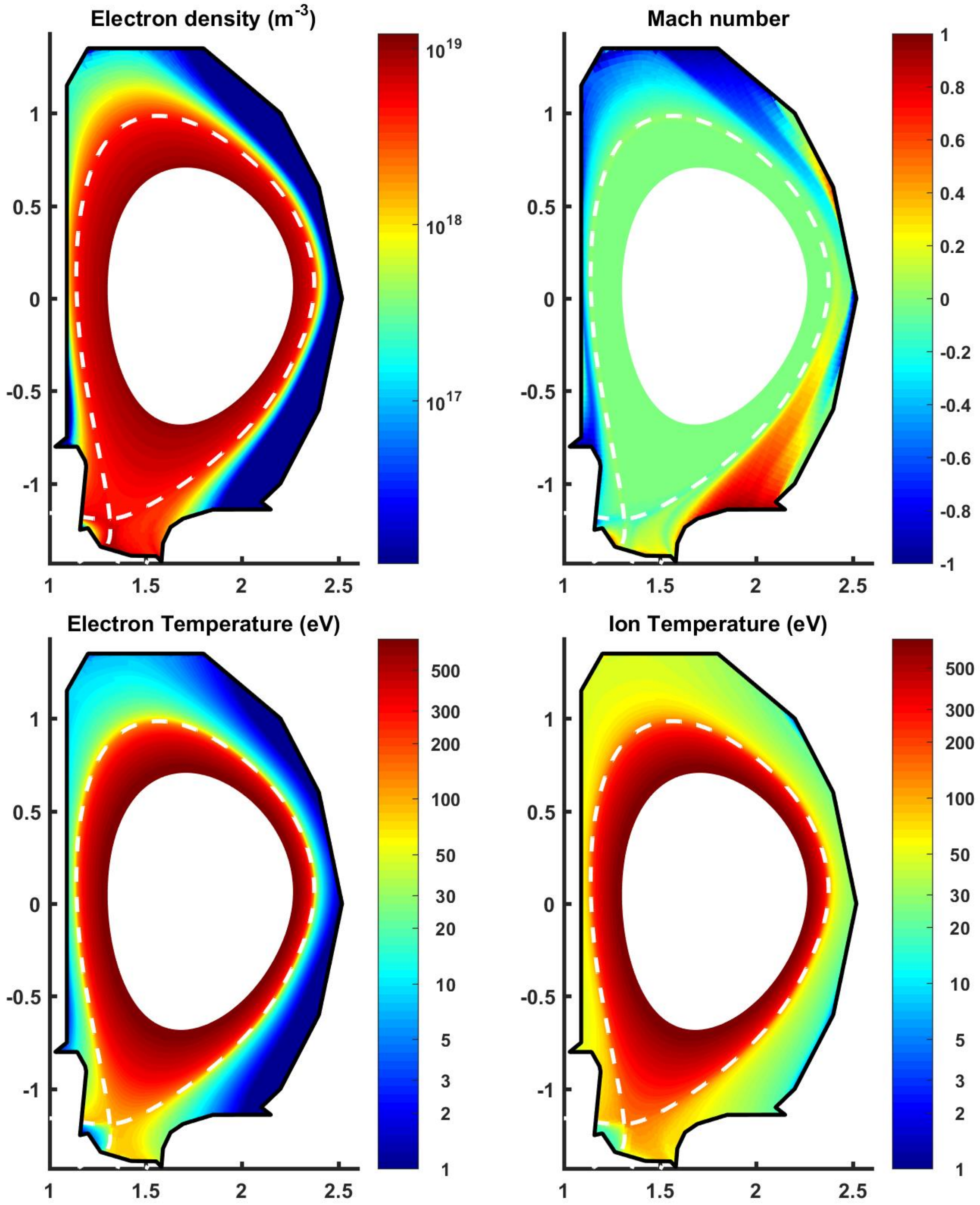

Figure 5.8.7 Example of SolEdge2D–EIRENE 2D outputs for the SF- plasma: density, parallel Mach number, electron and ion temperature profile for a pure deuterium plasma with P_{in} = 1.5 MW $n_{sep} = 0.39 \times 10^{19}\ m^{-3}$.

9. The impact of configurations

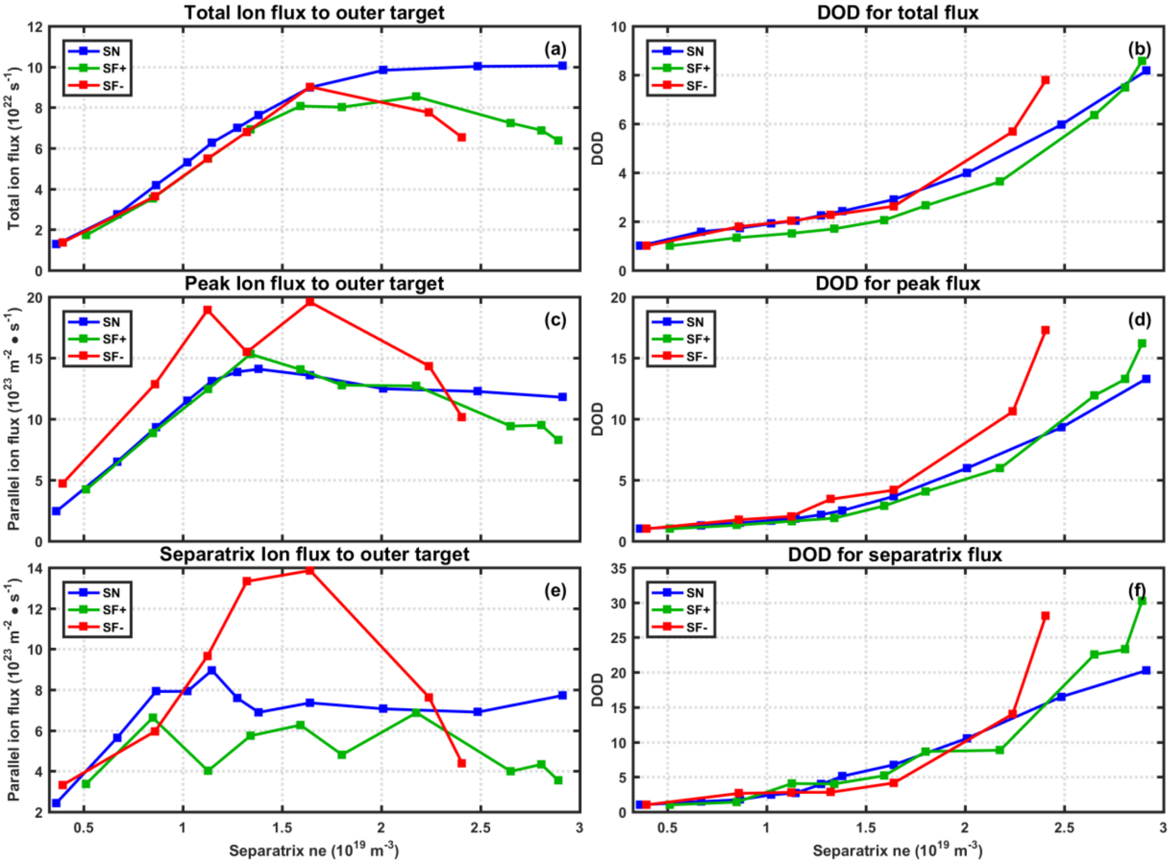

Figure 5.9.1. Ion particle flux to the outer target and the degree of detachment from the SolEdge2D-EIRENE density scan for pure deuterium plasmas with 1.5 MW input power. On the top panel (a), the dependence of the total ion particle flux ($\int nv_i \cdot sin\alpha_t \cdot ds$) is shown as a function of midplane separatrix density for the outer target in SN, SF+ and SF- configurations, here v_i represents parallel velocity for ion. (b), the DOD for total ion flux on the outer target. On the middle vertically (c, d), the same dependence is plotted for the peak ion flux and for the DOD defined for the peak value of ion flux. The bottom panels (e, f) show the dependence of the ion particle flux at the strike point and the corresponding DOD for separatrix ion flux.

In figure 5.9.1, we plot the total ion particle flux to the outer target, its peak value and the ion flux at the outer strike point as a function of the separatrix density for different configurations. In figure 10(a), at low density, during attached plasma ($\mathrm{n_{sep}} < 1.5 \times 10^{19}\ \mathrm{m^{-3}}$), the total fluxes for the three different configurations have similar trends. As the density is increased, a roll-over is observed. The SF- configuration~~s~~ has a lower threshold of detachment characterized by roll-over of the total ion flux, since the SF- plasma detachment onset is observed at an upstream density of $n_e \sim 1.6 \times 10^{19}\ m^{-3}$, while for SF+ the latter is $n_e \sim 2.2 \times 10^{19}\ m^{-3}$~~,~~and for SN $n_e \sim 2.5 \times 10^{19}\ m^{-3}$. The stronger drop in total flux indicates a deeper detachment is achieved for SF- at a given separatrix density. To be more quantitative, we evaluate the degree of detachment for the different configurations presented on figure 6. For detached conditions with a separatrix density of $n_e \sim 2.4 \times 10^{19}\ m^{-3}$, the integral DOD is 5.8 for the SN configuration, 5 for the SF+ configuration and 8 for the SF- configuration, figure 5.9.1 (b).

Considering the effect of divertor closure, it appears that the SN and SF+ configurations raise the outer strike point to bring the divertor plasma above the baffle structure as illustrated in figure 5.8.1 (a, b) and thus makes these divertor configurations more open compared to the SF- one, figure 5.8.1 (c). So, the most closed divertor (SF-) has produced the highest ne and lowest Te near the strike point, compared to more open divertor configurations at the same line-averaged density (see figure 5.9.5(b, c, d)). These observations are consistent with experiment results on C-Mod [1], ASDEX-Upgrade [2] and JT-60U [3], where L-mode discharges in more open divertors required ~15% higher core density than in more closed configuration to achieve detachment of the outboard divertor.

Then we consider the parallel ion particle flux on the strike point and the peak value of the ion flux, shown in figure 5.9.1(c, e), and define the local particle detachment onset in terms of parallel ion flux roll-over on the strike point and peak ion flux, while further out into the SOL the plasma remains attached. The SN and SF+ configurations achieve local particle detachment onset at a lower upstream density, compared to the SF- configuration. The local detachment occurs at $\mathrm{n_e} \sim 1.3 \times 10^{19}\ \mathrm{m^{-3}}$ for SF+ and SN, $\mathrm{n_e} \sim 1.6 \times 10^{19}\ \mathrm{m^{-3}}$ for SF-. The reason might be the positioning of the outer strike point on the vertical plate for SN & SF+, while the latter is on the horizontal plate for SF-. The degree of local detachment for SN and SF+ configurations are similar, while for SF- it is substantial higher.

The local detachment simulation results from the three configurations are consistent with the accepted idea of inclining the divertor target with respect to the magnetic flux line in order to reflect recycling neutrals towards the separatrix. The higher neutral pressure near the strike point leads to higher n_e, lower T_e and promotes detachment on strike point but inhibits detachment further out in the SOL with lower neutral pressure in that region. This concept can also be considered to be consistent with experiments in C-Mod and JET [1], ASDEX-Upgrade [2] and JT-60U [3].

To support this statement, in figure 5.9.2, the divertor neutral pressure and density profiles for the three different configurations are plotted. These pressure profiles are obtained for a separatrix density of $\mathrm{n_e} \sim 1.6 \times 10^{19}\ \mathrm{m^{-3}}$, that is, well after the onset of detachment. For SN and SF+ configurations, figure 5.9.2(a, b), the region of substantial neutral pressure is close to the strike point on the outer target. But for the SF- configuration, this region is far away from the strike point, even from the strike point corresponding to the second X-point. And the peak values of the neutral pressure and density for SF- are also lower than those observed in the SN and SF+ plasmas. To have a more quantitative analysis of the neutral pressure, its peak value and the neutral pressure at the outer target are plotted in figure 5.9.3 as a function of separatrix density for the three different configurations. It is evident that the neutral pressure in SN and SF+ plasma is substantially higher than in SF- plasma, for both peak (figure 5.9.3(a)) and separatrix value (figure 5.9.3(b)).

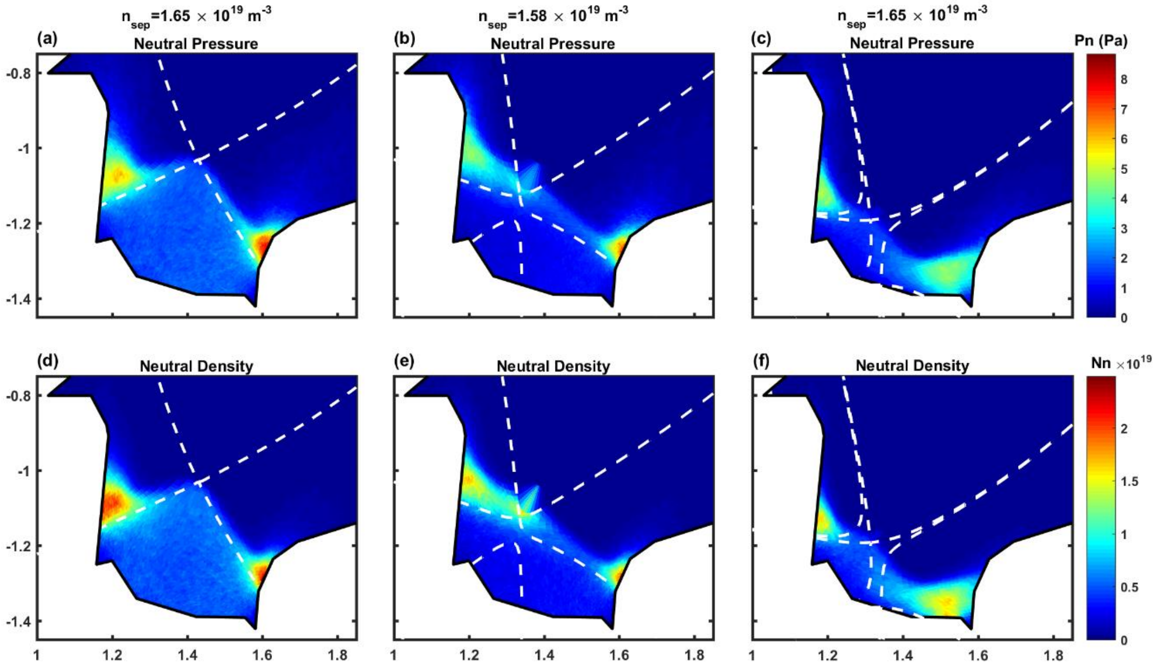

Figure 5.9.2. Neutral pressure profiles in the divertor for SN, SF+ and SF- configurations with the same input power and similar separatrix density. The white dashed lines represent the flux surface corresponding to the primary and the secondary X-points.

[1] Loarte A. et al 2001 Plasma Phys. Control. Fusion 43 R183
[2] Schneider R, Bosch H S, Coster D and Fuchs J C 1999 J. Nucl. Mater. 266–269 175
[3] Asakura N, Hosogane N, Itami K and Sakasai A 1999 J. Nucl. Mater. 266–269 182

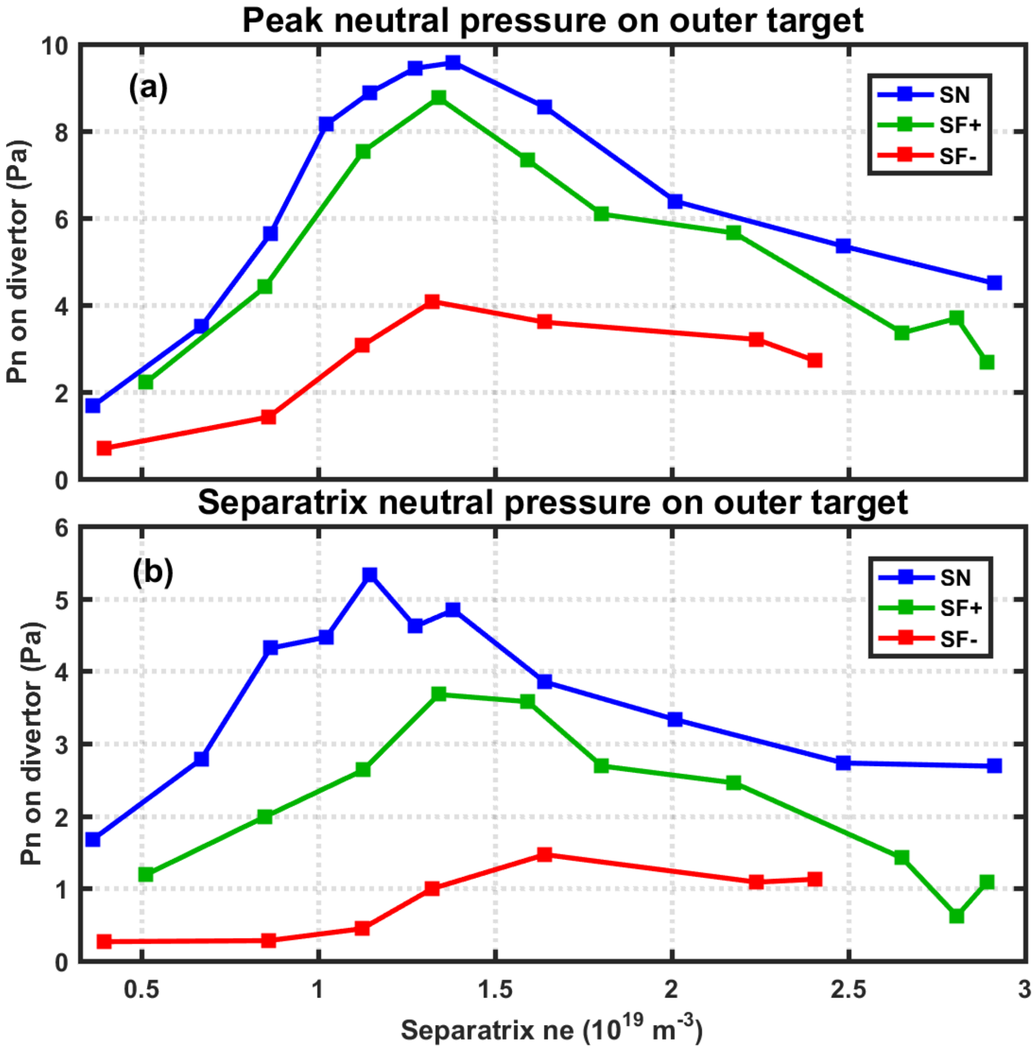

Figure 5.9.3 Neutral pressure on the outer target as a function of separatrix density for SN, SF+ and SF- configurations. The blue lines represent SN configuration, green lines represent SF+ and red lines represent SF- configuration. The peak value of neutral pressure on the outer target is shown on the top panel, and the neutral pressure on separatrix is plotted on the bottom panel.

From the 2-point model, equation (2.2.13), T$_{et}$ is expected to scale as $\propto L_{\parallel}^{-4/7}$, so that we would expect a reduction in upstream density for detachment with in increasing $L_{\parallel}$, through the terms of $L_{\parallel}^{-2/7}$. As there is a 5-fold increase in $L_{\parallel}$ between SN and SF+ configurations in figure 5.8.1 (e), a reduction of n_u by a factor of $(5)^{-2/7} \approx 0.63$ could compensate the $L_{\parallel}$ increase according to equation (2.2.13). However, comparing the simulation results from SN and SF+ configurations in figure 5.9.1, there is no significant impact of $L_{\parallel}$ on the detachment threshold.

Considering the effect of the total expansion f_R, the modified 2-point model has a analytic scaling for T_t and f_R: $T_t \propto f_R^{-2}[lnf_R/(f_R-1)]^{-4/7} \approx f_R^{-2}$. It is apparently that the plasma detachment onset at a lower n_u with an increasing f_R by a factor of f_R^{-1}. Comparison between SN and SF- configurations, $f_{R,SN} \approx 0.7$ $f_{R,SF-} \approx 0.65$, $L_{\parallel,SN} \approx 24$, $L_{\parallel,\,SF-} \approx 70$, the modified 2-point model predicts a reduction of n_u for SF- plasma detachment onset by a factor of $(70/24)^{-2/7}(0.65/0.7)^{-1} \approx 0.8$. As shown in figure 5.9.1 (a), the integral particle flux on outer target roll-over at $n_e \sim 1.6 \times 10^{19}\ m^{-3}$ for SF- and tend to be flat at $n_e \sim 2 \times 10^{19}\ m^{-3}$ for SN. However, the partial detachment onset at $n_e \sim 1.6 \times 10^{19}\ m^{-3}$ for SF- and $n_e \sim 1.3 \times 10^{19}\ m^{-3}$ for SN. Given this, the modified 2-point model predicts that the n_u for detachment onset impacted by geometry parameters as $\propto L_{\parallel}^{-2/7} f_R^{-1}$, which in good agreement with the simulation results for the integral detachment. But from the roll-over of local particle flux, the threshold of partial detachment doesn't show the effect from geometry parameter of configuration based on this modified 2-point model.

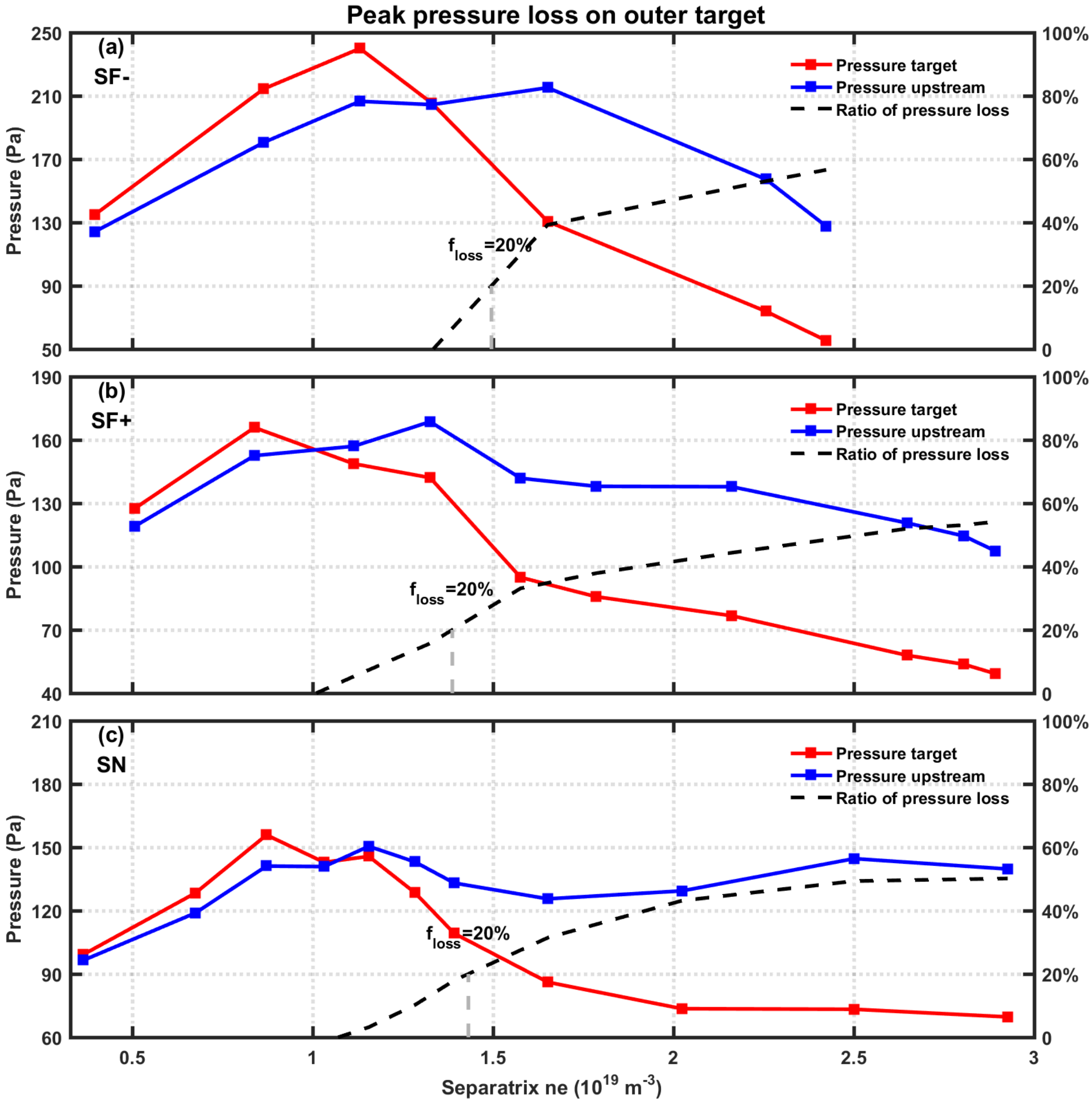

Figure 5.9.4. Comparison of the peak pressure on target (red line) and the upstream pressure (blue line) at the same magnetic tube in function of the upstream density, define the detachment as a more than 20% loss. The pressure corresponds to the left y-axis, $P = n_e(T_e + T_i)(1 + M^2)$. The black dash line represents the ratio of pressure loss between target and upstream, corresponding to the right y-axis.

As shown in figure 5.9.4, if we define the significant pressure loss as a more than 20% ratio of loss, the detachment thresholds of SF- is a little higher than SN and SF+, $n_e \sim 1.5 \times 10^{19}\ m^{-3}$ for SF-, $n_e \sim 1.4 \times 10^{19}\ m^{-3}$ for SN/SF+, $\Delta_{nu} < 10\%$. But SF- has a higher performance after detachment. For a detachment plasma $n_e \sim 2 \times 10^{19}\ m^{-3}$, the pressure loss $f_{loss} \sim 40\%$ for SN and SF+, $f_{loss} \sim 48\%$ for SF-. The pressure loss of SF- rises faster with the separatrix density, it reveals a higher degree of detachment for SF- plasma. There is no indication of a reduced detachment threshold with the second X-point near the target.

In order to gain some insight as to benefits of alternative configurations in these simulations, the distribution of the heat flux and other plasma parameters profiles on outer target for SN, SF+, SF- configurations are plotted on figure 5.9.5, with the similar separatrix density, and same input power. The SF- plasma has two strike points, the distance between the two strike points is $\Delta s_t \sim 170mm$, and the distance between the two flux suraface, correspond to the two strike points, on midplane is $\Delta s_t \sim 1mm$.

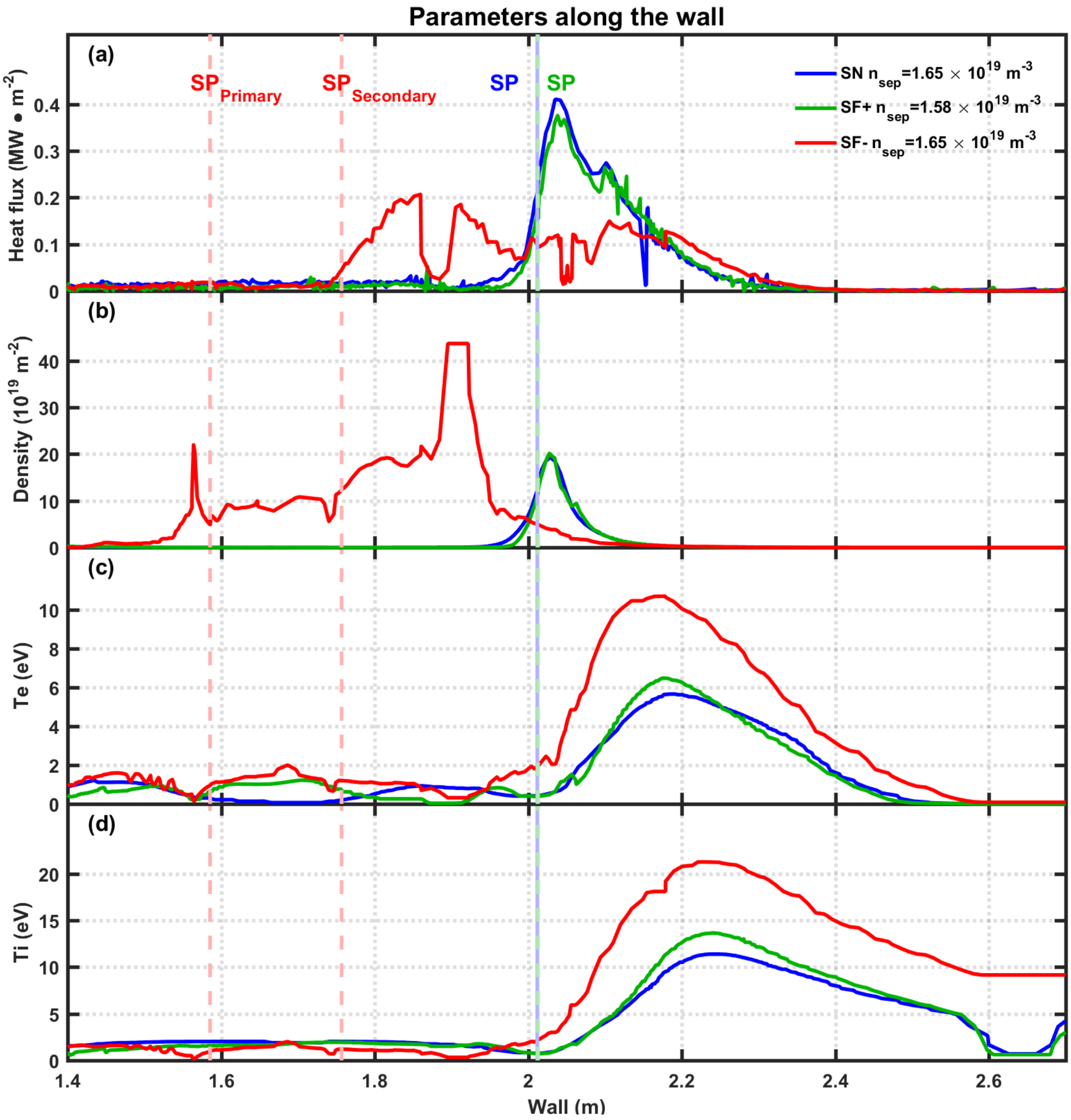

Figure 5.9.5. Heat flux, density, electron and ion temperature profile along the wall. The vertical, dash lines indicate the separatrix, corresponding to the parameter profiles with same color.

As shown in figure 5.9.5, with the small difference in separatrix density Δn_{sep}~4%, the SF+ configuration exhibited a similar parameter profiles at the outer target as the SN, even though there is a secondary X point in private region and the connection length between midplane and target $L_{\parallel}$ is much higher for SF+ as shown in figure 7.1 (e). As expected from 2-point model, equation (2.2.12, 2.2.13), the n_t scales $\propto L_{\parallel}^{6/7}$ and the T_t scales as $\propto L_{\parallel}^{-4/7}$. However, the expected reduction of T_t and increase in n_t for SF+ plasma is absent, figure 5.9.5(b,c,d).

For SF- configuration, the peak value of heat flux obviously less than others and the region of heat load is broader. This may benefit from the density far above other configurations and the position of temperature peak far away from the strike point.

The figure 5.9.6 shows the distribution of the heat flux along the wall and the total energy flux on each components for SN, SF+ and SF- configurations. For inner target, the integrated heat load is similar for three configurations, $\Delta p < 5\%$. For SF+ configuration, the heat flux doesn't cross the region between the separatrix respect to the primary and second X-point and the heat load on the wall is similar to SN configuration. With the second X-point in SOL, the SF- configuration is expected to have a diversion effect to heat flow. But this effect has not been found on the heat load for SF-, right side in figure 5.9.6. The heat flux flow along the separatrix respect to the second X-point.

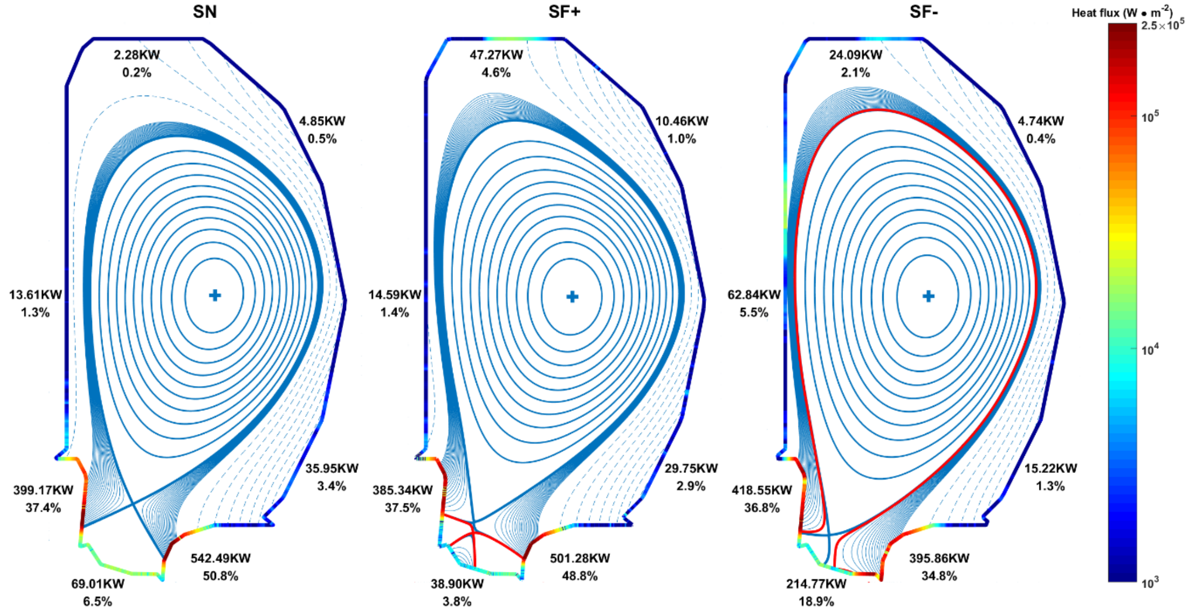

Figure 5.9.6 The heat flux profile on wall and the total energy flux on each component with P_{in} = 1.5 MW.

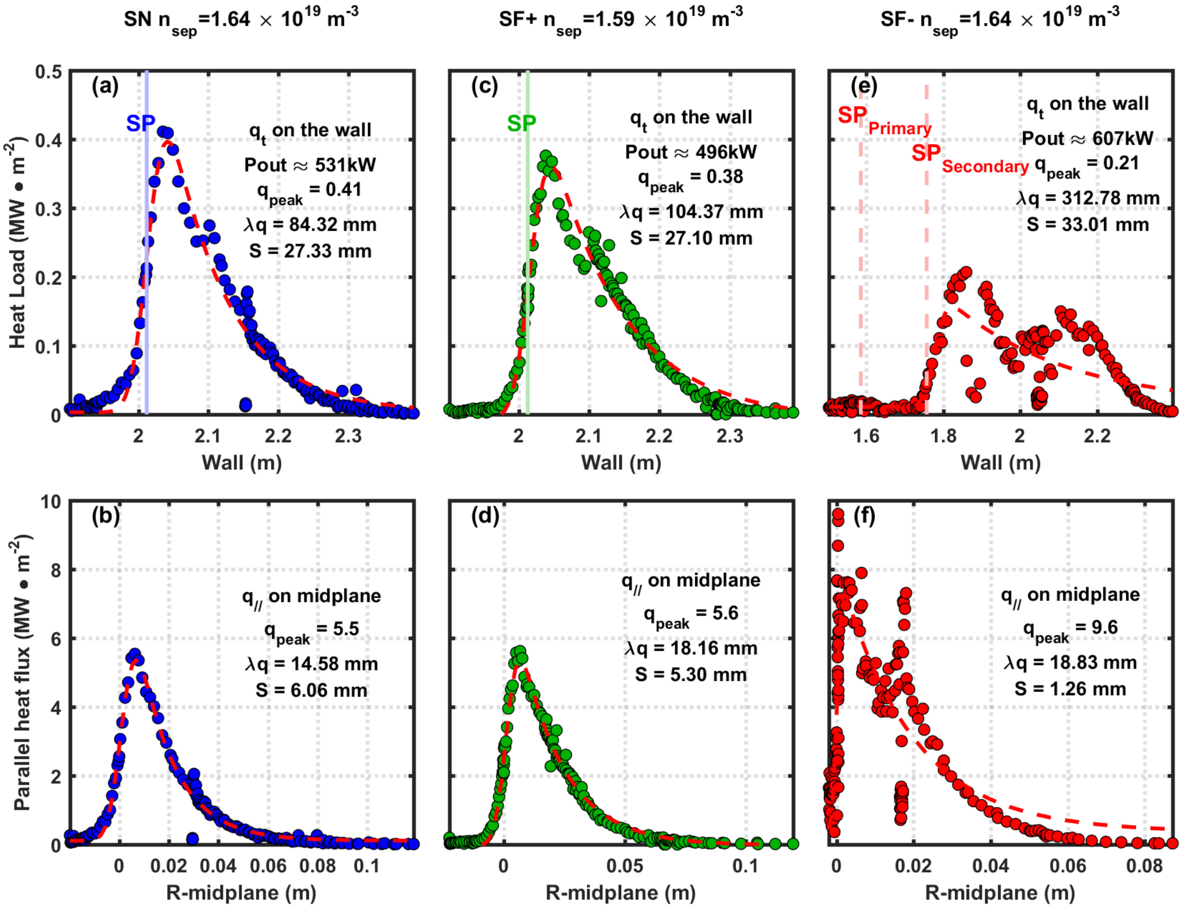

Figure 5.9.7. Top panel: Profiles of outer target perpendicular heat flux q_t for SN, SF+ and SF- configurations. Central panel: target parallel heat flux corrected by incidence angle $q_{\parallel} = q_t / sin\alpha_t$ and mapped to midplane for the three configurations. Bottom panel: target parallel heat flux corrected by incidence angle and total flux expansion $q_{\parallel} = q_t / sin\alpha_t \cdot f_R$. The different color dots represent the simulation results for different configurations obtained with input power Pin=1.5MW. q_{peak} is the peak value of the profile. The parameters λ_q and S represent the width and the spreading of profiles. The dash red line is a fit of exponential spread by Gaussian [1], $f = \frac{f_0}{2} e^{\left[(S/2\lambda_q)^2 - (x-x_0)/\lambda_q\right]} \times err + backgroud$. Here, f_0 is amplitude of the exponential, x_0 is center of the function, err is the complementary error function.
[1] T. Eich et al., Physical Review Letters 107 (2011), 215001

To have a more quantitative analysis of the effect of configurations to heat flux, the heat flux profiles on outer divertor plate q_t and the parallel heat flux profiles $q_{\parallel} = q_t / sin\alpha_t$ are shown in figure 5.9.7. Here, q_t is the total heat flux transported by plasma incidence the wall, includes the thermal of electron, ion, neutral and the recombination power of ion, without considering the radiation contribution. The $q_{\parallel}$ has been mapped to the midplane, and the radial coordinate for the below row of figure 5.9.7 is upstream radial distance to separatrix. Benefitting from the highest flux expansion f_x and lowest incidence angle, as shown in figure 9(d, f), the peak value of q_t reduces by a factor of 2, with the SF- configuration, compared to the SN and SF+ plasma. As expected in chapter2, the incidence angle and flux expansion has contributed to reducing the heat load peak.

It is apparent that the q_t and $q_{\|}$ profiles for SN and SF+ configurations are similar, $\Delta_{peak} \approx$ 7% $\Delta_{\lambda q} \approx$ 20% for q_t and $\Delta_{peak} \approx$ 2% $\Delta_{\lambda q} \approx$ 17% for $q_{\|}$. The small difference on parallel heat flux between SN and SF+ plasma, combined the similar plasma parameters on the wall as shown in figure 5.9.5, indicates that the geometry parameter $L_{\|}$ has no impact to the plasma parameters (T_e, n_e) on the wall, to heat flux and even the detachment threshold. The reason may be that comparison to width of $q_{\|}$ at midplane, ~20mm as shown in figure 5.9.7(b, d), the large difference for $L_{\|}$ only exist in a narrow region, $<$ 1mm as shown in figure 5.8.1(e).

The profiles of density and temperature on midplane for three configurations with the similar separatrix density has been analyzed in figure 5.9.8. For density profile, figure 5.9.8 (a, d, g), the radial width of density profile λ_{ne} almost same for SN and SF+ $\Delta\lambda_{ne}$~1.6%, and λ_{ne} for SF- is a lees than SN, $\Delta\lambda_{ne}$~10%. The width of temperature profiles, λ_{Te} is similar for three configurations, $\Delta\lambda_{Te} < 5\%$, figure 5.9.8 (b, e, h). The fitting for Ti profiles is not accuracy because of a obvously difference bewteen fitting funciton (red dash line) and Ti profiles (dots), figure 5.9.8 (c, f, i). The figure 5.9.8 shows that the big defference in divertor configurations doesn't affect the plasma parameter profiles in midplane.

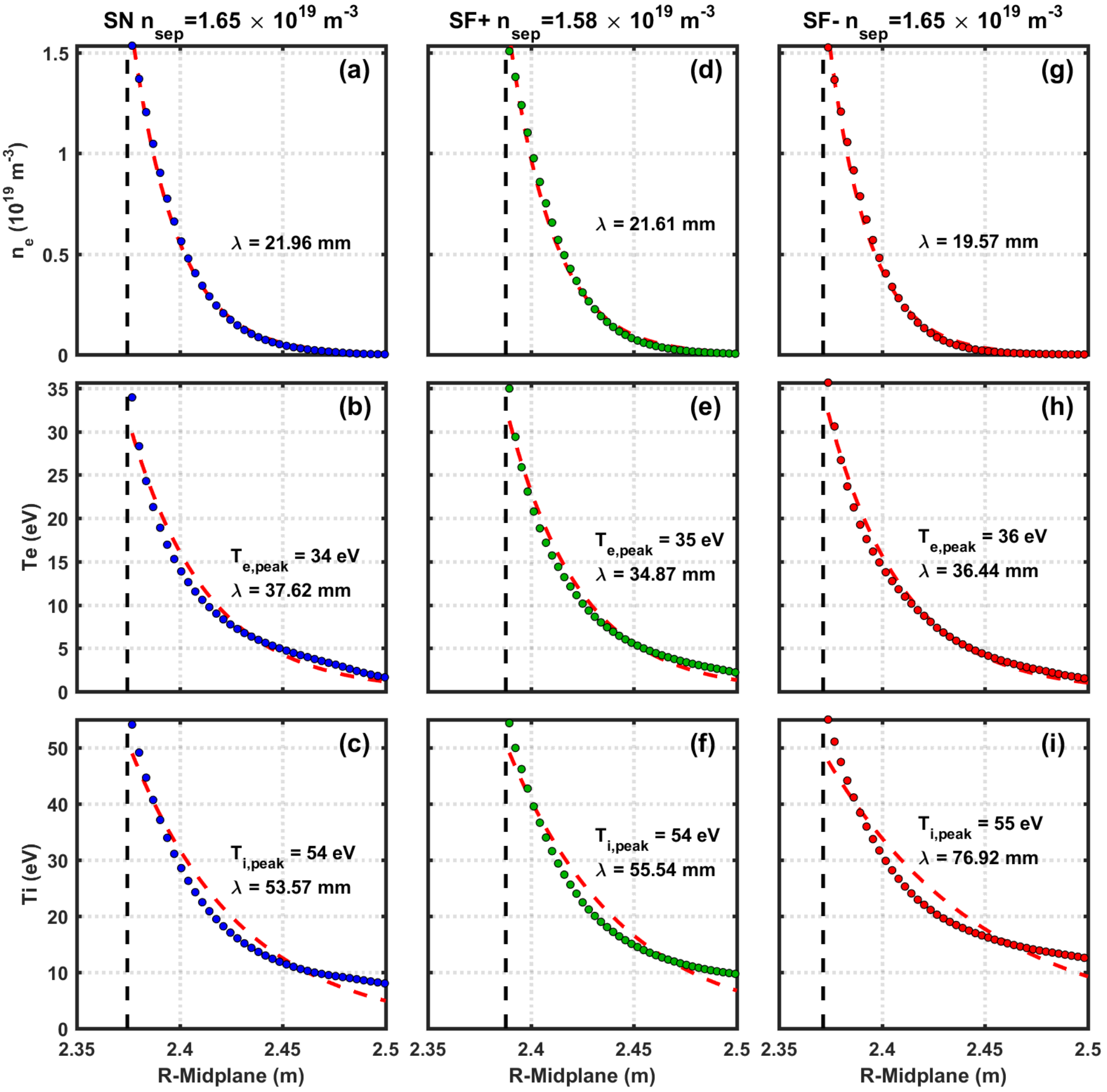

Figure 5.9.8. The density, electron temperature and pressure profiles on the midplane for three cases in figure 5.9.7. The vertical black dash line represents the plasma separatrix.

The detachment window is defined as the density interval over which the radiation front moves from target to X-point. The narrower this window, the more sensitive detachment state is with respect to density (and possibly other actuators) [1]. In the following, we investigate how this density window is affected by the divertor geometry. The evolution of radiation profiles during the detachment process for three configurations is shown in figure 5.9.9. Comparison between SN and SF+ cases, figure 5.9.9 (d), the detachment window increase from $\Delta_{nu} \approx 0.7 \times 10^{19} m^{-3}$ for SN, to $\Delta_{nu} \approx 1 \times 10^{19} m^{-3}$ for SF+, for a change of parallel connection length from $L_{\parallel,\mathrm{SN}} \approx 23\ m$ to $L_{\parallel,\mathrm{SF+}} \approx 120\ m$. It suggests an increase of the density window with parallel connection length. On the other hand, the SF- configuration has a narrowest detachment window

$\Delta_{nu} \approx 0.6 \times 10^{19} m^{-3}$ and a parallel connection length of $L_{\parallel,\mathrm{SF-}} \approx 70$, which seems to contradict the later suggestion. In reality the radiation front moves not only toward the X-point but also across flux surfaces (figure 5.9.9). A simple parametrization with a local connection length close to separatrix may not be a robust figure of merit.
[1] A Gallo et al 2018 Plasma Phys. Control. Fusion 60 014007

The start of the radiation front movement occurs at slightly lower densities than the roll-over in ion flux and the pressure loss. The SN and SF+ configurations achieve radiation detachment onset at a lower upstream density $\mathrm{n_e} \sim 0.97 \times 10^{19}\ \mathrm{m^{-3}}$ for SN, $\mathrm{n_e} \sim 0.9 \times 10^{19}\ \mathrm{m^{-3}}$ for SF+ and then SF- plasma start to detach at $\mathrm{n_e} \sim 1.15 \times 10^{19}\ \mathrm{m^{-3}}$ for SF-. This result can also be considered consistent with local particle detachment onset in terms of parallel ion flux roll-over on strike point and peak regime, as shown in figure 5.9.1.

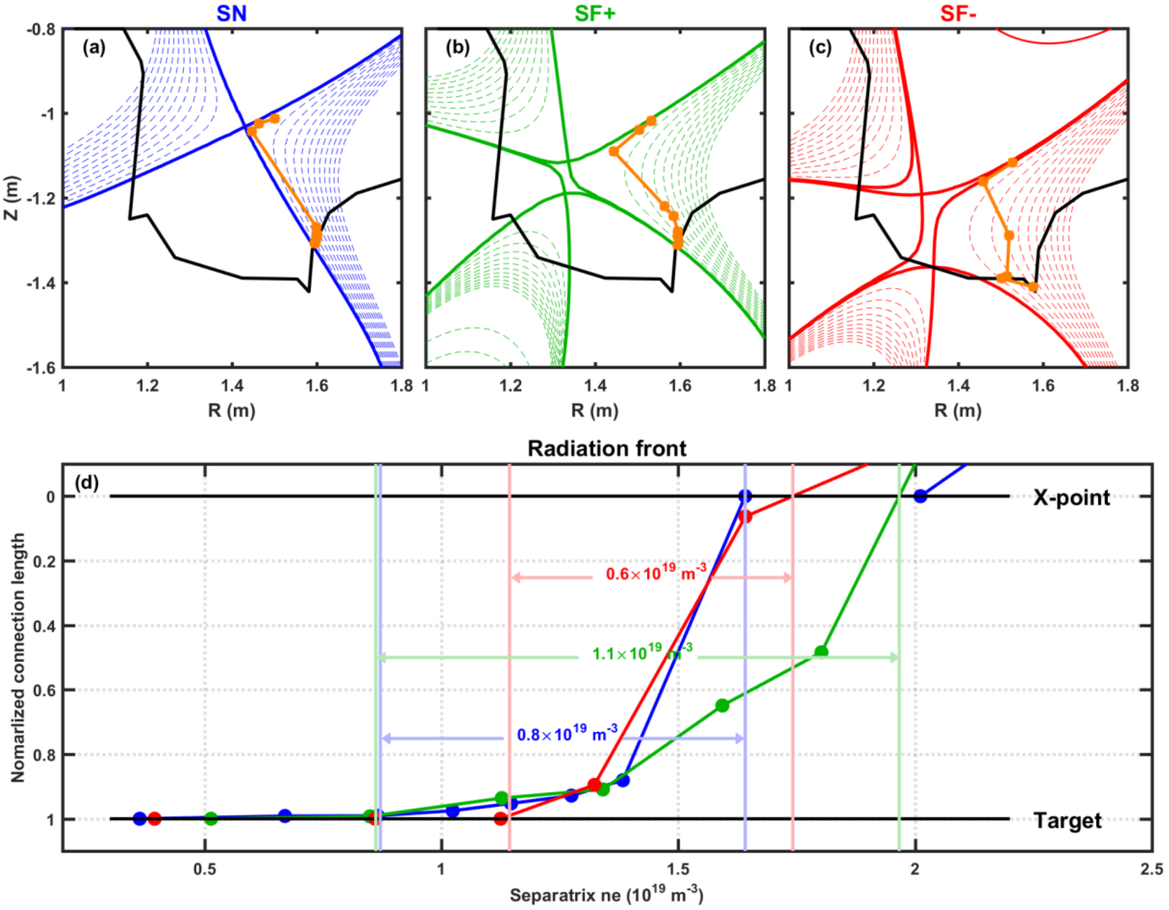

Figure 5.9.9. (a)–(c) Flux surface in the divertor volume for three configurations. The orange dot represents the position of radiation peak during the density ramp simulations. These three cases correspond to the evolution of radiation front shown below, with the same color. (d) Position of the front edge along the outer leg as a function of separatrix density.

Summary and conclusions

The impact of specific aspects of the magnetic and wall geometry on divertor detachment process is studied using SOLEDG2D-EIRENE simulations for HL-2M configurations in Ohmic density ramp with pure deuterium plasma. Three different divertor magnetic configurations are investigated, looking at the impact of connection length and flux expansion on detachment properties. Connection length increases by approximately a factor 6 from SN to SF+ configurations while flux expansion f_x at the outer target is varied by a factor 10 for SF- configuration with respect to SN one.

Some characteristics of the outer target detachment are assessed in these simulations. As a measure of the detachment threshold, we take here the upstream plasma density corresponding at the roll over in the ion particle flux on the outer target: the roll over of integrated ion flux indicates the threshold of integrated detachment and the roll over of peak ion flux indicates the threshold of partial detachment. The Degree Of Detachment is computed and used to estimate the level of detachment. The detachment window: density range estimated from the instant when the radiation front starts to detach from target and when it arrives at the X-point. Detachment control can benefit from a broader upstream density window.

Comparing the detachment process for SN, SF+ and SF- configurations, we find that SN and SF+ plasma always have similar threshold of detachment, $\Delta_{nu} < 10\%$, in terms of all detachment process: power dissipation, momentum and particle flux losses. The SF- achieve integral particle detachment at a lower upstream density,$n_e \sim 1.6 \times 10^{19}\ m^{-3}$, while $n_e \sim 2.2 \times 10^{19}\ m^{-3}$ for SF+ and $n_e \sim 2.5 \times 10^{19}\ m^{-3}$ for SN. However, SF- has a higher threshold for local detachment (separatrix $n_e \sim 1.6 \times 10^{19}\ m^{-3}$) compared to the SN & SF+ where plasma local detachment onset is observed at $n_e \sim 1.3 \times 10^{19}\ m^{-3}$.

The comparison of detachment threshold for these three configurations does not show a clear dependence on the connection length, as one could expect from 2-point model considerations. It seems that the penetration of neutrals and its dependence on geometrical aspects like vertical vs horizontal plate configuration as well as close vs open divertor could explain at least partially these behaviors. More specifically closure divertor for SF- and the vertical target plate for SN/SF+ reduce the threshold of integral and local detachment respectively, consistent with the C-Mod [33], ASDEX-Upgrade [34] and JT-60U [35] experiment results. On the other side it seems that connection length can explain why the SF+ configuration has a wider detachment window $\Delta_{nu} \approx 1 \times 10^{19} m^{-3}$, with respect to SN configuration where $\Delta_{nu} \approx 0.7 \times 10^{19} m^{-3}$ and SF- where $\Delta_{nu} \approx 0.6 \times 10^{19} m^{-3}$. This comparison reveals that the detachment window increases with connection length. On the other hand, the SF- plasma has a higher degree of detachment both in particle and momentum detachment.

The simulations and analysis presented here constitute a basis for more detailed studies of geometrical dependences of detachment on HL-2M configurations and even CFETR future reactor device. In the future, the H-mode plasma will be simulated, and the light impurities will be injected to study how the present picture changes under these conditions. To go further, the simulations of alternative configurations with different geometry parameters and second X-point positions are needed, to find a clearly, quantitative dependence of detachment behavior on geometrical parameters e.g. f_x, α, $L_{\parallel}$, R_t. Moreover, we will investigate the additional effect of the second X-point in the main SOL regime for the SF- configuration, for example, power repartition between active strike points.

It should be noticed that the electrostatic potential, grad B and ExB drifts can have a strong impact on particle and heat flux recirculation patterns in the divertor region, even if it is not completely clear if their role is always dominant or not. However, in this paper we have started from a detailed study without drifts allowing us to a better comprehension of the effect of magnetic and wall geometry disentangling these aspects from the drifts impact. We plan future studies with the activation of drifts to determine their impact in these configurations.

R. Mao et al, Nucl. Fusion 59 (2019) 106019 (16pp)